

Master Thesis



Czech
Technical
University
in Prague

F2

Faculty of Mechanical Engineering
Department of Process Engineering

Optimisation of spray dryer with nebulisation head

Bc. Matthew David Dimmock

Supervisor: doc. Ing. Jan Skočilas, Ph.D.

Field of study: Mechanical Engineering

Subfield: Process Engineering

August 2020

Acknowledgements

Firstly, I want to express my gratitude to the Merciful and Compassionate God, for His help throughout the course of my studies and also in the composition of this thesis.

Next, I want to thank my supervisor, Ing. Jan Skočilas, Ph.D. for his willingness to collaborate on this project. I've learned many things from him, not least that every stressful situations can be handled with a good dose of humour.

Finally I want to thank the many Czechs I've come to know over the last few years, friends who have supported and encouraged me. Infinitely practical and masters of improvisation, my respect and admiration for them grows each day.

Declaration

I confirm that this master's thesis was composed by myself and independently, under the guidance of my thesis supervisor. Wherever contributions of others are involved, every effort is made to indicate this clearly, with due reference to the literature, and acknowledgement of collaborative research.

In Prague, 03. August 2020

Abstract

The use of nanotechnology in the food industry has grown significantly in the last decade. As part of a wider project investigating the novel technology Carbon Dioxide Assisted Spray Nebulisation Drying (CASND), this thesis examines two particular dryer models used to produce nanoparticles and analyses their functionality from a mechanical engineering perspective. After providing a broad background in dehydration and nanoparticle technology, the dryer design is outlined, followed by the mass flow balance and numerical simulations of airflow. The results are discussed and recommendations for further developments are proposed.

Keywords: drying, dryer, spray drying, nebulization, nanoparticles, food processing

Supervisor: doc. Ing. Jan Skočilas,
Ph.D.
Department of Process Engineering,
Technická 1902/4,
160 00 Praha 6

Contents

Introduction	1	2.2.1 Physical Methods	15
		2.2.2 Physicochemical Methods . . .	18
		2.2.3 Chemical Synthesis	19
		2.3 Drying Nanoparticles	20
		2.4 Separating Nanoparticles	21
		3 Supercritical Assisted	
		Atomisation	23
		3.1 Principle	23
		3.2 The development of SAA and	
		CASND	25
		4 Conclusion	27
		Part II	
		Practical Part	
		5 Introduction to the CASND	
		project	31
		6 Problem analysis: preliminary	
		design of the dryer	33
		6.1 Initial data	33
		6.2 Preliminary design	34
		6.2.1 Preliminary flow balancing . .	34
1 Dehydration in the food industry	5		
1.1 Introduction	5		
1.2 The Drying Process	6		
1.2.1 Psychometry	6		
1.2.2 Transport phenomena	6		
1.2.3 Process Balancing	8		
1.3 Dehydration Systems	9		
1.3.1 Traditional Technology	9		
1.3.2 Recent Developments	10		
1.3.3 CFD in spray drying	10		
2 Nanoparticle Production	13		
2.1 Nanoparticles in the Food			
Industry	13		
2.2 State of the Art, how to produce			
nanoparticles	14		

6.2.2 Residence time of air in the laboratory dryer	36	9.1.1 First layer - Experiment data	60
7 Design proposal and realisation	41	9.1.2 Second layer - System geometry	61
7.1 Two variations	41	9.1.3 Third layer - Solver	63
7.2 Realisation	43	9.2 Results and discussion	63
7.2.1 Process overview	43	9.2.1 Modelling Measurement 11 . .	63
7.2.2 Processing units	43	9.2.2 Discussion of results	67
7.2.3 Working substances	44	10 CFD simulation	69
7.2.4 Process streams	46	10.1 Description of the task	69
7.2.5 Measurement equipment system control	47	10.1.1 The equipment	69
7.2.6 Pressure losses	48	10.1.2 Measurements	70
8 Measurement procedure	51	10.2 Numerical model	71
8.1 Introduction	51	10.2.1 Chosen approach	71
8.2 Measurements	51	10.2.2 Generating the shape	73
8.3 Protocol	54	10.2.3 Meshing	74
8.4 Results and evaluation	55	10.2.4 Fluent	77
9 Mass balance model	59	10.3 Results and discussion	83
9.1 Explanation of the model	59	10.3.1 Variant A	83

10.3.2 Variant B	84
10.3.3 Considerations	84
10.4 Figures and graphics	85
10.4.1 Representing flow in geometry A	85
10.4.2 Comparison of results for geometry A	88
10.4.3 Representing flow in geometry B	93
10.4.4 Comparison of results for geometry B	96
10.5 Further work	101
10.5.1 Explanation	101
11 Conclusion	105
11.1 General summary	105
11.2 Recommendations	106
11.2.1 General comments	106
11.2.2 Technical recommendations	107
Table of symbols	109
Bibliography	113

Appendices	
A Process Flow Diagrams	121
B Overview of measurements	125
C Mass balance MATLAB scripts	127
C.1 Flow rate integration from measured points	127
C.1.1 Inlet flow rate	127
C.1.2 Outlet volumetric flow rate	128
C.1.3 Outlet mass flow rate	129
C.2 Psychrometric recalculations . .	130
C.2.1 Moisture content to relative humidity function	130
C.2.2 Relative humidity to moisture content function	131
C.3 Balance model	132
C.3.1 Script: measurement11.m . .	132
C.3.2 Script: geometry.m	134
C.3.3 Script: solver.m	137

Figures

3.1 Nebulisation process using zero volume die and capillary restrictor [51]	24	8.1 Location of openings in the drying chamber [22]	52
3.2 Siever's original arrangement for continuous nebulisation [51]	25	8.2 Measurement location in the inlet pipe	53
5.1 Laboratory setup in arrangement A	32	8.3 Measurement location in the outlet pipe	53
6.1 Mollier diagram for preliminary air calculations [23]	35	8.4 Results from Measurement 11 [22]	56
7.1 Assembly drawings of the two dryer geometries (source: Vzduchotechnik, VÚPP, 2019) ...	42	8.5 Measured velocity profiles from Measurement 11	56
7.2 Process Flow Diagrams for both variants	44	8.6 Rotated valve from configuration A may have impeded the correct measurement of air flow	58
7.3 Proposal for sensor connections [24]	47	8.7 Location of the valve and anemometer probe	58
7.4 Location of measurement points in the drying chamber [adapted from Vzduchotechník, VÚPP, 2019]	48	9.1 Stream arrangement in Variant B (PFD)	62
7.5 Measurement locations in system	49	10.1 Location of measurement holes for both variants	70
7.6 Estimating pressure losses in Variant B	49	10.2 Processing tree in Workbench .	72
7.7 System characteristic for Variant B	50	10.3 Geometry A	74
		10.4 Inflation settings for Geometry A	75
		10.5 Cut of the mesh for geometry A	76
		10.6 Close-up of the inflation layer .	76

10.7 Mesh of geometry B.....	77	10.20 Geometry A - opening 1 – axial	88
10.8 Variant A - outer boundary conditions	78	10.21 Geometry A - opening 1 – tangential.....	88
10.9 Variant A - solution methods..	79	10.22 Geometry A - opening 2 – axial	89
10.10 Residuals during computation of Variant A - k-epsilon model	79	10.23 Geometry A - opening 2 – tangential.....	89
10.11 Velocity field - particle paths in variant A, k-omega simulation	80	10.24 Geometry A - opening 3 – axial	90
10.12 Variant B - solution methods .	81	10.25 Geometry A - opening 3 – tangential.....	90
10.13 Residuals during computation of Variant B - k-omega model.....	82	10.26 Geometry A - opening 4 – axial	91
10.14 Geometry A - Velocity field-contour at the level of the side inlets	85	10.27 Geometry A - opening 4 – tangential.....	91
10.15 Geometry A - Velocity field - cut at the level of the side inlet	85	10.28 Geometry A - opening 5 – axial	92
10.16 Geometry A - Velocity field - x-z plane.....	86	10.29 Geometry A - opening 5 – tangential.....	92
10.17 Geometry A - Velocity field - y-z plane.....	86	10.30 Geometry B - Velocity field-contour at the level of the side inlets	93
10.18 Geometry A - Velocity field - path of particles entering from the sides	87	10.31 Geometry B - Velocity field – cut at the level of the inlets	93
10.19 Geometry A - Velocity field - path of particles entering from the top	87	10.32 Geometry B - Velocity field – contour at the level of the blades .	94
		10.33 Geometry B - Velocity field - x-y plane.....	94

10.34 Geometry B - Velocity field - z-y plane	95	A.1 Process Flow Diagram for Variant A	122
10.35 Geometry B - Velocity field – particle path	95	A.2 Process Flow Diagram for Variant B	123
10.36 Geometry B - opening 1 – axial	96	B.1 Overview of measurements . . .	126
10.37 Geometry B - opening 1 – tangential	96		
10.38 Geometry B - opening 2 – axial	97		
10.39 Geometry B - opening 2 – tangential	97		
10.40 Geometry B - opening 3 – axial	98		
10.41 Geometry B - opening 3 – tangential	98		
10.42 Geometry B - opening 4 – axial	99		
10.43 Geometry B - opening 4 – tangential	99		
10.44 Geometry B - opening 5 – axial	100		
10.45 Geometry B - opening 5 – tangential	100		
10.46 Geometry A - comparison of simulations at opening 3 – axial .	102		
10.47 Geometry A - comparison of simulations at opening 3 – tangential	102		

Tables

2.1 Physical methods for generating nanoparticles	15	9.9 Auxiliary equations for Measurement 11	66
2.2 Separation methods	21	9.10 Results table for Measurement 11	67
7.1 List of processing units	45	9.11 Inlet and outlet flow for Measurement 11	67
7.2 List of substances	45	10.1 Summary of simulations for Variant A	101
7.3 List of streams - Geometry A . .	46	11.1 List of symbols used in Part I	110
7.4 List of streams - Geometry B . . .	46	11.2 List of symbols used in Part II	111
9.1 Mass balance input parameters .	61		
9.2 Reminder of the List of Streams - Geometry B	64		
9.3 Reminder of the List of substances	64		
9.4 Mass balance input parameters for measurement 11	65		
9.5 Reminder of the List of processing units	65		
9.6 Incidence matrix for configuration B	65		
9.7 Table of Data for configuration B	66		
9.8 Reference stream for measurement 11	66		



Introduction


The beginning of the third decade of the twenty-first century presents many challenges which will need to be confronted by engineers and scientists working across disciplines. Increased energy costs, a growing concern for consumer health and the environment combined with the emergence of novel technologies are bringing about changes to the food processing industry and the traditional way in which food is produced.

One area where this change can be seen is in the growing amount of research centred on the use of engineered nanoparticles in food items. Their potential benefits are numerous, and their use commercially is expected to rise over the next few years [48].

This entails the question of how to produce nanoparticles in an intensive and cost-effective way, whilst minimising energy consumption and the use of environmentally harmful substances.

This thesis will focus on a promising novel technological solution called Carbon-Dioxide Assisted Nebulisation Drying (CASND), and on the author's work to optimise a laboratory model of the equipment. CASND is a two-step process whereby a dissolved material mixed with water and near-critical CO₂ is atomised by pressure drop and then subsequently dried. The specific system to be studied was developed in partnership with the Food Research Institute Prague (FRIP).

The author's work is firstly to research the background and context to



CASND, summarising both the dehydration process of food products, as well as describing the various technologies used in the production of nanoparticles. The author will then describe the design process of the drying system, before analysing and using data taken during our measurements on the new dryer, conducting the mass balance of the drying process, and CFD analysis of the drying air in the equipment to check and investigate dryer function and suggest possible improvements.



Part I

Literature Research



Chapter 1

Dehydration in the food industry



1.1 Introduction

Whilst food dehydration is a practice dating back to antiquity, technological progress has led to the development of a wide range of processes, which now form one of the key pillars of the modern food processing industry. During dehydration, water is removed from food products to lengthen their lifespan and change their physical properties.

Dried food can be consumed directly, as in the case of apple slices, or introduced into the processing of other foodstuffs as an additive, with the purpose of enhancing the flavour or nutritious value, modifying the texture or colour and so on.

Firstly, the physical principles behind the dehydration process will be briefly examined, before moving on to look at current technologies employed as well as recent developments.

Next, the author investigates how nanoparticles are produced, dried, and separated, particularly in the food and pharmaceutical industries. He weighs up different technological approaches, comparing them between themselves.

Finally he focuses on the specific CASND technology, explaining how it works, and outlining its development.

1.2 The Drying Process

1.2.1 Psychrometry

Let's begin by explaining concepts that relate to the presence of water in a given substance and that we'll use subsequently to describe the drying process.

Whilst the term drying is typically considered to be more general, it will be used here -synonymously to dehydration- to indicate the removal of water from food products into surrounding air.

The first is absolute humidity, used as an indicator for humid air. Absolute humidity X [$\text{kg}_{\text{water}}/\text{kg}_{\text{dry air}}$] describes the ratio between the mass of water in air per unit mass of dry air [53].

$$X = \frac{m_w}{m_{da}} \quad (1.1)$$

Analogically, moisture content W [$\text{kg}_{\text{water}}/\text{kg}_{\text{dry product}}$] is the mass ratio of water in the product to dry product in a solid substance, such as dried food [53].

$$W = \frac{m_w}{m_{dp}} \quad (1.2)$$

Finally, relative humidity φ [-] represents the amount of water vapour in air as compared to the maximum amount of vapour that the air can absorb at a given temperature. It is defined in terms of partial pressures and saturation pressures at a given temperature [53].

$$\varphi = \frac{p_w}{p'_w} \quad (1.3)$$

1.2.2 Transport phenomena

In order to understand the process of dehydration, it is necessary to examine how various principles interrelate to effectuate the transfer of water between media.

Considering how hot air being blown around a wet object causes water on the object's surface to evaporate can help one to visualise the problem. Heat is transferred from the air into the object causing the water to evaporate, and the resultant steam is transferred back to the air by diffusion. The surrounding air is circulated by a process of convection [53].

The amount of water evaporating from a unit area of the product in one hour is call the drying rate, N [$\text{kg.m}^{-2}.\text{h}^{-1}$]. It is defined as follows [26]:

$$N = - \frac{m_{dp}}{A} \frac{dW}{dt} \quad (1.4)$$

During dehydration two distinct phases are observed, and recognised by different drying rates. During the first phase, the surface is wet and evaporation occurs at the wet-bulb temperature, thus the drying rate is constant and fairly rapid. Heat is transferred from the warm air to the surface of the product, and evaporated water steam is diffused into the air. Both of these phenomena are controlled by the flow of air across the interface.

Once sufficient amounts of water have been evaporated, the water surface retreats inside the product, and the product surface dries out, a drop in the drying rate is observed. The water locked inside the product's matrix must be evaporated and the resulting steam has to make its way to the surface before being removed. The temperature of the material surface rises above the wet-bulb value to approach the temperature of the surrounding air. Hence during the second drying phase the speed of the process is controlled by the diffusivity of water inside the drying matter as well as by heat transfer inwards. We talk here of a steam-gradient between the vapour pressure at the water surface, and the vapour pressure of the surrounding air. Nevertheless, liquid water also diffuses inside the structure, and so the property of effective diffusivity is introduced, which considers the combined transport of water in both liquid and vapour phases.

Thus there are four processes at work: the heat and mass transfer inside the product and the heat and mass transfer at the surface between the product and the air. The drying rate is regulated by the slowest of these, which generally tend to be the mass and heat transfer inside the product [26].

To describe the movement of water through the material, Fick's second law of diffusion is used [26].

$$\frac{\partial W}{\partial t} = \nabla \cdot (D_{eff} \nabla W) \quad (1.5)$$

Heat transfer through the product is described by Fourier's heat conduction model [53].

$$\frac{\partial T}{\partial t} = \nabla \cdot \left(\frac{\lambda}{\rho c_p} \nabla T \right) \quad (1.6)$$

1.2.3 Process Balancing

Crucial to the design of any dryer, mass and energy balancing helps to estimate the produce yield as well as the required amount of energy and drying air [53].

To balance the mass of water, the following equation is used, which describes how much water enters and leaves the system. The material flow rates are expressed in terms of dry matter and dry air [53].

$$\dot{m}_{da} X_{in} + \dot{m}_{dp} W_{in} = \dot{m}_{da} X_{out} + \dot{m}_{dp} W_{out} \quad (1.7)$$

And for the energy balance [53]:

$$\dot{m}_a H_{a\ in} + \dot{m}_p H_{p\ in} = \dot{m}_a H_{a\ out} + \dot{m}_p H_{p\ out} + q \quad (1.8)$$

To express the enthalpy of air [53]:

$$H_a = c_s(T_a - T_0) + X.L \quad (1.9)$$

The author notes that according to Singh and Heldman [53].

$$c_s = 1.005 + 1.88X \quad (1.10)$$

And the enthalpy of the product can be written as follows [53]:

$$H_p = c_{pp}(T_p - T_0) + W c_{pw}(T_p - T_0) \quad (1.11)$$

1.3 Dehydration Systems

1.3.1 Traditional Technology

In industry, various processes are employed depending on the substance being dried, and selecting the optimum one can lead to faster production rates, economies in energy requirements and improved quality of the dried product.

For solid products, the most widely used methods are **tray drying**, where the food is laid out on stacked trays in a drying chamber and hot air is blown past, and a semi-continuous variant called **tunnel drying**. In tunnel drying the racks are moved gradually through a drying "tunnel" either in co-current or counter current with the air stream. The speed at which they move can be adjusted to match the required drying time [53].

A more modern concept, **puff drying**, involves heating up the products under pressure to a high temperature before suddenly exposing them to atmospheric conditions. The drop in pressure and temperature results in flash evaporation of water, speeding up the process significantly. However, puff drying isn't suitable for all foods [53].

For liquid solutions two main technologies are used. The first is **drum drying** during which the liquid is spread on the edge of a rotating cylinder and heat is applied either directly, by blowing hot air through the middle of the tube, or indirectly, by heating the material of the cylinder. The results for some products are often of lower quality [26].

The second process is **spray drying**. The solution is forced through an atomiser to create a fine mist of small droplets inside the drying chamber. Heated air circulates in the chamber to evaporate the water, leaving small particles of dry matter which are separated from the air upon exit, often by cyclone [53, 58].

Fluid bed dryers are used in the case of liquids and solids with small particle sizes to produce more evenly dried results by floating the product directly on a bed of hot air [53].

Freeze drying is an energy intensive process that can be used for both liquids and non-liquid products. By lowering the pressure around a frozen

object, water can be removed through sublimation. This results in a higher quality output, which needs to be weighed against increased energy costs.

■ 1.3.2 Recent Developments

With rising environmental concerns and tighter health legislation over the last couple of decades, pressure has grown to find ways of drying that are both more energetically efficient and hygienic. This has led to the development of unconventional methods for drying, often combining various traditional technologies in one process. These so-called hybrid techniques have been expanding the realm of what is possible, allowing for greater control of parameters such as drying temperatures, and the properties of the dried product [26].

Also, developments in numerical analysis and computer simulation have led to a better understanding of the drying process and to improved dryer design [26].

■ 1.3.3 CFD in spray drying

Computational fluid dynamics (CFD) offers tools to help optimise the design of certain types of dryers, most importantly spray dryers. Combining applied mathematics with computer technology allows the various processes inside a dryer to be modelled effectively. These include fluid flow, heat transport, and eventually phase changes of substances. CFD numerically solves the Navier-Stokes equations and other thermodynamic relations, giving scientists and engineers an understanding of what is happening inside the dryer in situations where taking measurements is impractical [31].

In the case of spray-drying, CFD can help to examine the flow of air inside the geometry of the drying chamber to ascertain residence times, dead-spots, optimum flow-rates, temperatures, and much more. This tool can help improve the efficiency of a particular dryer model, and be used to simulate the performance of a scaled-up version of laboratory equipment [31].

In order to simulate turbulent flow, an appropriate simplification must be chosen. The five most common models used in spray dryers are as follows:

Standard $k - \epsilon$. Here, k represents turbulence kinetic energy and ϵ turbulence dissipation rate. This model, which is concerned primarily with the mechanisms affecting turbulent kinetic energy, is robust and fairly accurate.

Realisable $k - \epsilon$. Similar to the previous model, however certain constraints are applied relating to normal stresses which make the model more realistic, particularly in the case of rotation.

RNG $k - \epsilon$. The Renormalisation Group Method takes a different approach to the previous methods, using alternative functions and values in describing k and ϵ . It is based on the instantaneous Navier-Stokes equations, and is more accurate for flows with swirl.

RANS. Reynolds-Averaged Navier-Stokes models use a simplified version of the Navier-Stokes equations, whereby fluctuating values are replaced by a constant "average value". This allows a steady result to be calculated, even when the flow regime would naturally vary with time, and reduces required computing power.

Reynolds stress model (RSM). This model uses time-averaged velocities, and is suitable for situations where swirl is prevalent. Nevertheless it converges slower than the other models [31].



Chapter 2

Nanoparticle Production



2.1 Nanoparticles in the Food Industry

Nanotechnology is a field of engineering that deals with manipulating particles in the size range of nanometres. Interest in nanoparticles -particles with dimensions in the nano-scale range- has grown in recent decades as their properties and benefits are gradually being explored and as technological improvements enable the creation of new types of particles [48].

In the domain of food technology, nanoparticles are produced naturally during certain processing operations, and so are widely consumed by the general public. Nevertheless the risks associated with using engineered nanotechnology in food production remains as yet poorly understood, and concerns are being raised over nanoparticles compromising the natural digestive process [48, 57].

Owing to their small size, the behaviour of particles of nano-scale proportions is affected primarily by surface properties rather than the behaviour of the bulk material. Hence, they can be used to affect the properties of food in novel ways that can't be achieved through using traditional ingredients. Applying nanotechnology can yield benefits in improving the flavour, texture, colour and shelf-life of food, as well as increasing the absorption of nutrients into the human body [47, 48].

between "top-down" methods that consist of breaking down larger particles until they obtain the required dimensions and "bottom-up" methods that involve constructing nanoparticles directly from smaller molecules (for example creating polymers out of monomers) is distinguished. Physicochemical methods are also documented as a way of forming nanoparticles from pre-formed polymers dissolved in a solvent and dispersed within a nanoemulsion. Thus the physicochemical methods can be viewed as the second phase of a two-step production process, the first being a choice of method for producing the emulsion. The number of possible combinations of emulsifying techniques and polymer solidification methods provides a large array of options [32].

2.2.1 Physical Methods

Processes which use mechanical or electrical energy to break down larger particles or droplets are called physical methods. Force is exerted on the particles or droplets either in the form of mechanical impact or compression, as shear within a liquid, or through electric fields. These are also known as "top-down" methods [46]. The methods are summarised in **Table 2.1**, followed by a more detailed description. The energy required is the author's own unverified estimate, given the absence of data available in the literature.

Since the author's research is primarily focused on solid nanoparticles, it's important to distinguish between one and two-step production methods. In single-step methods the particles are produced without an intermediate emulsification or similar dispersion stage.

Method	Nature	Lower-limit size	Energy required
Milling	NP	50 nm	High
Spinning disk	NS	200 nm	Medium
Supercritical fluids	NS, NC, NL	50 nm	Low
Electrified coaxial jets	NS, NC	150 nm	Low
Microfluidisation	NE	120 nm	High
Ultrasound emulsification	NE	75 nm	Medium
Membrane processes	NE, NS, NC	260 nm	Low

Table 2.1: Physical methods for generating nanoparticles

■ Single-step methods

Milling. The most widely used top-down method for food products, milling can be broken down into two separate processes, ball milling and jet milling, and can be conducted in a liquid or gas medium. Since milling is versatile, a wide range of materials can be processed.

Ball milling (or bead milling) is an adaptation of widely macro-scale ball milling where the particles to be crushed are placed in a rotating chamber with hard spheres and gradually rotated. The impact of the balls on the product material breaks it down into ever smaller pieces. In nanotechnology, the balls are much smaller and are usually made from steel, flint or ceramics [2, 21, 46].

Jet milling similarly uses impact and shear to reduce particle sizes. In this case however the particles are blasted into each other directly without the presence of beads [2, 46].

Experiments have been conducted showing that high-energy ball milling can reduce cellulose to 24 nm in size [33] and a scalable method produced start with dimensions of 245 nm [37].

Spinning disk processing. This process consists of spraying a mixture of the product dissolved in a solvent onto a heated rotating disk. Large centrifugal forces break the liquid down into small droplets, whilst heat transferred from the disc evaporates the solvent, leaving behind solid nanoparticles. Often surfactants must be added in order to hinder the particles from agglomerating after formation [2]. The process can also be used for chemical reactions, such as the formation of silver from reactants [56].

A spinning disc reactor with rotational speed of 1500 rpm was used by Khan and Rathod to create curcumin nanoparticles with sizes from 180 nm to 220 nm, which had higher dissolution rates over macro-sized particles [29].

Supercritical fluids. Developments on the principle of microfluidisation involve exploiting the benefits of supercritical fluids. Carbon dioxide under high pressure can be used directly as a solvent into which is dissolved the active ingredient. The fluid is then expanded through a nozzle into a chamber at atmospheric pressure and forms a fine mist due to the large shear forces.

Then the CO₂ quickly evaporates, causing the solute to precipitate in the form of nanoparticles. This process is known as the rapid expansion of supercritical solutions (RESS) and whilst it can produce very small nanoparticles, in the absence of a stabiliser they tend to agglomerate into larger structures. Variants include the rapid expansion of supercritical solutions into aqueous solution (RESSAS), supercritical antisolvent precipitation (SAS) and a method involving dissolving the active ingredient in water which is then mixed with a supercritical fluid as well as others [2, 50].

Using RESS, some researchers encapsulated vitamin B in solid-lipid nanoparticles of dimensions around 100 nm [12], whilst others produced nanoparticles from turmeric extract in 2019 with sizes around 50 nm [35].

Electrified coaxial liquid jets. Using an interdisciplinary approach, the electrified coaxial liquid jet method (electrospraying) atomises an envelope of two charged liquid jets using electrical fields. This results in nanoparticles of one substance encapsulated within another. Because they are electrically charged, the droplets naturally disperse in space, preventing coagulation. No mechanical forces are used besides the pressure needed to form the initial jet [27, 61, 46].

Nanocapsules for drug delivery were created with sizes around 110 nm [8].

■ Emulsification methods

Emulsions are produced either as the first phase of a two step method or used directly for certain applications.

Microfluidisation. Shear forces acting in a liquid can be used to break up droplets in an emulsion. These can be created by forcing the fluid through a nozzle with a high pressure drop. Cavitation and impact forces also work to reduce the particle size. The technology is already widely adopted in the food industry and is used, for example, to encapsulate pro-biotic cultures [2, 46].

Researchers were able to create 120 to 1000 nm zein nanoparticles by microfluidising an emulsion containing dissolved zein, which was then precipitated [15].

Ultrasound emulsification. A potentially more cost effective way of producing nanoemulsions, ultrasounds emulsification subjects the liquids in an emulsion to extreme pressure fluctuations that cause cavitation, shock waves and liquid jets, using high frequency sounds waves. Surfactants are used to stop the droplets from recombining, and heat generated during the process can damage some sensitive materials [34, 46].

Chang et al. used ultrasound emulsification followed by nanoprecipitation to efficiently produce nanoparticles from starch in the size-range of 75 nm [9].

Membrane emulsification. An alternative to using shear forces, nanoemulsions can also be produced by forcing the dispersed phase through a membrane with very fine pores into another liquid (oil or water) flowing tangentially to the membrane. Whilst the method offers the advantage of lower energy requirements and a reduced need for surfactants, the low flux rate and the risk of fouling engender potential difficulties for scaling up the process [46].

Variations on membrane emulsification also exist, such as membrane mixing, whereby a reactant is forced through a membrane into another solution. The resulting chemical reaction produces solid-phase nanoparticles, nanocapsules, etc. which can have dimensions as small as 260 nm. The author notes that membrane mixing is a single-step method [10].

■ 2.2.2 Physicochemical Methods

As the name implies, physicochemical methods use a combination of physical and chemical techniques to create nanoparticles. Unlike during chemical processes, nanoparticles are formed from already synthesised polymers using principles such as evaporation, over-saturation and diffusion. Most of the author's sources for this section were taken from research on nanoparticles for controlled drug release for pharmaceuticals [19, 25, 48, 55].

Emulsion-solvent evaporation. Polymer nanospheres can be prepared from nanoemulsions composed of an aqueous phase and the polymer dissolved in a volatile solvent such as dichloromethane. The solvent phase is evaporated by mixing or lowering the ambient pressure and the remaining polymer nanoparticles can be removed by ultracentrifugation [25, 55, 59].

Nanoprecipitation. Nanoprecipitation involves dissolving polymers in a water-miscible solvent, which is then mixed into an aqueous solution. As the solvent rapidly diffuses into the water, the polymers precipitate in the form of nanocapsules, which can be kept from reassembling by the inclusion of a surfactant. [59, 43, 45].

In a modern variant of the process called flash nanoprecipitation (FNP), rapid mixing of the solvent and polymeric solution causes local oversaturation and precipitation [44].

Reverse salting-out. Reverse salting-out (or simply "salting-out") is a process whereby two phases of an emulsion are prepared separately. The polymer is dissolved in a water-miscible organic solvent (usually acetone). Simultaneously, the aqueous phase is created by adding salt and a colloidal stabiliser to water forming a gel. Once the two phases are mixed, they form an emulsion due to the high concentration of salt, which inhibits the solvent and aqueous phase from combining. Next, a large quantity of water is added and the solvent diffuses suddenly, leaving behind the polymer material to form nanospheres. The solvent is then removed by low-pressure evaporation and the salting agent by repeated washing or cross-flow filtration. The method is suitable for compounds that can't tolerate higher temperatures [59, 25, 55].

Emulsification diffusion. In the first instance, a partially water-miscible solvent (for example ethyl acetate) in which the polymer is dissolved is fully saturated with water. Secondly, the solution is emulsified. And finally more water is added, whereby the solvent diffuses into the water, leaving behind the solidified nanoparticles. This process can be used to form nanospheres and liposomes.

This technique is scalable and has low energy requirements. However, the process takes longer to complete [25, 55].

2.2.3 Chemical Synthesis

The bottom-up approach of constructing nanoparticles through in-situ chemical reaction or by self-assembly of polymers and a surfactant offers methods with a lower requirement of mechanical energy. These methods and their relevant principles fall into the realm of chemical engineering, and rely primarily on mixing appropriate solutes, solvents and surfactants [2]. As such they are

of less interest to the author and are not included within the scope of this thesis.

■ 2.3 Drying Nanoparticles

Following the creation of nanoparticles, it is often necessary to remove them from the medium in which they were formed by drying. Dried nanoparticles are more stable both physically and chemically, and so can be better stored [1].

Freeze drying. This method varies little from freeze-drying used for larger particles. As water is removed by sublimation resulting from depressurisation, nanoparticles are subject to large stresses. Thus, it can be necessary to use protectants. The process must be carefully tuned in order to ensure that the dried nanoparticles have the required humidity and stability. Freeze-drying has the disadvantage of being both energetically demanding and slow, and so is only appropriate for substances with a high added value. Particles clump together to form the drying cake, which then needs mechanically breaking up. Nevertheless, substance recuperation is straight-forward. If the process is conducted correctly, nanoparticles can have a shelf-life of several years [1, 7].

Spray Drying. The nanoparticle-containing liquid can be forced through an atomising nozzle and the resulting droplets dried by a co-current stream of warm air. The process is quick, continuous and easily scalable, and hence is widely employed. Nevertheless, there are high energy requirements for heating the large amounts of air flowing through the dryer. The co-current flow can help keep the temperature of the particles lower than that of the incoming air. Collection efficiency is lower for spray drying, as some particles are lost during separation from air [7].

Fluid bed drying. The concept of using a fluid bed dryer for drying nanoparticles was trialed by Bourezg et al. in a batch laboratory-scale dryer. The method differs from spray drying in that the air flows counter-current to the falling droplets, suspending them inside the dryer in a floating layer. Bourezg noted that the particles look much longer to dry, and that the resulting properties of the dry powder were at best comparable to those of the spray dried powder [7].

2.4 Separating Nanoparticles

Method	Medium	Lower-limit size [nm]	Power requirements kW per m ³ /s
Cyclonic separation	gas	200 nm	0.2 - 2.0
Electrostatic Precipitation	gas	1 nm	0.4 - 1.2
Electrostatic Cyclones	gas	10 nm	unknown
Filtering	gas, liquid	10 nm	0.8 - 2.0

Table 2.2: Separation methods

Following their creation, solid nanoparticles must be separated from the fluid medium in which they were produced or dried, usually air. Owing to their size, particles at the nano-scale are more difficult to separate than normal particles, and thus most classical separation techniques are ineffective. The reasons for this usually relate either directly to the size, such as the case of filters with pores that have micrometric diameters, or to the lack of mass/inertia, which limits the use of cyclones and settlers.

Here the author documents technological processes which are currently employed for this purpose. His results are summarised in **Table 2.2**. The estimates for power consumption were provided by Goodfellow and Tähti [20].

Cyclonic separation. Whilst traditional industrial cyclones are able to separate particles down to the micrometre range, they have proved ineffective at removing particles smaller than 1 μm . Since the size difference between nanoparticles and molecules of the surrounding medium is small, centrifugal forces are limited in their ability to displace particles in a cyclone due to large buoyancy. Cyclones designed for separating nanoparticles from air or flue gases have a very small diameter and work by reducing the pressure in the chamber to around 10 torr. This decrease in gas density leads to an increase in slipping, or particle movement towards the outer wall of the chamber, where they can be removed from the gas flow. This method is effective for removing particles over 200 nm in diameter [11].

Electrostatic precipitation. This processes uses electric fields to separate nanoparticles from air. Precipitators are small enough to be fitted as part of

a ventilation system. They consist of a charging section composed of a row of metal wires suspended between vertical metal plates which are alternatively charged or grounded. The large negative voltage which is applied between the plates and wires ionises the gas and causes the newly-charged particles to be attracted to the grounded plates. The collected nanoparticles can be removed once the voltage is switched off. The energy consumption of precipitators, which although being highly efficient, is directly proportional to the number of particles separated, and therefore is not insubstantial. Their collection efficiency is higher for nanoparticles than for microparticles [5, 28, 36]

Electrostatic cyclones. The principles of centrifugal separation and electrostatic precipitation can be combined to produce an effective separator with far greater through-flow than vacuum cyclones. Particles in the air are charged prior to entering or within the separation chamber, where large electric fields force the particles to aggregate at the outer surface. Airflow in the boundary layer helps to remove these aggregates and transport them to a small outlet through which flows only a fraction of the total air. Thus the process is fully continuous. This method can be used for particles as small as 10 nm which are unaffected by the centrifugal force [60].

Filtering. Filters, made from glass, polymer or cellulose fibres or alternatively from membranes with nanopores can be used to remove nanoparticles from gases or liquids in much the same way as ordinary particles. The fibres must be of particularly small dimensions, usually within the nano-scale. Filters have been tested to be more effective at removing particles in the size range of 10-50 nm than those ranging from 100 to 300 nm. A higher efficiency is observed in the case that the fibres are electrically charged [4, 30, 40].

Chapter 3

Supercritical Assisted Atomisation

Here we return to one of the variations of the supercritical fluid methods which has lately shown a lot of promise for mass-producing nanoparticles of small size at a comparatively low cost. A process called Supercritical Assisted Atomisation (SAA) or Nebulisation is used to generate aqueous nanodroplets containing the dissolved product, which, once dried, form a fine powder composed of hollow nanospheres [6, 54].

3.1 Principle

Nebulisation using supercritical or near-critical CO₂ is a well-studied topic. A solution is combined with carbon dioxide at high pressure (from about 4 to 8 MPa) to form a mixture with low surface tension and high viscosity. Gaseous CO₂ is highly soluble in water at high pressures (1.6 mol% at 63°C and 10.3 MPa [51]), which means that a large quantity dissolves into the solution. This mixture is then expanded rapidly through a capillary flow restrictor. Aided by the change in properties, the sudden reduction in pressure causes microbubbles to form, expand and then burst in very rapid succession, dispersing a plume of micro- and nanodroplets. Thus the droplets are formed in two distinct stages. In the first instance, pneumatic atomisation breaks down the fluid upon leaving the injector, and in the second, the newly-formed primary droplets are split by CO₂ expansion into smaller secondary droplets (decompressive atomisation). This technology has been used primarily in the medical sector for dispersion of inhalation drugs, such as those used to treat

asthma, but its potential for the large-scale production of solid nanoparticles for other applications is under investigation [3, 6, 42, 51, 54].

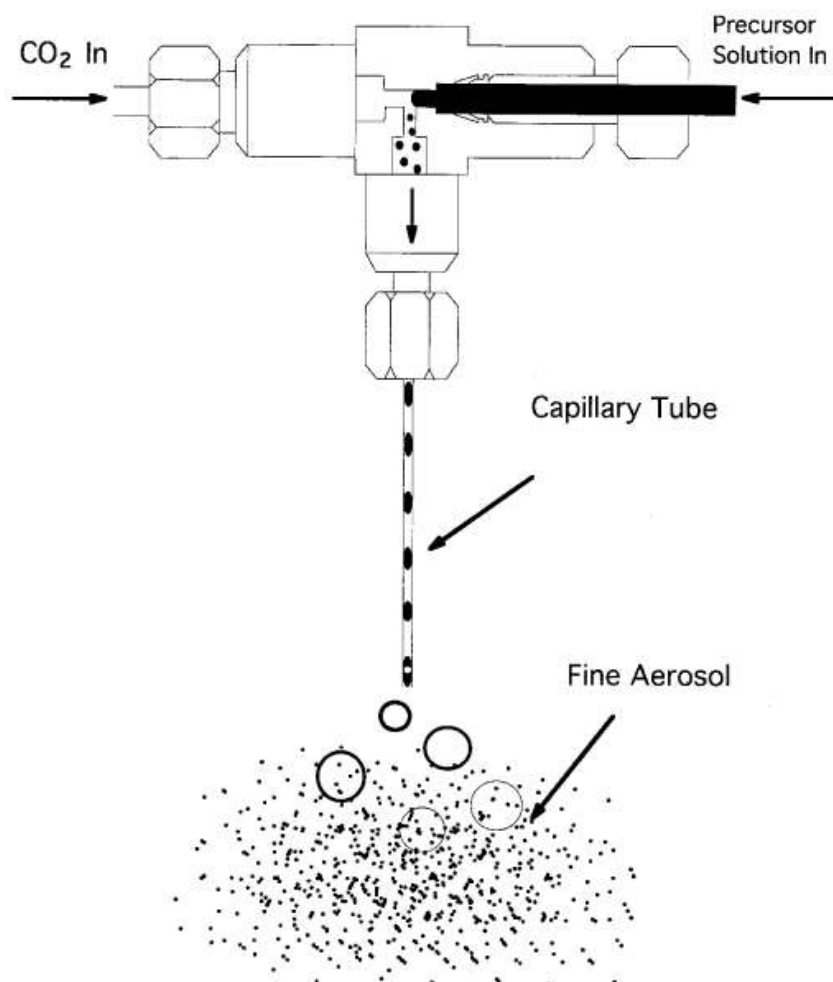


Figure 3.1: Nebulisation process using zero volume die and capillary restrictor [51]

The use of supercritical fluids (SFs) offers numerous benefits over other conventional methods for forming nanodroplets and nanoparticles. A high level of control can be exercised over the process by varying the pressure and temperature, as well the concentration of solvent fluid. SFs are associated with significantly larger mass transfer rates than normal solvents. SAA forms small particles ($< 3 \mu\text{m}$) with a higher efficiency compared to conventional microfluidisation techniques. In ultrasonic nebulisation localised heating can occur, damaging heat sensitive materials, an issue which is avoided in SAA. This means that droplets produced by SAA can be potentially dried even at ambient air temperatures [39, 51].

When comparing various supercritical technologies, SAA holds the advantage that the working material is dissolved in water rather than directly in CO₂ as is the case in RESS technology. Since a significantly larger range of substances are soluble in water than in supercritical CO₂, the technology is more versatile [51].

CO₂ is the working medium of choice, since it is non-toxic, non-flammable, readily available, relatively environmentally safe, and has a low critical temperature and pressure. In some cases N₂ is used instead of CO₂ [39].

3.2 The development of SAA and CASND

At the turn of the millennium, Sievers and other researchers from the University of Colorado proposed that small bubbles and droplets caused by the rapid decompression of supercritical CO₂ dissolved in an aqueous solution could be dried at low temperatures, representing an improvement on traditional spray drying [52, 51]. This process came to be known as Carbon Dioxide Assisted Nebulisation with Bubble Drying (CAN-BD), and uses a micrometric volume tee for partial mixing and a capillary tube for expanding the solution. Uniform particles with diameters of less than 3 μm can be thus generated [49]. Subsequently, work began by researchers at the university of Salerno to further develop SAA, using a packed column to ensure the full mixing of CO₂ and the aqueous solution. Most of the early research focused on creating micro- and nanoparticles for drug delivery [41, 6].

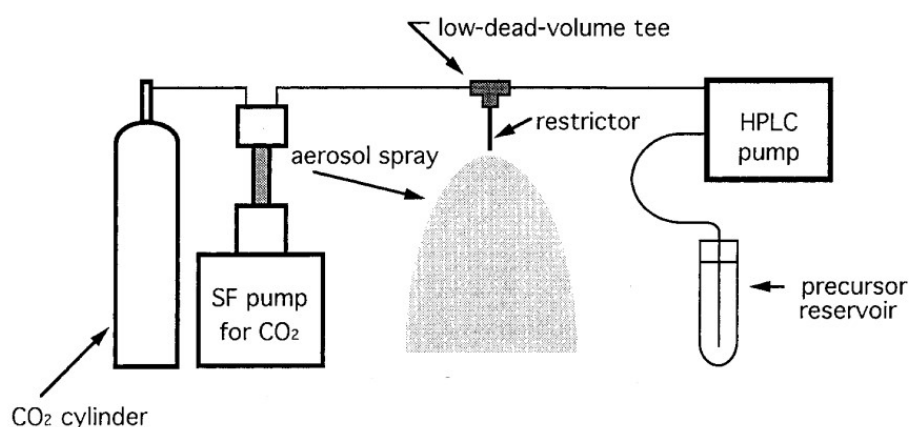


Figure 3.2: Siever's original arrangement for continuous nebulisation [51]



Chapter 4

Conclusion

Having given the necessary background in both food drying and nanoparticle production, it should be clear why the CASND technology is of interest as a topic of research. Its clear advantages over equivalent technologies, both in its simplicity and scalability are recapitulated:

- A large number of materials can be processed
- Particles can be dried at lower temperatures
- CASND has low energetic requirements
- High nanoparticle production efficiency
- The process can be finely controlled.
- No toxic or significantly environmentally harmful solvents are required
- The technology is easily scalable

Because it is a new technology that still under development, much is yet to be investigated before it can be implemented commercially. Research conducted now can help promote and speed up its acceptance as a "go to" technology for use in the food industry of the future.

Now that the context has been given, the author will move on to describe the specific equipment for producing, drying and separating nanoparticles and his specific research in the next section.



Part II

Practical Part



Chapter 5

Introduction to the CASND project

Building on previous work by researchers in the Czech Republic, an investigation was launched to examine the potential of using CASND technology in the field of food processing. The project - a collaboration between the Food Research Institute Prague (FRIP), the Czech Technical University (CTU) and industrial partners - involved operating a laboratory-size dryer whilst manipulating various parameters. The goal is to optimise the process of producing nanoparticles in preparation for eventually scaling-up to industrial production. Various designs have been tested and progressively improved [54].

The author of this thesis was involved in the project during the measurement phase of one iteration of the experimental dryer's design, and in the subsequent processing and evaluation of the data.



Figure 5.1: Laboratory setup in arrangement A

Chapter 6

Problem analysis: preliminary design of the dryer

Here, the steps used for the preliminary design of the dryer based on certain given parameters are presented. Initially the psychometric properties of the drying air are deduced along with the amount of evaporated water, which enables the estimation of the required quantity of drying air. Subsequently the residence time of particles in the dryer is found.

This phase of the design was realised by the author's supervisor, which the author then studied to familiarise himself with the design process.

6.1 Initial data

- Capacity of the drying chamber: approx. 1.5 m^3
- Mass flow rate of drying air: 400 to $1000 \text{ m}^3/\text{h}$
- Maximum temperature of entering air: 60°C
- Maximum mass flow rate of drying solution: $5\text{kg}/\text{h}$
- Mass flow rate of liquid carbon dioxide: approx. 0.25 to $0.5 \text{ kg}/\text{h}$
- Dried product concentration in solution (or suspension): 1 to 10% w/w

6.2 Preliminary design

6.2.1 Preliminary flow balancing

Drying air parameters

The water content, humidity and enthalpy of the drying air is calculated with the help of a Mollier diagram for various stages of the drying process. The initial values were estimated.

Before heating	state - 0
Temperature	$t_{A0} = 25^\circ\text{C}$
Moisture content	$x_{A0} = 0.01 \text{ kg/kg}$
Enthalpy	$h_{A0} = 51 \text{ kJ/kg}$
After heating	state - 1
Required temperature	$t_{A1} = 35 \text{ to } 60^\circ\text{C}$
Moisture content	$x_{A1} = 0.01 \text{ kg/kg}$
Enthalpy	$h_{A0} = 61 \text{ to } 87 \text{ kJ/kg}$
After evaporation	state - 2 (neglecting heat losses)
Working temperature	$t_{A2} = 25 \text{ to } 35^\circ\text{C}$
Moisture content	$x_{A1} = 0.014 \text{ to } 0.020 \text{ kg/kg}$
Enthalpy	$h_{A0} = 51 \text{ kJ/kg}$
1kg of air removes	$\Delta x_A = 0.004 \text{ to } 0.010 \text{ kg water from solution}$

Quantity of evaporated water W from the solution (for the maximum flow rate)

Maximum water flow rate	$M_{0max} = 5\text{kg/h}$ (without CO_2)
Inlet solution concentration	$X_0 = 1 \text{ to } 10 \text{ wt}\%$
Outlet concentration estimate	$X_1 = 95 \text{ wt}\%$ (humidity $5 \text{ wt}\%$)

$$W = M_0 \times \left(1 - \frac{X_0}{X_1}\right) \quad (6.1)$$

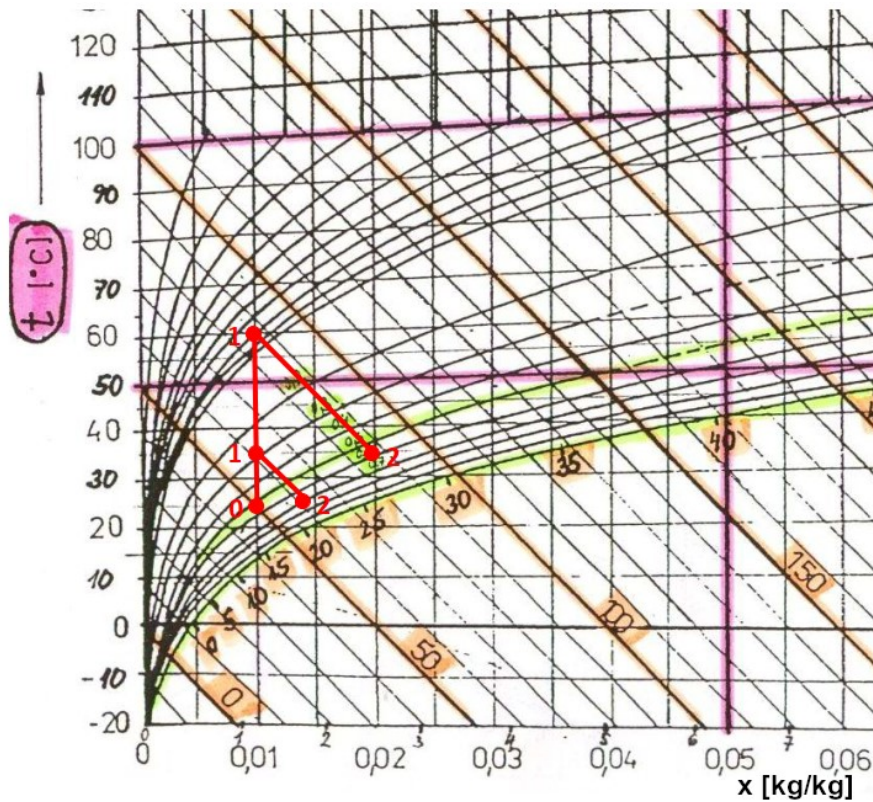


Figure 6.1: Mollier diagram for preliminary air calculations [23]

Minimum evaporation $W_{min} = 5 \times \left(1 - \frac{10}{95}\right) = 4.47 \text{ kg/h}$

Maximum evaporation $W_{max} = 5 \times \left(1 - \frac{1}{95}\right) = 4.95 \text{ kg/h}$

■ Required quantity of drying air for various operating conditions

$$\dot{M}_A = \frac{W}{\Delta x_A} \quad (6.2)$$

- a. Temperature of air $t_{A1} = 35^\circ\text{C}$ and solution concentration 1%

$$\dot{M}_A = \frac{4.95}{0.004} = 1238 \text{ kg/h} \quad \text{for } \rho_A \approx 1.2 \text{ kg/m}^3, \dot{V}_{A0} \approx 1032 \text{ m}^3/\text{h}$$

- b. Temperature of air $t_{A1} = 35^\circ\text{C}$ and solution concentration 10%

$$\dot{M}_A = \frac{4.47}{0.004} = 1118 \text{ kg/h} \quad \text{for } \rho_A \approx 1.2 \text{ kg/m}^3, \dot{V}_{A0} \approx 932 \text{ m}^3/\text{h}$$

- c. Temperature of air $t_{A1} = 60^\circ\text{C}$ and solution concentration 1%

$$\dot{M}_A = \frac{4.95}{0.010} = 495 \text{ kg/h} \quad \text{for } \rho_A \approx 1.2 \text{ kg/m}^3, \dot{V}_{A0} \approx 413 \text{ m}^3/\text{h}$$

d. Temperature of air $t_{A1} = 60^\circ\text{C}$ and solution concentration 10%

$$\dot{M}_A = \frac{4.47}{0.010} = 447 \text{ kg/h} \quad \text{for } \rho_A \approx 1.2 \text{ kg/m}^3, \dot{V}_{A0} \approx 373 \text{ m}^3/\text{h}$$

The calculated values roughly correspond to the required flow rate of drying air (i.e. 400 to 1000 m³/h).

6.2.2 Residence time of air in the laboratory dryer

From a calculation of particle drying time, which was less than 1 second, it was possible to estimate the required height of the dryer and compare the drying time with the particle residence time inside the dryer.

The dryer was built in 500 mm modules to allow its height to be reduced or increased according to produced particle size.

The average residence time of dried particles in the proposed dryer is, in the case of particles with the given size (around 500 nm), approximately equal to the average residence time of the drying air. This will be demonstrated later.

Given values

Diameter of the drying chamber $D = 500 \text{ mm}$
 Height of the cylindrical part of the chamber $H = 1500 \text{ mm}$

Volume of the drying chamber

$$V_{DC} = \pi \times \frac{D^2}{4} \times H = \pi \times \frac{0.5^2}{4} \times 1.5 = 0.294 \text{ m}^3$$

■ Residence time of air for various operating conditions

Residence time (τ) is calculated as the volume of the drying chamber (V_{DC}) over the volumetric flow rate (\dot{V}_A).

$$\tau_A = \frac{V_{DC}}{\dot{V}_A} \quad (6.3)$$

The same temperature and humidity conditions as above are assumed:

- a. $\tau_A = \frac{0.294}{1032} \times 3600 = 1.03 \text{ s}$
- b. $\tau_A = \frac{0.294}{932} \times 3600 = 1.14 \text{ s}$
- c. $\tau_A = \frac{0.294}{413} \times 3600 = 2.56 \text{ s}$
- d. $\tau_A = \frac{0.294}{373} \times 3600 = 2.84 \text{ s}$

For reference, the particle residence time in a spray dryer for milk (particles sizes of approx. 0.3 to 0.5 mm) is 10 to 30 s [23].

■ Checking whether the settling velocity of particles can be neglected

Settling velocity of a particle can be calculated by balancing the gravitational, buoyancy and viscous forces acting on it. In the present case, the particles are assumed to be perfectly spherical and sufficiently scarce that they don't interfere with each other.

Two scenarios are calculated, one where the particle density is $\rho_p = 1000 \text{ kg/m}^3$ and one where the density is $\rho_p = 1500 \text{ kg/m}^3$. The other values are as follows:

density of air	$\rho_A = 1.152 \text{ kg/m}^3$
particle diameter	$d = 500 \text{ nm}$
dynamic viscosity of air	$\mu = 1.88 \times 10^{-5} \text{ Pa}\cdot\text{s}$

The balance of forces acting on the falling particle at terminal velocity is:

$$F_{gravity} - F_{buoyancy} = F_{drag} \quad (6.4)$$

Substituting in the above mentioned values returns:

$$\frac{\pi \cdot d^3}{6} \cdot g \cdot (\rho_P - \rho_A) = C_D \cdot \frac{\pi \cdot d^2}{4} \cdot \frac{u_t^2}{2} \cdot \rho_A \quad (6.5)$$

Assuming the particles are falling in the Stokes' (laminar) regime ($Re \leq 0.2$), C_D is defined in terms of Reynolds number as:

$$C_D = \frac{24}{Re} \quad (6.6)$$

Where Reynolds number is

$$Re = \frac{u_t \cdot d \cdot \rho_A}{\mu} \quad (6.7)$$

Rearranging **Equation 6.5** in terms of u_t gives:

$$u_t = \frac{(\rho_P - \rho_A) \cdot d^2 \cdot g}{18\mu} \quad (6.8)$$

- Case 1, $\rho_P = 1000 \text{ kg/m}^3$

$$u_t = \frac{(1000 - 1.152) \cdot (500 \times 10^{-9})^2 \times 9.81}{18 \times 1.88 \times 10^{-5}} = 7.24 \times 10^{-6} \text{ m/s}$$

$$Re = \frac{7.24 \times 10^{-6} \times 500 \times 10^{-9} \times 1.152}{1.88 \times 10^{-5}} = 2.22 \times 10^{-7} \leq 0.2$$

- Case 2, $\rho_P = 1500 \text{ kg/m}^3$

$$u_t = \frac{(1500 - 1.152) \cdot (500 \times 10^{-9})^2 \times 9.81}{18 \times 1.88 \times 10^{-5}} = 1.09 \times 10^{-5} \text{ m/s}$$

$$Re = \frac{1.09 \times 10^{-5} \times 500 \times 10^{-9} \times 1.152}{1.88 \times 10^{-5}} = 3.33 \times 10^{-7} \leq 0.2$$

Thus, the settling velocities of particles of size 500 nm and densities of 1000 and 1500 kg/m^3 respectively are calculated to be $7.24 \times 10^{-3} \text{ mm/s}$ and $1.09 \times 10^{-2} \text{ mm/s}$.

Reynolds is recalculated for both cases to check that the particle falls in the Stokes regime.

Given how small the settling velocity when compared to the motion of air in the drying chamber, it can be neglected. Thus the average residence time of dried particles in the laboratory dryer can be considered to be equal to the average residence time of the drying air.

This also shows that particles can be pneumatically transported upwards, as is the case of in the dryer with geometry B, where air and smaller particles are aspirated upwards through the central column.

Chapter 7

Design proposal and realisation

In this section the author describes the laboratory drying system, including two designs for the dryer.

Whilst the author was not involved in the design of the dryer, which was conducted by researchers from the Department of Process Engineering and from the Food Research Institute Prague, he carefully studied the system and wrote the following description.

Conceptually, the dryer was designed as an experimental device for investigating the drying process by diverse measuring techniques.

In the first variant, referred to as geometry A, the dryer functions solely as a drying chamber, where the drying solution is mixed with air. In the second variant, geometry B, the drying chamber works simultaneously to remove water from the solution droplets and to extract the larger particles from the main air stream by cyclonic separation.

7.1 Two variations

The drying chamber itself consists of a large vertical cylinder with a flat cover at the top and a cone-shaped base underneath. The chamber is constructed

from three smaller cylindrical sections and the cone, joined end-to-end by flanges. There is an opening in the centre of the cover, four tangential entrances near the top of the sides and one opening at the bottom of the cone, besides a maintenance hatch for access and cleaning built into the wall of the middle cylinder. The numerous orifices in the chamber walls are for inserting diverse measuring probes and sensors. All the components of the chamber are made from stainless steel (DIN EN 1.4301).

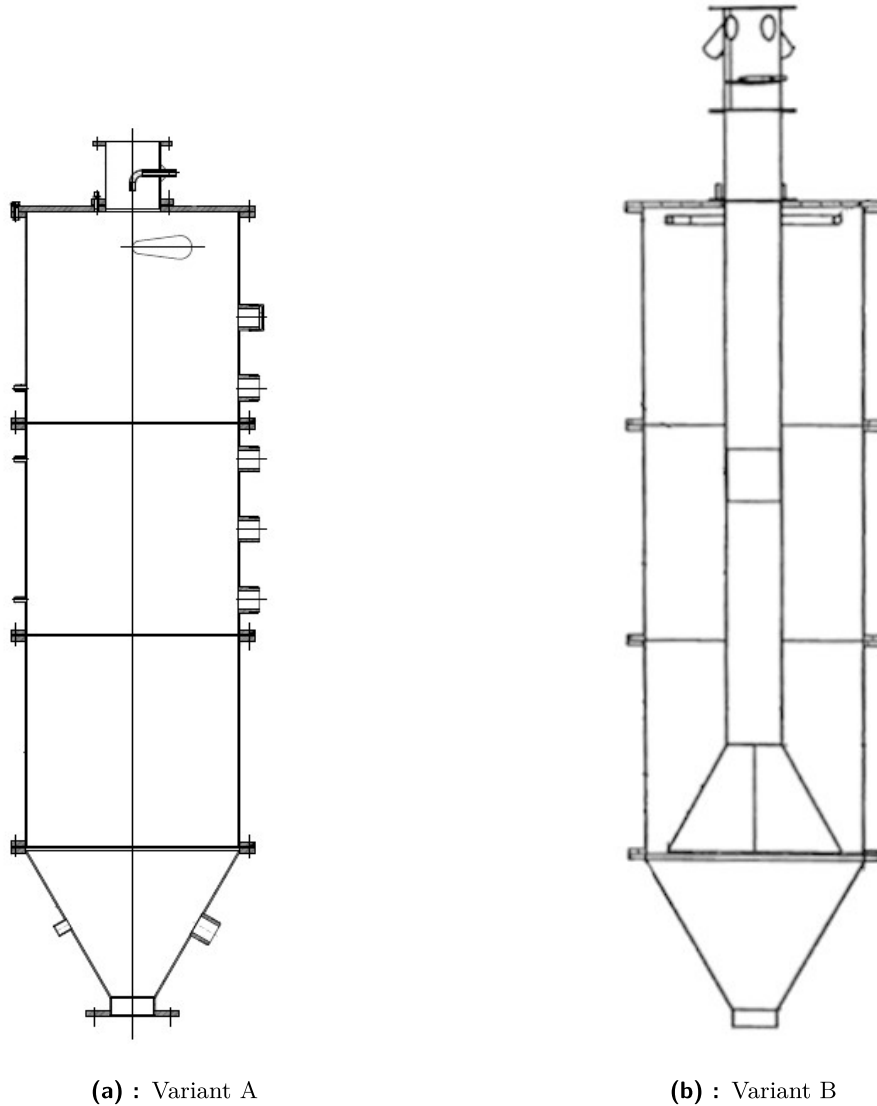


Figure 7.1: Assembly drawings of the two dryer geometries
(source: Vzduchotechnik, VÚPP, 2019)

In the case of geometry A, the hole in the centre of the top cover is used as the main inlet for air and the drying solution, and the tangential openings are used as auxiliary air inlets to induce helical motion. An adjustable valve is located in the pipe above the chamber at the point where the two inlet air

streams divide and enables the ratio of air flowing through the two entrances to be adjusted (see **Figure 5.1**). Air and dry matter leave the chamber through an opening at the bottom of the cone.

Geometry B is more complex since here the chamber functions simultaneously as a dryer and a cyclonic separator. It features an additional tube which runs vertically down through the centre of the chamber from the opening in the top cover and is connected to an inverted cone with angled blades on its outer side. Air enters the chamber through the tangential openings. It immediately mixes with the solution which is sprayed through expansion nozzle inserted through the cover. It then rotates around the cylinder, moving progressively downwards until it is sucked back up through the central pipe and out through the top opening, carrying with it the smaller-sized particles. The larger particles, being forced outwards to the chamber wall by centrifugal force, fall to the bottom of the cone from which they leave the chamber. For the laboratory tests, a small stainless steel vessel was fixed to this opening, though for industrial scale a pneumatic transport system is recommended.

The assembly is supported by a four-pillared frame, and a platform at shoulder-height allows access to the maintenance hatch and to the top cover.

■ 7.2 Realisation

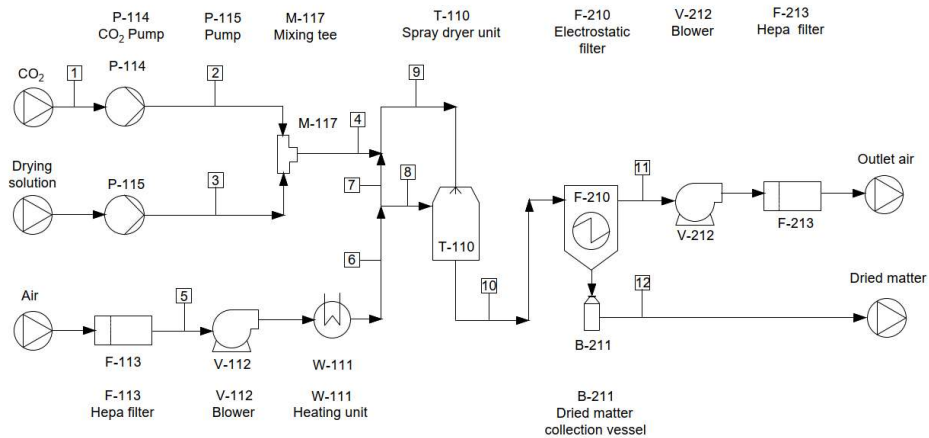
■ 7.2.1 Process overview

The dryers are connected to a system of devices and technologies that ensure a supply of air, CO₂ and solution, as well as regulate the temperature. The Process Flow Diagrams (PFD) are displayed in **Figure 7.2** and in larger format in **Appendix A**.

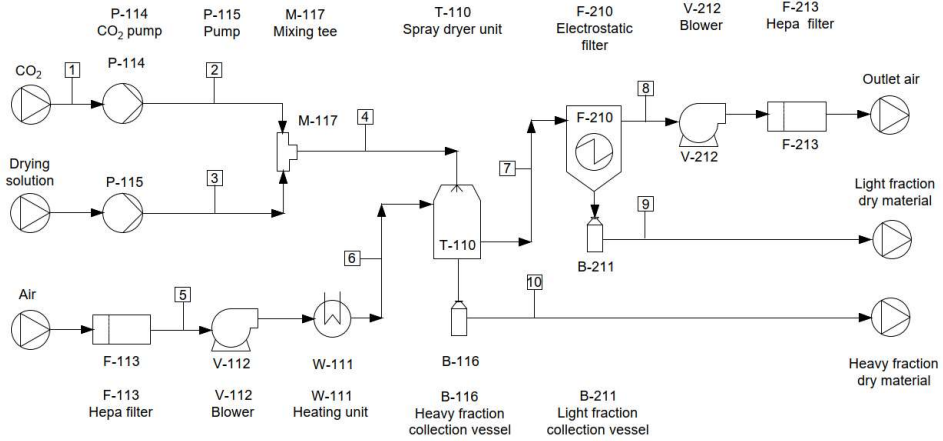
■ 7.2.2 Processing units

A list of equipment used in the dryer system is displayed in **Table 7.1**.

The heating unit, manufactured by Vzduchotechnik is composed of six heating coils inserted into a section of the inlet air duct. Each coil can be



(a) : Variant A



(b) : Variant B

Figure 7.2: Process Flow Diagrams for both variants

switched on separately and has a heating duty of 3 kW, so in total the heating unit has a duty of 18 kW, which is more than sufficient to heat our demanded flow of air to a satisfactory temperature (10 kW is enough to heat 1000 m³ of air from 25°C to 60°C at atmospheric pressure). Air is heated as it flows around the coils.

7.2.3 Working substances

The four substances treated in the dryer system are dry air, CO₂, water and the material for drying.

Air is obtained from the environment, filtered, heated before being intro-

Code	Unit	Manufacturer	Name
T-110	Spray dryer unit	custom	/
F-113	HEPA filter	Vzduchotechnik	/
V-112	Inlet blower	Vzduchotechnik	PV 90
V-212	Outlet blower	/	/
B-211	Electrofilter	Vzduchotechnik	Aerofog KE1
W-111	Heating unit	Vzduchotechnik	/
F-213	HEPA filter	/	/
P-114	CO ₂ regulating pump	custom	/
P-115	Solution pump	Hydra-Cell	319758
M-117	Mixing tee	custom	/
B-116	Heavy fraction collector	/	/
B-211	Light fraction collector	/	/

Table 7.1: List of processing units

#	Component	Notes
1	Water	Liquid and vapour state
2	CO ₂	From high pressure cylinder
3	Air	Filtered from the environment
4	Dry Matter	Mixed with water, absent during trials

Table 7.2: List of substances

duced into the spray dryer. It is then filtered again twice before being ejected into the environment. It remains in gaseous form throughout, and does not undergo any large changes in pressure.

Carbon dioxide is released from a cylinder where it is stored at approximately 6 MPa and cooled before being mixed with the solution stream. Once released through the capillary pipe into the drying chamber, the CO₂ expands and is transported away with the air. Despite beginning at near-critical values, most CO₂ undergoes no change of phase, although a small proportion dissolves in the solution.

Water enters the system by two different means. Water vapour is carried into the system with the air intake. The solution for dehydrating consists of the product material dissolved in water. This mixture is combined with CO₂ and sprayed into the dryer. The majority of water evaporates into the air and is carried off with the other gases. A small part remains in the dried nanoparticles as moisture.

The material for drying precipitates in the drying chamber as water evaporates, forming nanoparticles that are collected either in the heavy fraction collection vessel (Variant B) or in the electrofilter (Variant A and B).

7.2.4 Process streams

#	Stream description	T [°C]	P [MPa]
1	Inlet of high pressure CO ₂	T _{atm}	≈ 6
2	Regulated CO ₂	≈ T _{atm}	≈ 5
3	Water/drying mixture inlet	T _{atm}	P _{atm}
4	Emulsion of CO ₂ in mixture	≈ T _{atm}	5
5	Air inlet at atmospheric conditions	T _{atm}	P _{atm}
6	Air after heating	≈ 60	≈ P _{atm}
7	Heated air separated for central inlet	≈ 60	≈ P _{atm}
8	Heated air separated for side inlets	≈ 60	≈ P _{atm}
9	Nebulised solution in air	≈ 60	≈ P _{atm}
10	Nanoparticles and gas mixture	≈ 60	P _{atm}
11	Mixed gases	≈ 60	≈ P _{atm}
10	Dried nanoparticles	≈ 60	P _{atm}

Table 7.3: List of streams - Geometry A

#	Stream description	T [°C]	P [MPa]
1	Inlet of high pressure CO ₂	T _{atm}	≈ 6
2	Regulated CO ₂	≈ T _{atm}	≈ 5
3	Water/drying mixture inlet	T _{atm}	P _{atm}
4	Emulsion of CO ₂ in mixture	≈ T _{atm}	5
5	Air inlet at atmospheric conditions	T _{atm}	P _{atm}
6	Air after heating	≈ 60	≈ P _{atm}
7	Mixed gases and smaller nanoparticles	≈ 60	≈ P _{atm}
8	Mixed gases	≈ 60	≈ P _{atm}
9	Smaller nanoparticles	≈ 60	P _{atm}
10	Larger nanoparticles and microparticles	≈ 60	P _{atm}

Table 7.4: List of streams - Geometry B

Materials are transported around the system by pipes and ducts.

The diameter of the pipe where air temperature and velocity are measured after heating (stream 6) is 130 mm. The diameter of the pipe where humidity and temperature of air are measured after passing through the electrofilter (stream 8) is 100 mm.

7.2.5 Measurement equipment system control

The collection of continuously measured data and control of the air temperature were designed to be carried out by Arduino miniprocessor. This solution was chosen due to its simplicity and low cost. The initial proposal for the arrangement is represented in **Figure 7.3**.

The properties measured continuously are temperature and relative humidity.

In the initial design measuring pressure drop in the drying chamber was also proposed.

Relative humidity is read at two points: at the air inlet prior to heating, and directly after the electrofilter.

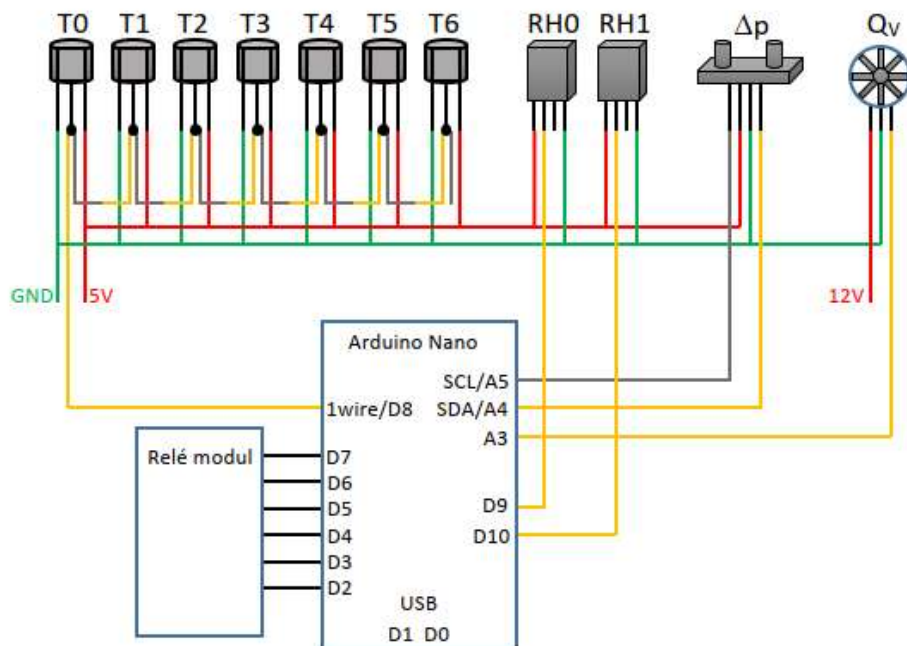


Figure 7.3: Proposal for sensor connections [24]

The temperature of air is continuously measured between the heating coils and the dryer and at six points inside the drying chamber. Ambient temperature should be read separately at the start of each experiment.

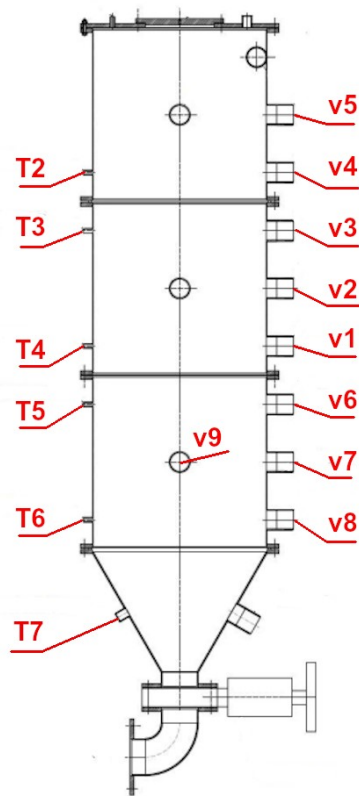


Figure 7.4: Location of measurement points in the drying chamber [adapted from Vzduchotechník, VÚPP, 2019]

The air velocity can be measured at various points in the drying chamber and in the system ducts.

The location of the temperature and humidity sensors, as well as the points where air speed was measured can all be read from **Figures 7.4 and 7.5**.

Control of the air temperature was effectuated by switching on and off the six coils of the heater depending on the temperature of air leaving the heater.

■ 7.2.6 Pressure losses

An analysis of the expected pressure drop in the air stream was conducted by the author's supervisor. The purpose was to choose an appropriate blower

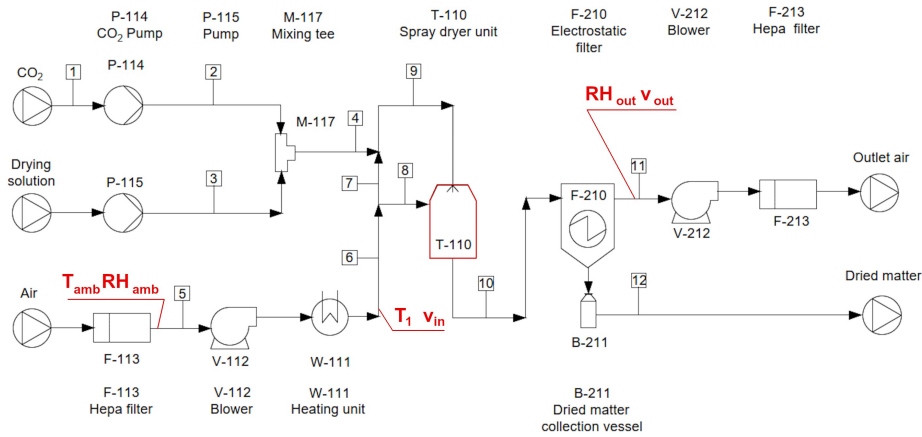


Figure 7.5: Measurement locations in system

arrangement and find the working point (flow rate and pressure) of the system.

The system was broken down into individual section and was analysed according to standard fluid dynamic principles and data from the equipment manufacturers (see **Figure 7.6**).

Eventually, a configuration of two blowers connected in parallel was used, one at the beginning of the system to raise the pressure, and one at the end to lower it. The blowers were converted from other equipment. Both blowers needed to operate at full capacity for the maximum flow rate through the system to be reached.

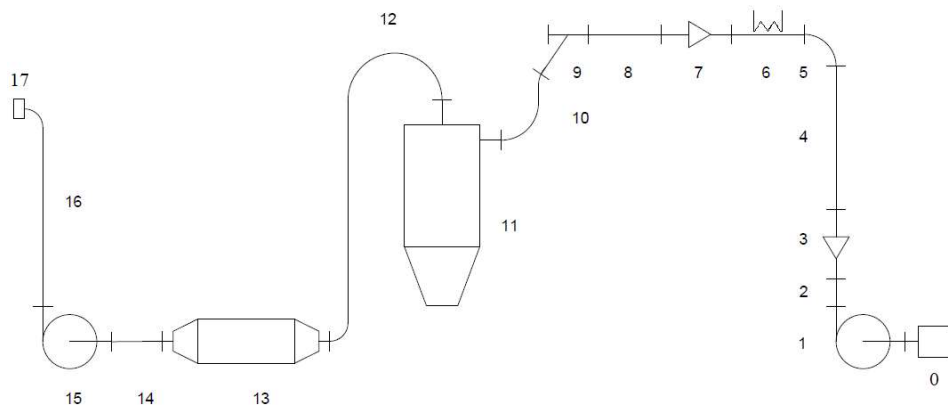


Figure 7.6: Estimating pressure losses in Variant B

Description of figure 7.6

- 0 Hepa filter
- 1 Inlet blower
- 2 Pipe DN200×1000
- 3 Expansion unit
- 4 Duct 200×400×1500
- 5 90°Elbow bend 200×400 R380
- 6 Heater 200×400×900 + coils
- 7 Reduction unit
- 8 Pipe DN140×500
- 9 Tube DN40×1100
- 10 90°Knee bend DN40×1100 R100
- 11 Drying unit
- 12 Pipe DN100 various geometries
- 13 Electrofilter
- 14 Pipe DN100 various geometries
- 15 Outlet blower
- 16 Pipe DN100×5800
- 17 Grill

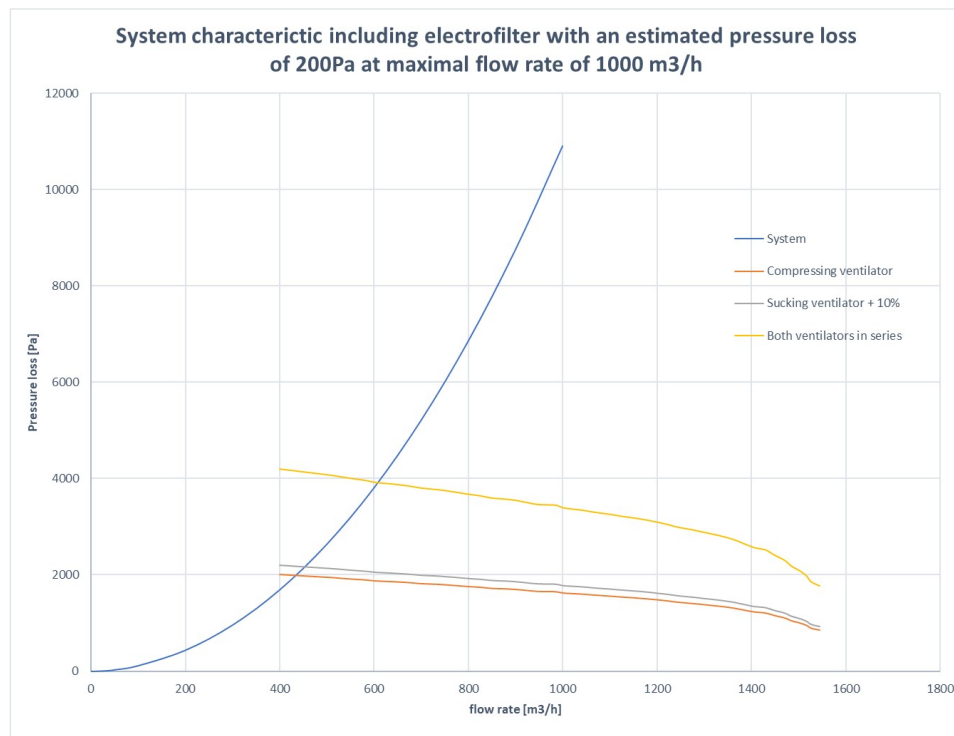


Figure 7.7: System characteristic for Variant B

From **Figure 7.7** we can see that the working point of the system when both blowers are connected in series is at an approximate flow rate of 600 m³/h and pressure drop of 4 kPa.



Chapter 8

Measurement procedure



8.1 Introduction

The experimental dryer set-up from the previous chapter was constructed and operated in collaboration with the Food Research Institute Prague. Previously, various experiments had been conducted relating to the size of nanoparticles produced by different expansion nozzles, as well as other tests.

The author joined the project whilst measurements were being taken to understand how the various components flow through the system. The purpose was to optimise future designs of the spray dryer by determining the way air moves inside the drying chamber. The data was processed by the author of the thesis, with advice from his supervisor and Ing. Hladíková, a doctoral student in the department of Process Engineering, who oversaw the beginning of the measurement phase. The author was present for the later experiments on Variant B, and the outcome of his work is presented in the following chapters.



8.2 Measurements

In total 11 measurements were conducted to read the air velocity, temperature and humidity at various points throughout the system under different

conditions. The first was conducted on configuration A, and the next ten on configuration B; both variants are described in Chapter 7. Experiments 1 to 9 were conducted only with air circulating in the dryer, and no solution or CO₂ was present. During the last two experiments, water mixed with CO₂ is added and "dried".

For configuration B, various arrangements with the blowers were also tried with air as the only working medium. The system was tested with just the inlet blower (Measurement 2), then with only the outlet blower (Measurement 3), then with both in parallel. The power of the outlet blower can be regulated, the impact of which was tested in Measurement 8.

For the Variant B dryer, the blades on the inner cone can be angled to interact with the air flow. In Measurements 2 to 5, these blades were angled at 50° from the horizontal, and for the following they were angled at 65°.



(a) : Drying chamber - top

(b) : Drying chamber - bottom

Figure 8.1: Location of openings in the drying chamber [22]

When measuring airflow with the anemometer, readings can be taken with the probe aligned to the pipe axis, or angled. Angling the probe at, for example, 90° gives an indication of whether the air is flowing directly through the pipe, or else helically. It can also prove the presence of turbulence. Similarly, when the probe is inserted into the drying chamber, the local velocity is measured in the tangential and axial directions. During the measurement on Variant A, eight different angles were measured at each position. For the rest of the measurements where air speed was measured, readings were only taken for the tangential and axial velocity.



Figure 8.2: Measurement location in the inlet pipe

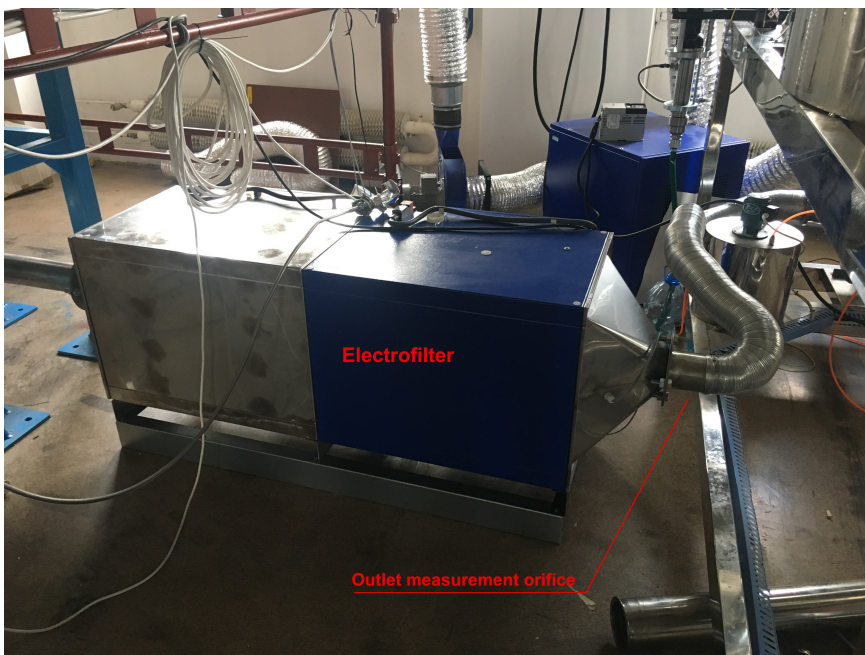


Figure 8.3: Measurement location in the outlet pipe

An overview is presented in **Appendix B**.

During the course of the experiments, temperature and humidity at the

inlet were measured continuously and the readings logged in the system's computer.

Air velocity was measured by inserting a hot-wire anemometer probe (data logger: AHLBORN ALMEMO 2450-1R02; probe: AHLBORN ALMEMO FVAD35TH4) into the air current through an orifice. The velocity was measured and averaged over a period of sixty seconds at various depths.

More information about the quantities measured is laid out in **Chapter 7**.

8.3 Protocol

During the readings, the following protocol, devised by Ing. Skočilas, PhD, and Ing. Hladíková, was observed (the text in *italic* describes steps that concern only some of the readings):

1. Switch on the blowers *and heater*, measure the atmospheric conditions (temperature, humidity, pressure)
2. Wait for the values to settle
3. *Begin to pump CO₂ and the drying solution (water) into the mixing valve and then into the drying chamber*
4. Measure the velocity fields required for calculating the inlet and outlet flow rate of air: the probe is inserted into the appropriate opening and readings taken 2 cm at a time
5. Measure the velocity field at opening 5: the hexagonal nut covering is removed, and the probe is inserted through the rubber seal
6. Wait 5 minutes for the air flow to stabilise
7. The probe is inserted 2 cm into the chamber (measured from the wall) and readings are taken with the probe angled at 0° and 90°
8. Move the probe 2 cm further in and again measure the air velocity at both angles (the probe can be inserted to a depth of 16 cm from the chamber wall)
9. proceed likewise for the other openings

8.4 Results and evaluation

The measurement phase was hindered by numerous issues. Besides technical problems such as power outages, various mistakes during the measurement meant that certain parts of the data are incorrect or unusable. Some of the errors are part of the unavoidable troubleshooting of a new system, and some could have been avoided had the author been sufficiently trained prior to being requested to supervise the process.

Listed below are the problems that arose during the week that the author was present at the measurement (Measurements 9, 10 and 11).

- A electricity outage to the heaters meant that the measurement had to be postponed until an electrician could fix the connection.
- The humidity and temperature sensors at the outlet malfunctioned, and therefore the continuous readings from after the electrofilter are incorrect. The issue with the humidity sensor was diagnosed thanks to the author's mass balance calculations.
- The anemometer probe used to measure air speed was being operated at, and sometimes above, its design parameters. According to the datasheet, temperature difference is no longer compensated above 50°C, which is the temperature of the air which was being measured, although its maximum operating temperature is still 70°C. The maximum air speed that it can measure is 20 m/s, a value which was often passed, meaning that there are many gaps in the measurements. There is no information on the effects of air humidity on the probe.

Despite these setbacks data was obtained, particularly during **Measurement 11**, which could later be used to model the mass balance of the system and **Measurement 4** used to qualify the CFD models.

A sample of the results is included for the case of Measurement 11. **Figure 8.4** shows the overall data relating to the experiment, and **Figure 8.5** shows the measured velocity profiles at various openings.

GENERAL	measurement	11th measurement
		overseen by measurement date
CONDITIONS	temperature [°C]	X
	humidity [%]	X
	inlet temperature [°C]	65.25
	inlet humidity [%]	46
MEDIUM	outlet humidity [%]	22.5
	air	YES
	water	YES
	quantity of water	20 ml/min
	CO2	YES
EQUIPMENT	quantity of CO2	20 ml/min
	configuration A	NO
	configuration B	YES
	valve angle [°]	X
	number of blades	8
	angle of blades [°]	50
	inlet blower	YES
outlet blower	YES	
FLOW RATES	power of output blower [%]	100
	opening after the temperature sensor	YES
	opening after the valve	NO
	opening after the filter	YES
	opening after the temp. sensor (pipe diameter) [mm]	130
MEASUREMENTS	opening after the filter (pipe diameter) [mm]	100
	duration of measurement in each position [min]	1
	1st opening	NO
	2nd opening	NO
	3rd opening	YES
	4th opening	YES
	5th opening	YES
	6th opening	NO
	7th opening	NO
	8th opening	YES
	9th opening	YES
	large opening (outer cone) 10th opening	NO
small opening (outer cone) 11th opening	NO	
PROBE ANGLE [°]	0	YES
	45	NO
	90	YES
	135	NO
	180	NO
	225	NO
	270	NO
	315	NO

Figure 8.4: Results from Measurement 11 [22]

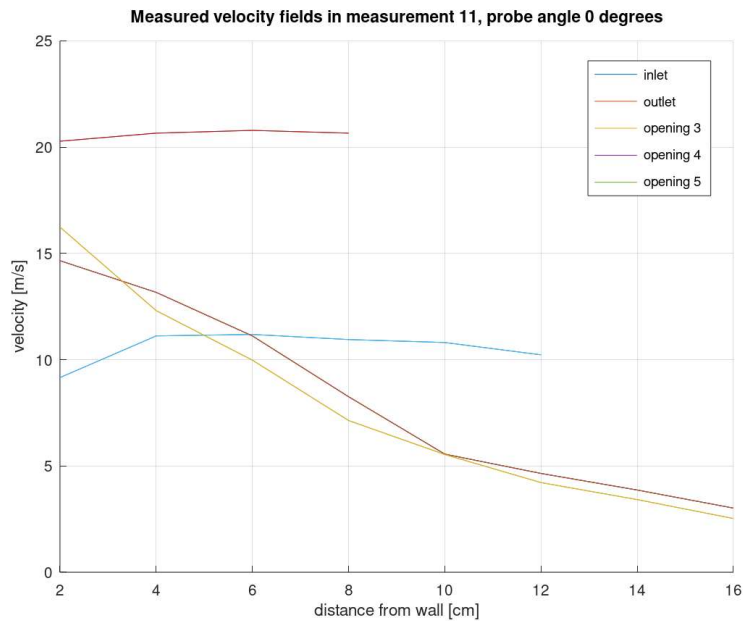


Figure 8.5: Measured velocity profiles from Measurement 11

For the mass balance, the inlet velocity of air, the relative humidity of the air, and the inlet flow of the other components are required to be known. Since no solution was dried, only water, processing this information became easier. Outlet values are useful for validating the model, and since the outlet temperature and humidity sensors were erroneous, the author was required to estimate these values.

The continuous measurements of temperature and humidity were recorded by computer throughout the duration of the experiment, from the moment that the blowers and heaters were activated through to when they were switched off. This data was saved in a text file and retrieved by the author for later analysis.

Calculated air speeds from the CFD model are compared against the measured values from the experiments. While the measured data is not complete (particularly in locations where the air speed was greater than 20 m/s), there are enough reference points to qualify the model. For Measurement 1 (from which data was obtained about the air flow in geometry A), the author suspects that the value of air flow was either wrong, or misreported, since the simulated model demonstrates significantly different characteristics at this air speed. The author hypothesises that the sensor measuring air velocity in the pipe leading to the top inlet to the chamber was shielded by the valve which is positioned in front of the sensor. However later work showed that the overall value of air flow must have been incorrect as well (see **Chapter 10**).



Figure 8.6: Rotated valve from configuration A may have impeded the correct measurement of air flow



Figure 8.7: Location of the valve and anemometer probe



Chapter 9

Mass balance model

The author used the data obtained during the experiments to produce a model for calculating the flow-rates of components in the system.

The purpose was to provide the author with an understanding of how the various substances flow inside the system. This information was then used for identifying issues in the system and estimating air leakage.

The concept behind a mass balance model is to use knowledge of a given system and relevant physical principles as well as data measured at the inlets to calculate the theoretical flow rate of each component in every stream.

The author's first attempt at modelling the mass balance was written in Microsoft Excel, which he then transcribed and expanded as a Matlab script. The Matlab script includes functions for calculating between absolute and relative humidity from empirical relations, short-cutting the need for manually reading values from psychrometric charts.



9.1 Explanation of the model

The full scripts are included for reference in **Appendix C**.

The approach employed was provided to the author during the course "Computer Aided Design" [14]. The network of streams and operating units is represented as a system of linear equations, and the remaining relationships are created from auxiliary information about the components or streams in order to obtain a problem with a single solution. This problem is written in the matrix form:

$$\mathbf{A} \cdot \mathbf{x} = \mathbf{b} \quad (9.1)$$

where \mathbf{A} is the so-called Matrix of Coefficients, \mathbf{b} is the Vector of Residues, and \mathbf{x} is the vector of flow rates which needs to be found.

The problem is resolved by simple inversion:

$$\mathbf{x} = \mathbf{A}^{-1} \cdot \mathbf{A} \cdot \mathbf{x} = \mathbf{A}^{-1} \cdot \mathbf{b} \quad (9.2)$$

The script is divided into three layers. In the first, data specific to each experiment is input. The second layer, designed as a function called up by the first script defines the geometry of the system based on the outlay from the process flow diagram. The third layer, a function within the second script, is the mathematical solution of the matrix problem.

9.1.1 First layer - Experiment data

Here the author input the parameters of the system during the relevant measurement. The necessary values are summarised in **Table 9.1**. This part of the script is specific to each measurement, and the value of each parameter should be appropriately defined.

The inlet air flow rate was estimated from the measured velocity profile in the duct. These velocities are integrated numerically across the area of the pipe using the rectangle rule on a rotated surface. In the case where the velocity is consistent at all points equidistant from the axis, the integration can be expressed as a function of the radius (**Equation 9.3**).

$$dV = v(A) \cdot dA = v(r) \cdot 2\pi \cdot r \cdot dr \quad (9.3)$$

Value	Unit	Description
Tamb	°C	Ambient temperature
Pamb	Pa	Ambient pressure
Vco2	ml/min	Inlet flow rate of CO ₂
Vsol	ml/min	Inlet flow rate of solution
M_lfrac	kg/h	Mass flow rate of humid dry matter, electrofilter
M_hfrac	kg/h	Mass flow rate of humid dry matter, cyclone
RH5	/	Relative humidity at inlet before heating
T6	°C	Moist air temperature after heating
V6	m ³ /s	Flow rate of air at inlet
X9	kg _w /kg _{dm}	Moisture content of light fraction - dry basis
X10	kg _w /kg _{dm}	Moisture content of heavy fraction - dry basis
D6	m	Inlet pipe diameter
dens_sol	kg/m ³	Density of solution
dens_co2	kg/m ³	Density of liquid CO ₂

Table 9.1: Mass balance input parameters

where V is the volumetric flow rate, A is the area, and r is the radius from the centre of the pipe.

The script used to calculate the volumetric flow rate for the inlet pipe and likewise for the outlet pipe are included in **Appendix C**.

All the necessary values are fed directly into the second layer.

9.1.2 Second layer - System geometry

The system geometry is represented graphically by the Process Flow Diagram, and so this part of the script should be edited only in the case when the system is modified (such as the difference between Variant A and Variant B).

In the first instance, the input parameters are recalculated to properties that are more appropriate for further processing. Inlet volumetric flow rate is converted to mass flow rate using empirical equations to define density as a function of humidity and temperature [13, 17, 38].

Volumetric flow rates of CO₂ and the solution for drying are converted to mass flow rates.

The flow rate of water vapour in the air and in the separated nanoparticulate matter is derived from humidity and water content.

In the next step, auxiliary equations are composed from information known about the system. These are required, since the system is not fully defined by the boundary conditions. These relations are based on values defined in the first layer.

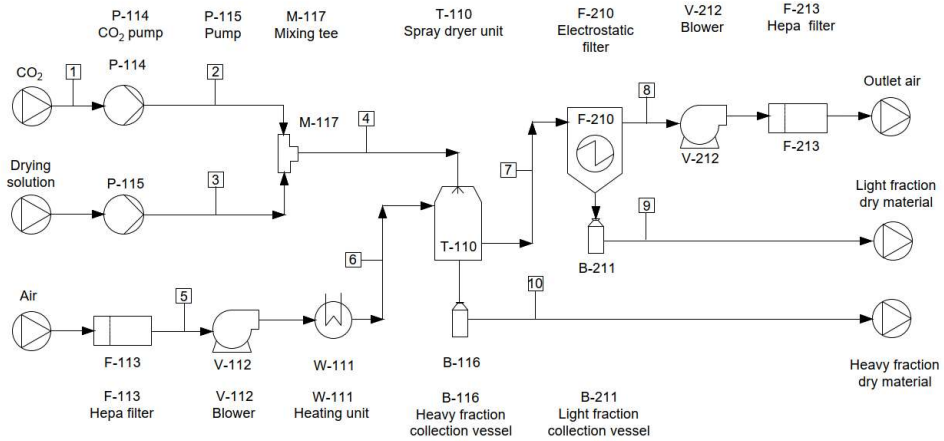


Figure 9.1: Stream arrangement in Variant B (PFD)

The relations used for geometry B are summarised below:

- reference stream, flow rate of water in stream 3
- stream 3, ratio of dry matter to water
- stream 6 (or 5), ratio of water to air
- dry matter, ratio of the separated light fraction to the heavy fraction
- ratio of water in stream 3 to air (stream 6)
- ratio of CO₂ (stream 1) to water (stream 3)
- stream 9, ratio of water to dry matter
- stream 10, ratio of water to dry matter

Next, the Incidence Matrix (IM) is determined, showing which streams connect with which processing unit.

Subsequently, the Table of Data (TD) is similarly defined, showing which components are present in each stream.

These two matrices, along with the auxiliary equations, are fed the thirds layer of the script.

■ 9.1.3 Third layer - Solver

In the third layer, an algorithm combines the given data to produce the Matrix of Coefficients and Vector of Residues. This process is equivalent to defining a system of linear equations, which is subsequently solved.

The number of auxiliary equations must be such that the number of total equations (the number of rows in the MC) is equal to the compounded number of components in each stream (number of columns).

This problem is solved by simple inversion and the flow rates of each component in every stream are obtained. This information is then entered into a table for ease of reading, and this table is returned to the first layer to be displayed.

■ 9.2 Results and discussion

■ 9.2.1 Modelling Measurement 11

In practice, the author used the model to calculate flow through the drying system in the case of Measurement 11, which corresponds to the set-up of Variant B where only water is mixed with CO₂ and sprayed into the dryer (see **Appendix B**). The author was present when the measurements were taken, and has access to the necessary data.

The list of streams from **Chapter 7** is reminded (**Table 9.2**), as well as the list of components (**Table 9.3**) and the list of units (**Table 9.5**).

#	Stream description	T [°C]	P [MPa]
1	Inlet of high pressure CO ₂	T _{atm}	≈ 6
2	Regulated CO ₂	≈ T _{atm}	≈ 5
3	Water/drying mixture inlet	T _{atm}	P _{atm}
4	Emulsion of CO ₂ in mixture	≈ T _{atm}	5
5	Air inlet at atmospheric conditions	T _{atm}	P _{atm}
6	Air after heating	≈ 60	≈ P _{atm}
7	Mixed gases and smaller nanoparticles	≈ 60	≈ P _{atm}
8	Mixed gases	≈ 60	≈ P _{atm}
9	Smaller nanoparticles	≈ 60	P _{atm}
10	Larger nanoparticles and microparticles	≈ 60	P _{atm}

Table 9.2: Reminder of the List of Streams - Geometry B

#	Component	Notes
1	Water	Liquid and vapour state
2	CO ₂	From high pressure cylinder
3	Air	Filtered from the environment
4	Dry Matter	Mixed with water, absent during trials

Table 9.3: Reminder of the List of substances

Given the absence of drying material in the water, it is clear that no nanoparticles were produced during this measurement, and that the flow rate of dry matter will always be zero.

The first step is to input the initial parameters shown in **Table 9.4**. The value of temperature T6 was taken from the data measured by the computer. The temperature in the duct after the heater (stream 6) oscillated only very slightly around this value.

Value	Unit	Value
Tamb	°C	20
Pamb	Pa	101325
Vco2	ml/min	20
Vsol	ml/min	20
M_lfrac	kg/h	0.0
M_hfrac	kg/h	0.0
RH5	/	0.46
T6	°C	65.25
V6	m ³ /s	0.097269
X9	kg _w /kg _{dm}	0.05 (redundant)
X10	kg _w /kg _{dm}	0.05 (redundant)
D6	m	0.13
dens_sol	kg/m ³	998 (water at 20°C)
dens_co2	kg/m ³	140.65

Table 9.4: Mass balance input parameters for measurement 11

#	Unit	Notes
1	T-110	Spray Dryer
2	W-111	Heating Unit
3	P-114	CO ₂ regulating pump
4	B-112	Electrostatic Filter
5	M-117	Mixing tee

Table 9.5: Reminder of the List of processing units

The system configuration produces the Incident Matrix represented in **Table 9.6**. The value **1** represents a flow into the given unit, while a value of **-1** represents a flow out of the unit.

IM	Stream										
	1	2	3	4	5	6	7	8	9	10	
Unit	1	0	0	0	1	0	1	-1	0	0	-1
	2	0	0	0	0	1	-1	0	0	0	0
	3	1	-1	0	0	0	0	0	0	0	0
	4	0	0	0	0	0	0	1	-1	-1	0
	5	0	1	1	-1	0	0	0	0	0	0

Table 9.6: Incidence matrix for configuration B

Similarly, the author constructed the Table of Data (**Table 9.7**), showing which components are present in each stream.

TD	Stream									
	1	2	3	4	5	6	7	8	9	10
1	0	0	1	1	1	1	1	1	1	1
2	1	1	0	1	0	0	1	1	0	0
Unit 3	0	0	0	0	1	1	1	1	0	0
4	0	0	1	1	0	0	1	0	1	1

Table 9.7: Table of Data for configuration B

This information was then fed into the solver, along with the reference stream (**Table 9.8**) and necessary auxiliary equations (**Table 9.9**).

Str.	Cp.	Flow rate	Explanation
3	1	0.00033267	Mass flow rate of water in stream 3 [kg/s]

Table 9.8: Reference stream for measurement 11

Str.	Cp.	Ratio	Str.	Cp.	Explanation
3	4	0.00000	3	1	stream 3, dry matter over water
6	1	0.00665	6	3	stream 6 (or 5), water over air
9	4	0.00000	10	4	dry matter, light over heavy fract.
3	1	0.00231	6	3	water (stream 3) over air (stream 6)
1	2	0.14093	3	1	CO2 in over water (stream 3)
9	1	0.05000	9	4	stream 9, water over dry matter
10	1	0.05000	10	4	stream 10, water over dry matter

Table 9.9: Auxiliary equations for Measurement 11

The results, once the script is run, are displayed in **Table 9.10**.

Flow rates [kg]	Components				
	1 water	2 CO ₂	3 air	4 product	
Stream	1	0.000000	0.000047	0.000000	0.000000
	2	0.000000	0.000047	0.000000	0.000000
	3	0.000333	0.000000	0.000000	0.000000
	4	0.000333	0.000047	0.000000	0.000000
	5	0.000663	0.000000	0.099705	0.000000
	6	0.000663	0.000000	0.099705	0.000000
	7	0.000996	0.000047	0.099705	0.000000
	8	0.000996	0.000047	0.099705	0.000000
	9	0.000000	0.000000	0.000000	0.000000
	10	0.000000	0.000000	0.000000	0.000000

Table 9.10: Results table for Measurement 11

9.2.2 Discussion of results

The model of the mass flow rates through the system offers several important uses. Nevertheless, the results must first be validated.

As a quick preliminary step, the inlet flow rate of each component are compared to the outlet flows to make sure they are the same. The comparison, outlined in **Table 9.11**, shows that the system is balanced.

Flow rates [kg]	Components				
	1 water	2 CO ₂	3 air	4 product	
Stream	In	0.000996	0.000047	0.099705	0.000000
	Out	0.000996	0.000047	0.099705	0.000000

Table 9.11: Inlet and outlet flow for Measurement 11

The validity of the model can further be established by comparing the calculated values to ones measured during the experiments. For this comparison the author used the experimental measurements of air velocity at the outlet, and factoring for temperature and humidity, he compared the measured flow rate with the calculated one. CO₂ was neglected in the outlet stream.

Running the calculations in Matlab reveals that for the measured velocity of 20.62 m/s, measured relative humidity of 17.60%, pipe diameter of 10 cm, measured temperature of 57.06 °C and atmospheric pressure (101.325 kPa) the following results are obtained:

Mass flow rate of dry air: 0.060091 kg/s
Mass flow rate of water: 0.0011588 kg/s
Total mass flow rate at outlet: 0.061250 kg/s

Thanks to these numbers two things can be observed. The first is that the quantity of water leaving the system as calculated from the humidity measurement in the outlet pipe is far higher than the amount of water entering the system. In other words, from the mass balance one should expect a relative humidity of 9.278% in stream 8, which is far lower than the 17.60% recorded by the humidity sensor. This confirms the author's suspicion that the humidity sensor at the outlet is damaged. He had previously observed that the temperature sensor located in the same position as the humidity sensor was giving impossible readings.

The second important conclusion that can be drawn from the numbers is that there is a large leakage in the system. Since 0.099705 kg/s of air entered the system, and only 0.060091 kg/s leaves through stream 8, we observe a 39.7% loss of air. This loss can occur at many places, including connections between the piping, and in the ventilators and filters. High leakage is associated with higher energy costs and also entails a higher number of nanoparticles escaping into the surrounding air and being inhaled by the operator of the equipment.

Initially, the author had intended to expand his model to include the balance of enthalpies in the system. However, after numerous attempts, he came to the agreement with the thesis supervisor to abandon the idea. Owing to the complexity of the expansion of near-critical CO₂ and water from the nozzle, the work required to perform such calculations would overreach the expectations of this thesis. Despite being used as a refrigerant, very little research has gone into the behaviour of a CO₂-water mixture at high pressures, and therefore we were unable to find the data we needed. Most of the literature sources we examined concerned mixtures with a low concentration of CO₂. From a physicochemical perspective, a four or five phase system would need to be considered, as the liquid media evaporate and the cooling due to carbon dioxide expansion may potentially cause the water to momentarily freeze. Nevertheless, a basic enthalpy analysis of the system was conducted during the preliminary design of the system, and we recommend the expansion nozzle as a topic for future research.



Chapter 10

CFD simulation



10.1 Description of the task

In this chapter, the flow velocities of air inside an experimental dryer are examined. The experimental values having already been measured, the author's task is to create an appropriate model of the system using software and to compare the theoretical values to the measured ones, thus qualifying the computer model's validity.

Dimensions of the equipment and the experimental data were provided by the Thesis supervisor.

The first step in being able to understand the process well is to investigate how air flows inside the drying chambers. Hence experiments were designed to measure airflow when no solution is being injected into the chamber, and these models only consider momentum transport to simulate the velocity field.



10.1.1 The equipment

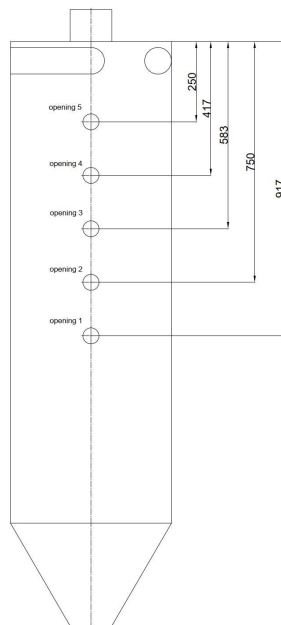
In this particular case, the author investigated two drier geometries. Both are cylindrical in shape, with a conical bottom. Variant A consists of a

more simple geometry. Its main section is the drying chamber, with air entering both vertically downwards from the top and tangentially through the sides. The air is then expected to circulate helically downwards before leaving through a hole at the bottom. The shape of the chamber is that of a vertically arranged cylinder with a conical bottom. There are no walls or partitions inside the chamber itself.

The second variant (Variant B) is an improvement on the first, more simple design. It differs in that it also incorporates a cyclone system to separate the dried particles by their mass into two fractions. Air enters the chamber tangentially at the top through four inlet pipes. It then spirals down to the bottom of the tank where the heavier particles are collected in a vessel, whilst the air and smaller particles are sucked through a pipe back up through the middle of the chamber and exit through an opening at the top.

The tank itself is part of a wider arrangement of equipment, involving blowers, heaters, and filters. The whole system is summarised in the process flow diagram **Appendix A**.

10.1.2 Measurements



(a) : Vertical placement



(b) : Variant B

Figure 10.1: Location of measurement holes for both variants

Measuring the experimental data on the dryers was conducted in collaboration with the Food Research Institute Prague.

A set of openings is included in the design of the dryer along the height of the tank to allow for the insertion of a probe. These were used to take readings of the air velocity at specific points inside the volume. The vertical placements of the holes in the dryer are indicated in **Figure 10.1**.

The measuring device used was a hot wire anemometer. It was inserted into the chamber with incrementally increasing depth. Both axial and radial air velocities were recorded and averaged over 60 seconds.

The collected data was then compared with the simulated models. For Variant A data was used from Measurement 1 and for Variant B data was used from Measurement 4 (see **Appendix B**).

■ 10.2 Numerical model

■ 10.2.1 Chosen approach

In order to simulate the airflow inside the dryer, the author opted to work with the software package ANSYS 2019 R2. The software package allows the user to load a CAD model of the geometry, generate an appropriate mesh, then examine the flow inside the system according to given input parameters.

In the Workbench software he created two projects, one for each variant. A project consists of a network diagram with three nodes connected linearly, corresponding to three specific applications. Each of these represents a necessary step in the modelling of the system.

The first one (“Geometry”) was used to load the dryer’s dimensions into the software, and conduct some necessary set-up operations, prior to creating the mesh. The second step (“Mesh”) is used to choose discrete points within the geometry where the flow rate will be approximated, and the third step (“Fluent”) calculates the flow inside the chamber according to input parameters and the chosen computation model.

Due to an issue in working with the software, the mesh for the Variant B was provided by the author's supervisor. The meshing phase wouldn't recognise the blades at the bottom of the cyclone, which were modelled as zero-thickness walls. Thus, the second model was calculated directly in Fluent, skipping the first two, unsuccessful, steps.

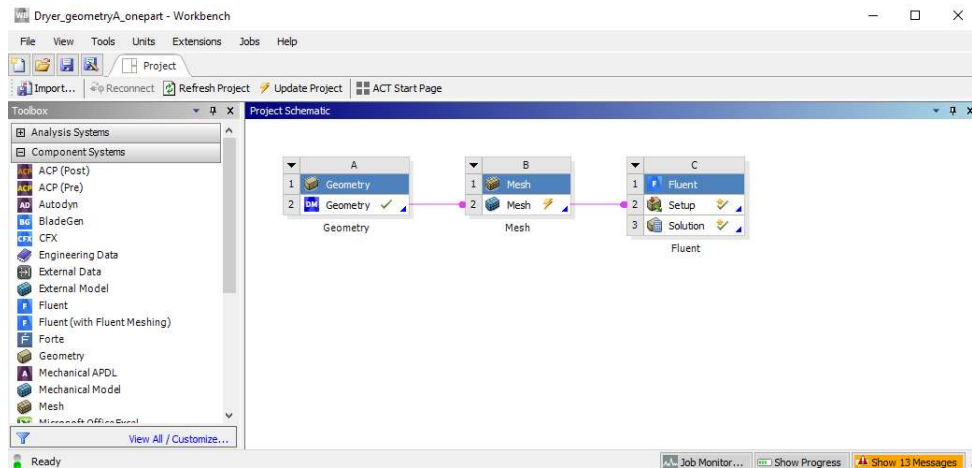


Figure 10.2: Processing tree in Workbench

Prior to opening ANSYS, the author estimated the air velocity at the inlets in both cases. He started with the flow rate, which he obtained from previous work by other researchers and using basic geometrical relations calculated the following values. For Variant A, the velocity through the top inlet was 10.350 m/s, through each side inlet 1.5402 m/s, and for Variant B, the velocity through the side inlets was 3.6708 m/s.

The author then checked Reynold's values through the inlet tubes and found that its value was higher than the critical Reynolds number for flow inside a pipe. Therefore, in the simulations the author chose a model that allowed for turbulence.

To calculate Reynold's number, the following equation was used:

$$Re = \frac{\rho \cdot u \cdot d}{\nu} \quad (10.1)$$

The author used the values for air at atmospheric pressure and a temperature of 40°C. Thus, ρ is 1.1275 kg/m³ and ν is 1.6982 x 10⁻⁵ m²/s [18].

For the Variant A, the Reynold's value of the flow through the top inlet

(diameter 0.129 m, air velocity 10.350 m/s) is 88645.7 and through the sides (diameter 0.083 m, air velocity 1.5402) is 8487.6.

For the Variant B, the Reynold's value of the flow through the side inlets (diameter 0.083 m, air velocity 3.6708 m/s) is 20228.6.

An approximate value for Reynold's number in the drying chamber (using tangential velocity 15.14 m/s, diameter 500 mm - Measurement 4, opening 5, probe inserting depth 2 cm) is 502601.28.

From these results it is clear in both cases that Reynold's number is much higher than the critical point for fluid flow inside a pipe ($Re = 2300$) and thus the author used a numerical calculation model that allows for turbulence.

■ 10.2.2 Generating the shape

The first step in numerically analysing the flow inside a system is to work out the appropriate geometry, the space inside which the air will be moving. In this case this geometry equated to the space inside the dryer tank. All the data that the author used was obtained in connection with the author's thesis.

In the case of Variant A, the author used the dimensions of the dryer to model the inside space of the chamber in Fusion 360, creating the whole geometry from one part. This offers the advantage of simplicity during the meshing stage, though can lead to less precise analysis of the flow in more complex areas of the geometry. The created data was exported as an .stp file. before being loaded into ANSYS.

From the mesh provided for Variant B, it can be seen (**Figure 10.7**) that the object was modelled as separate bodies joined into one part. This allows for a simpler mesh in less complex sections of the dryer but allows more complex volumes such as the bottom of the cyclone to be meshed more finely.

As previously mentioned, the blades are modelled as zero-thickness walls.

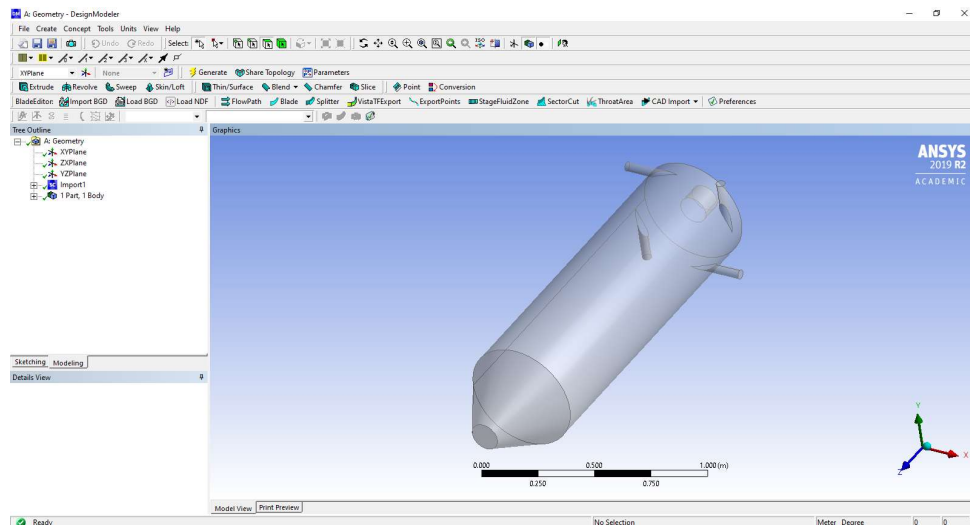


Figure 10.3: Geometry A

10.2.3 Meshing

The mesh serves to designate discrete points inside the defined geometrical space at which the airflow will be calculated. The finer the mesh, the more accurately the system can be modelled, however it will also take longer to compute. A correctly prepared mesh will allow the flow to be analysed in appropriate detail, whilst keeping its complexity to a minimum.

Variant A

Since the first geometry is composed of just one part, the meshing of it was fairly simple. The physical preferences were set to CFD, Fluent, and element size to 20 mm, and left the other settings at their Default.

The most important step in creating the mesh is to calculate an appropriate value for the wall function. To facilitate the calculation, the author used the following Matlab code, provided by doc. Ing. Karel Petera, Ph.D., which returns the distance at which y^+ is equal to 1. This value should be taken as the thickness of the first inflation layer in the meshing model.

```
rho = 1.225;          % density of air
```

```

mu = 1.7894e-05 ; % dynamic viscosity, Pa s
nu = mu/rho      % kinematic viscosity
u = 1.5401;      % velocity, m/s
Lchar = 0.083;   % characteristic length, m

Re = rho*u*Lchar/mu
% Re = u*Lchar/nu

Cf = 0.079*Re^-0.25 % internal flows
% Cf = 0.058*Re^-0.2 % external flows
tauw = 0.5*Cf*rho*u^2
utau = sqrt(tauw/rho)

yp = 1 % to resolve the viscous sublayer, the first grid cell
      % needs to be at about y+ = 1

y1 = yp*nu/utau % width of the first layer, m

```

Running the script with the parameters for the two inlets returns the values of $y1 = 0.00014842$ m in the side inlets (from the example above), and $y1 = 0.000029611$ m for the top inlet. The author chose an intermediate value of 0.0000345 m which is nevertheless precise enough for the top inlet.

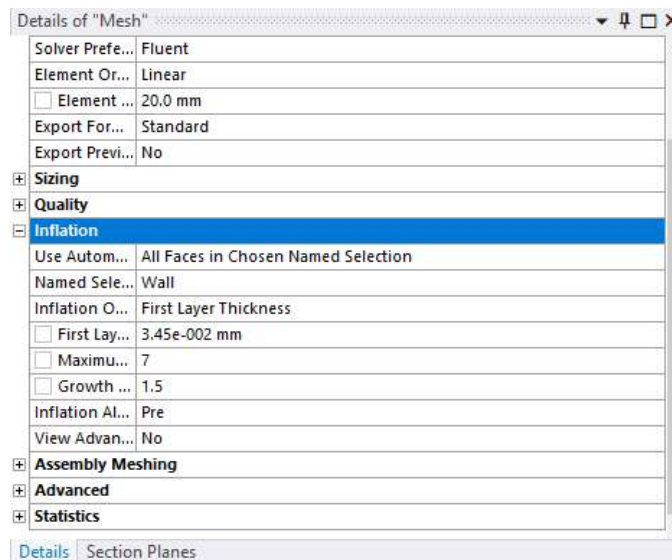


Figure 10.4: Inflation settings for Geometry A

The resulting mesh is shown in the next two figures (figures 10.5, 10.6)

The mesh contains **377569 elements** and has an **average orthogonality**

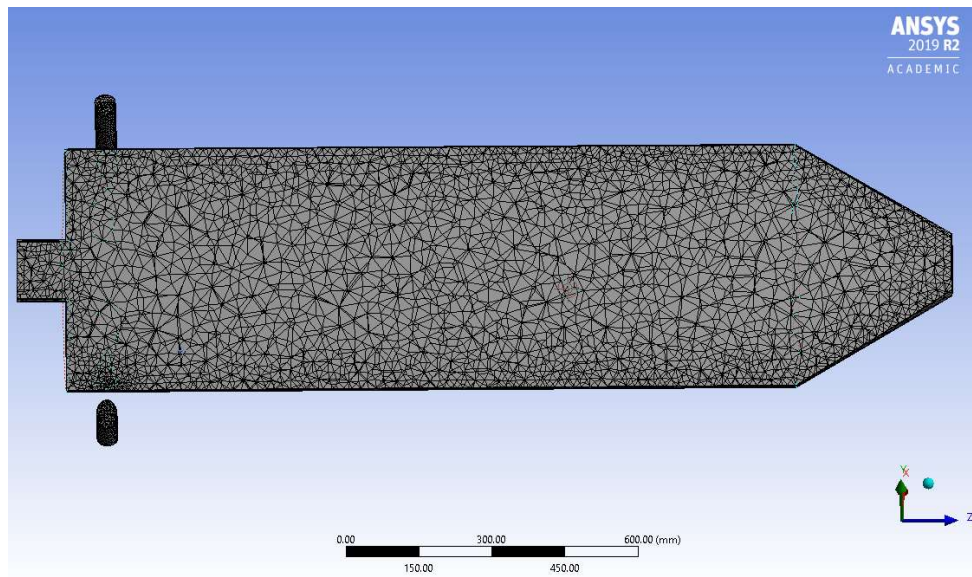


Figure 10.5: Cut of the mesh for geometry A

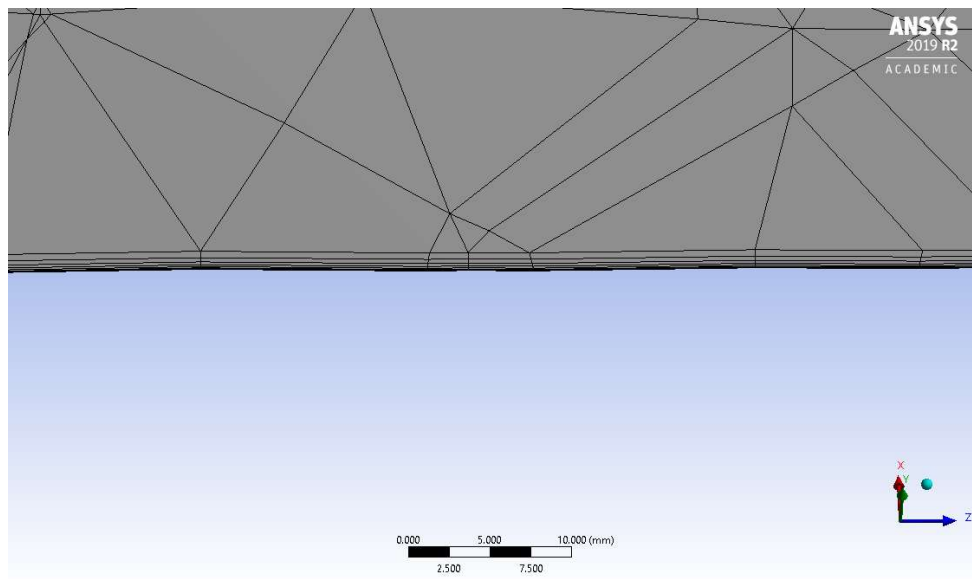


Figure 10.6: Close-up of the inflation layer

of **0.79645**. This slightly lower orthogonal quality is a result of the model being comprised of just one part.

■ Variant B

Since the data for variant B was provided ready-meshed, the author did not choose the parameters. It contains **116285 elements**.

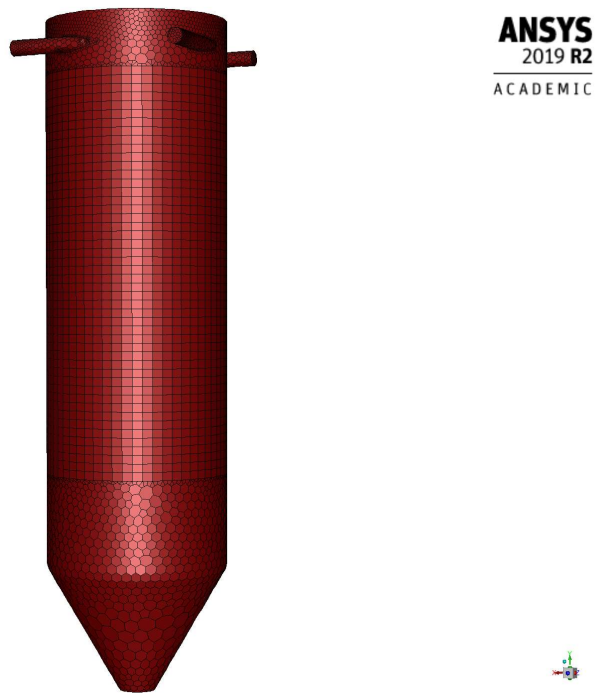


Figure 10.7: Mesh of geometry B

■ 10.2.4 Fluent

The meshes were then loaded into Fluent where after setting the initial parameters, the simulations were conducted. The author specified that the dryers operate under a normal gravitational field of 9.81 m/s^2 , and that the fluid medium is air at 20°C . Having calculated that the Reynolds number in some parts of the dryer was higher than the critical value, the author opted for a viscous calculation model that accounts for turbulence. No heat transfer is considered.

Variant A

The first step in the simulation was to define the boundary conditions. The ends of the side and top entrance pipes were designated as momentum inlets, with air entering consistently across the pipe's diameter at a perpendicular angle. At the sides, the velocity was set to the calculated value of 1.5402 m/s. The supersonic gauge pressure was set to zero, and the turbulent settings left at their default values (Turbulent intensity 5%, Turbulent viscosity ratio 10). For the top inlet, a velocity of 10.35 m/s was assigned with the other values the same as for the sides.

The outlet at the bottom was set to be a pressure outlet. Its properties are shown in figure 10.8.

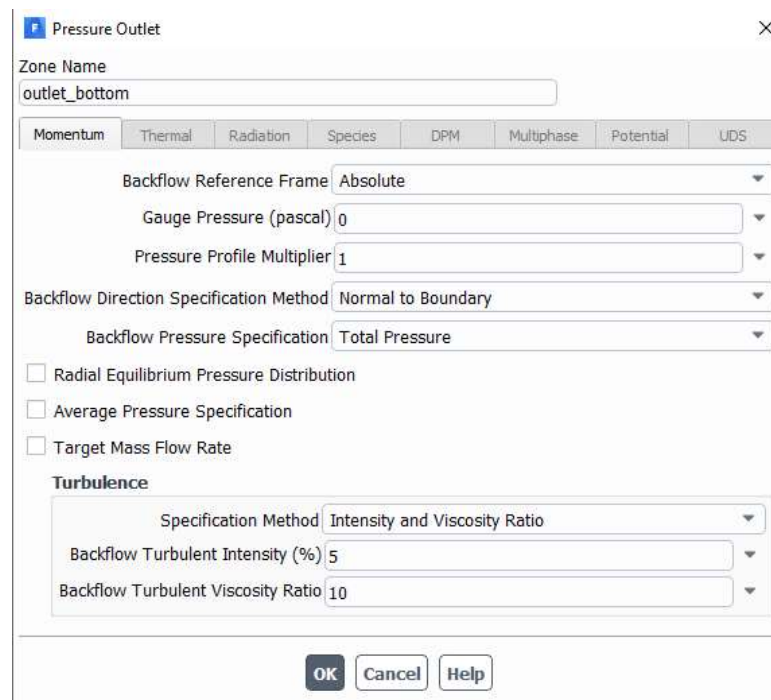


Figure 10.8: Variant A - outer boundary conditions

The walls of the vessel were designated as a no slip stationary wall with roughness height of 0 m and a roughness factor of 0.5.

The solution methods are shown in **Figure 10.9**.

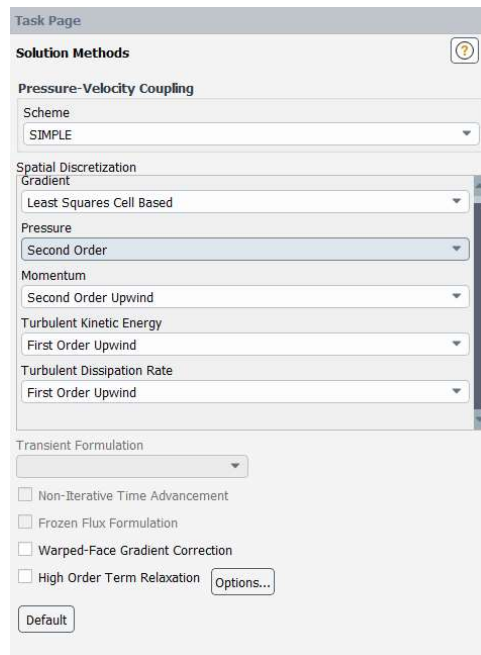


Figure 10.9: Variant A - solution methods

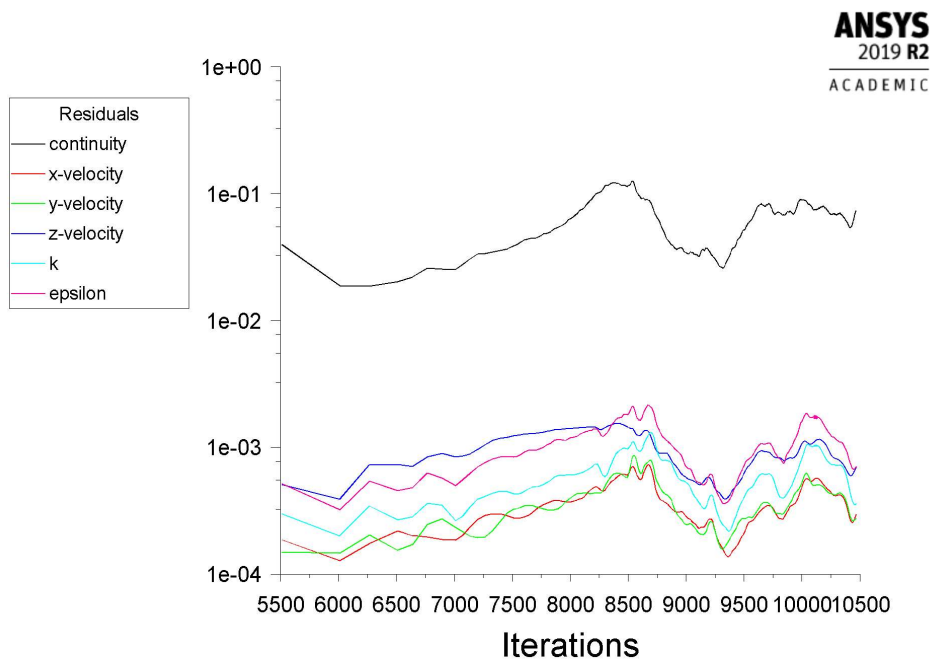


Figure 10.10: Residuals during computation of Variant A - k-epsilon model

The solver control under-relaxation factors are summarised as follows:

- Pressure: 0.3
- Density: 1
- Body Forces: 1
- Momentum: 0.7
- Turbulent Kinetic Energy: 0.8
- Turbulent Dissipation Rate: 0.8
- Turbulent Viscosity: 1

The first geometry was simulated for 10467 iterations using the simulation model “k-epsilon, realizable”. The residue graph (shown in **Figure 10.10**) indicates that the results are not particularly accurate, neither did the residues settle at a steady value, despite being iterated so many times.

The author therefore opted to simulate the system again using a k-omega model for reference, however the residuals were similar in order, and the results showed similar flow paths predominantly in the axial direction. The author recorded the results from only the original k-epsilon model.

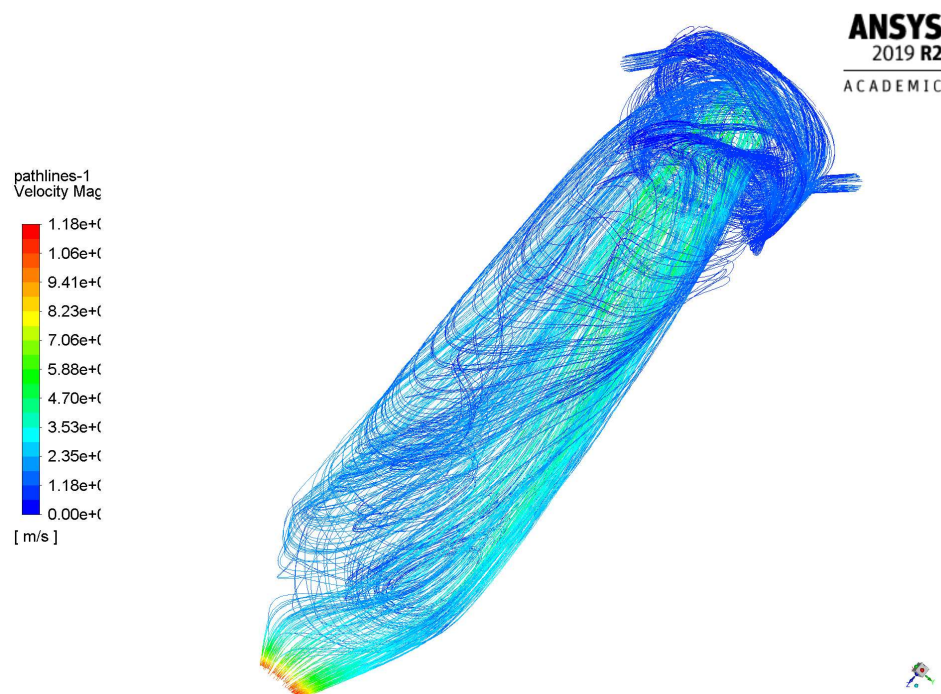


Figure 10.11: Velocity field - particle paths in variant A, k-omega simulation

■ Variant B

In the case of Variant B, the author opted directly for the k-omega model.

Regarding the boundary conditions, each of the side pipes was indicated as an entrance with velocity of 3.6708 m/s, the other conditions were left the same as in Variant A.

The outlet at the top was set to the same as the outlet in Variant A, and the walls also had the same settings.

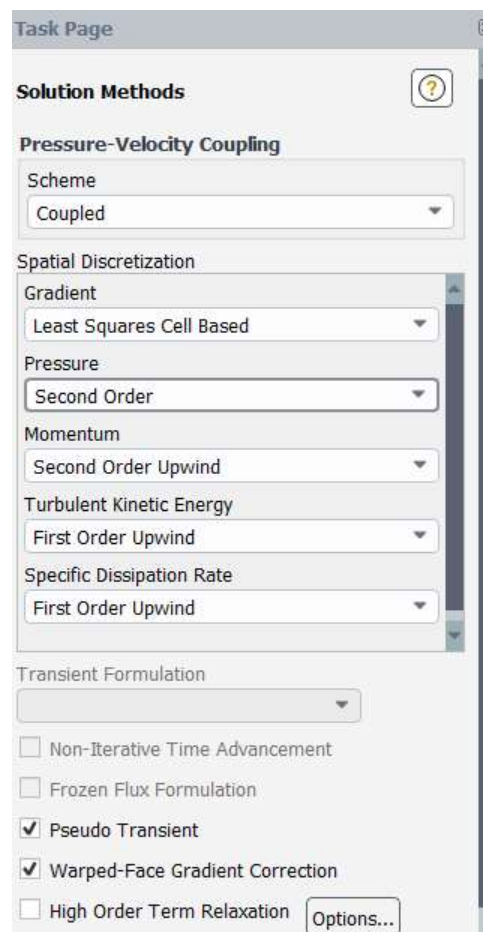


Figure 10.12: Variant B - solution methods

During the experiments, a metal vessel was attached to the opening at the bottom of the dryer to catch hypothetical dry matter. Since the vessel wasn't included in the meshed geometry, the opening in the bottom of the dryer was

modelled as a wall with no slip, a roughness height of 0 m and a roughness constant of 0.5.

The solution methods are shown in **Figure 10.12**.

And the control values are as follows:

- Pressure: 0.5
- Momentum: 0.5
- Density: 1
- Body Forces: 1
- Momentum: 0.7
- Turbulent Kinetic Energy: 0.75
- Turbulent Dissipation Rate: 0.75
- Turbulent Viscosity: 1

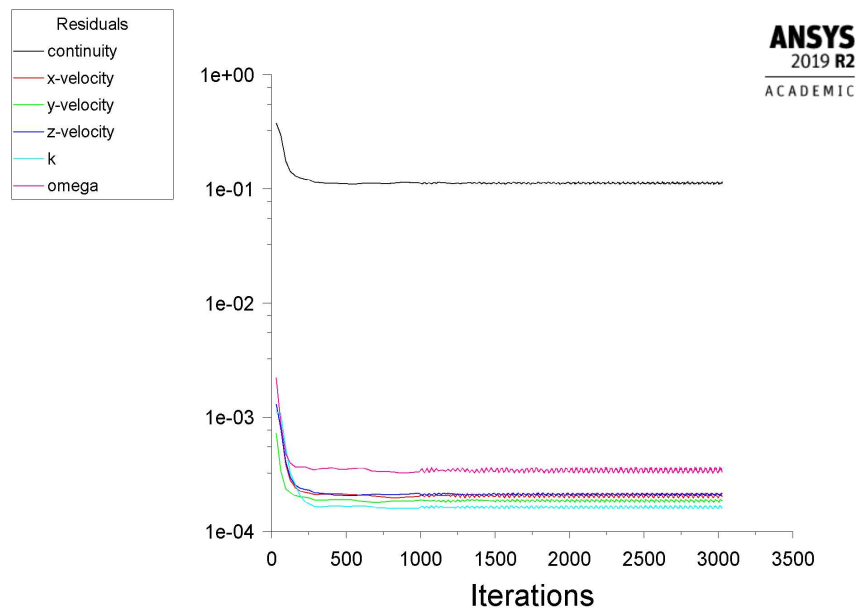


Figure 10.13: Residuals during computation of Variant B - k-omega model

A steadier behaviour was obtained, though the residuals were not significantly smaller. The simulation was iterated 3028 times.

10.3 Results and discussion

Following the simulation in Fluent, the author examined the results. He chose to represent the data initially in graphical form, displaying the velocity fields at key points as well as the particle paths, which clearly show how the different airstreams interact. He also plotted graphs showing the tangential and axial velocities at the level of the openings where the air velocities were measured on the experimental dryer. Overlaying the modelled and measured results gives the author a good indication of the accuracy of the models.

In order to extract the data from the numerical model, the author created raked lines within fluent at the heights of the openings used for measuring real data. These rakes were aligned along the horizontal axes from the centre to the edge, with 26 evenly spaced points.

The tangential and axial air velocity in the appropriate direction at each point was then exported to a text file, and the data then copied into a Matlab script to be plotted against the measured values. All the graphs and plots are included in **section 10.4** at the end of the chapter.

10.3.1 Variant A

The concept behind the design of Variant A is that the air circulates steadily downwards in a vortex, keeping the air in contact with the substance for drying for as long as possible. The circular motion is provided by the tangential inlet pipes, which are supposed to accelerate the air column entering through the top into the desired cyclonic motion. This can be clearly seen when the measured data is plotted, as the tangential velocity (circular motion around the dryer) is much higher than the axial velocity (motion downwards). It is also obvious from the graphs, that the model has this in reverse, with the air circulating predominantly in the axial direction. This phenomenon is confirmed by the representation of the flow paths (**Figures 10.18 and 10.19**). Thus, there's very little correlation between the modelled system and the measured values of real flow.

As can be seen in the vertical cuts, most of the inlet air from the top proceeds straight down and out the bottom of the chamber. The consequences of this movement mean that once a real liquid is sprayed into the dryer, mixing between the liquid and the drying air, as well as the residence time inside the

dryer are both minimal, making the drying process particularly ineffective.

On reviewing the inlet velocities, it seems to the author that there is quite possibly an error in the received values for air flow rates. Given that the air entering through the sides is supposed to significantly affect the momentum of the air column from the top, it seems illogical that the side velocity is nearly seven times smaller. Perhaps the problem then isn't so much with the model, but with the values used.

■ 10.3.2 Variant B

Our model for the second variant is partially successful. **Figure 10.35** shows an elegant cyclonic path down to the bottom of the drying chamber and then back up through the central pipe.

Looking at the comparisons between the plots of measured versus simulated data the author can see that there's quite a strong correlation in the axial direction. The exception is towards the edge of the chamber (x at around -0.23 m), where the velocity in reality is actually much higher. This raises questions about the correctness of the wall function.

Unfortunately, the data doesn't correspond very well for the tangential direction. The measured velocities are significantly higher than the simulated one, though both show a steady decrease towards the centre (in the simulation, the velocity peaks again at the centre inside the central pipe). Perhaps this is once again an issue of having inlet flow rate values that are too low.

■ 10.3.3 Considerations

Within the scope of his Diploma thesis, the author has been able to create two models of the airflow inside the dryers.

This work was good opportunity for the author to become familiar with numerical modelling of fluid flows, and particularly with the ANSYS software. Nevertheless, both models are far from satisfactory and without further modification cannot be used for further work on the dryer.

10.4 Figures and graphics

10.4.1 Representing flow in geometry A

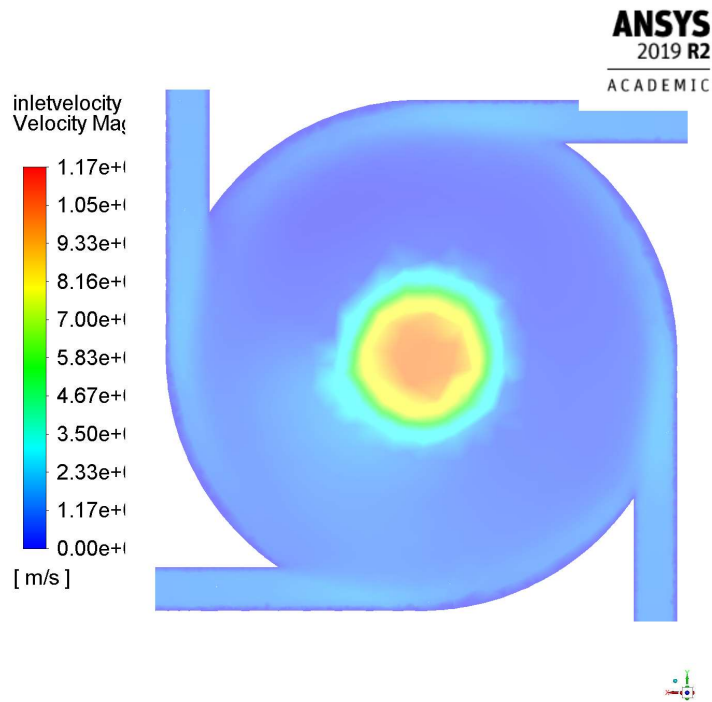


Figure 10.14: Geometry A - Velocity field- contour at the level of the side inlets

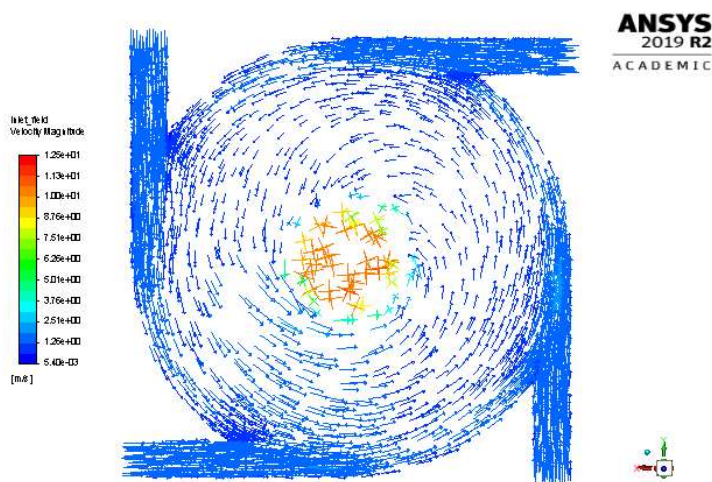


Figure 10.15: Geometry A - Velocity field - cut at the level of the side inlet

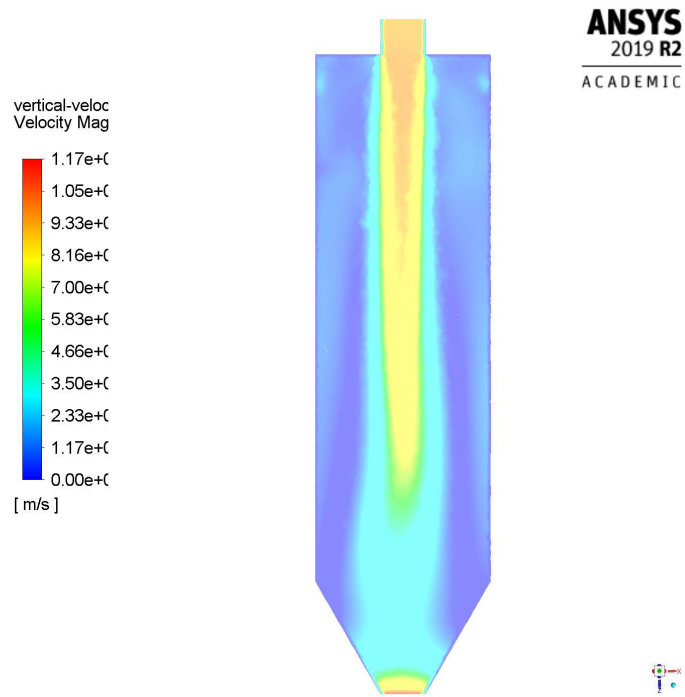


Figure 10.16: Geometry A - Velocity field - x-z plane

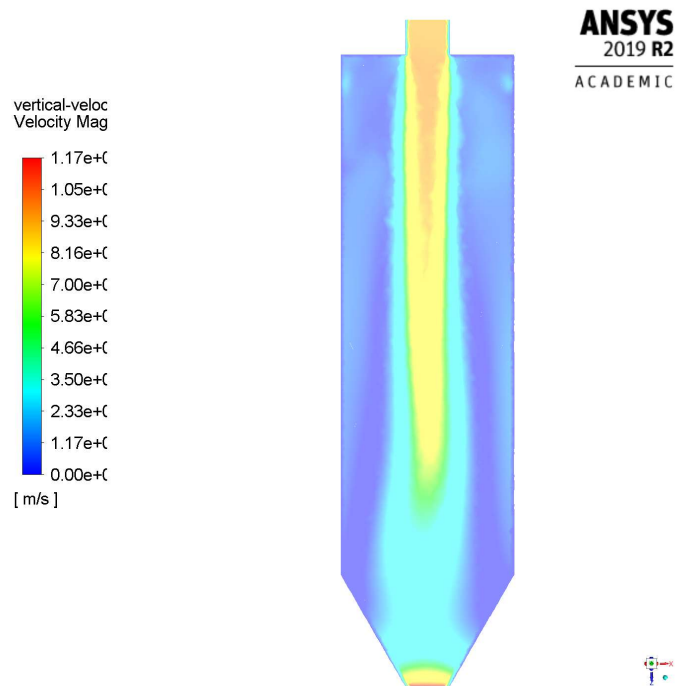


Figure 10.17: Geometry A - Velocity field - y-z plane

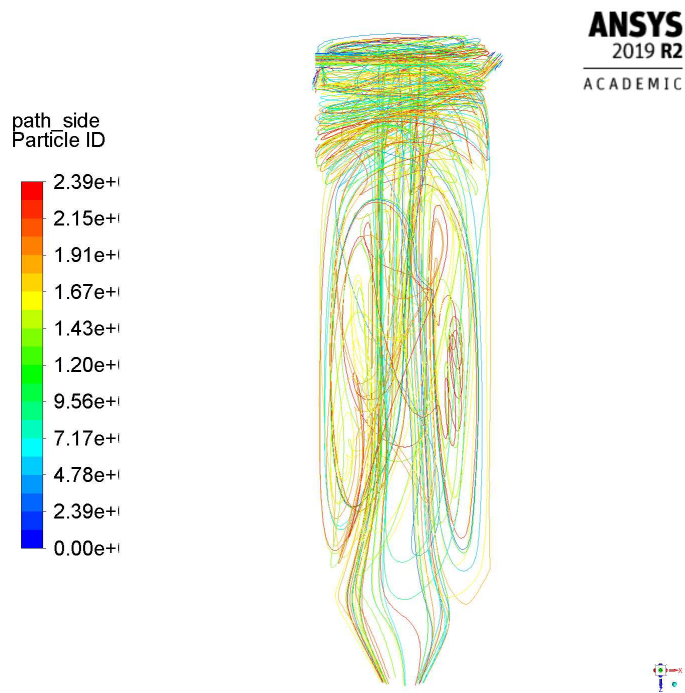


Figure 10.18: Geometry A - Velocity field - path of particles entering from the sides

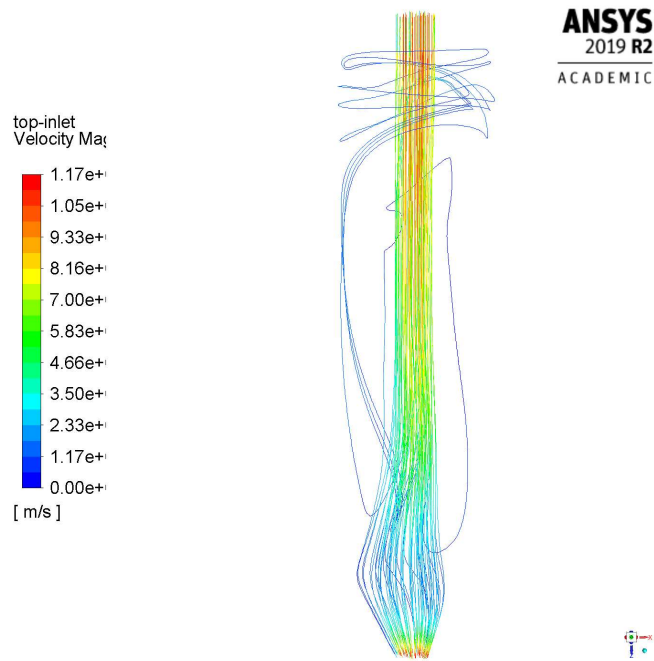


Figure 10.19: Geometry A - Velocity field - path of particles entering from the top

10.4.2 Comparison of results for geometry A

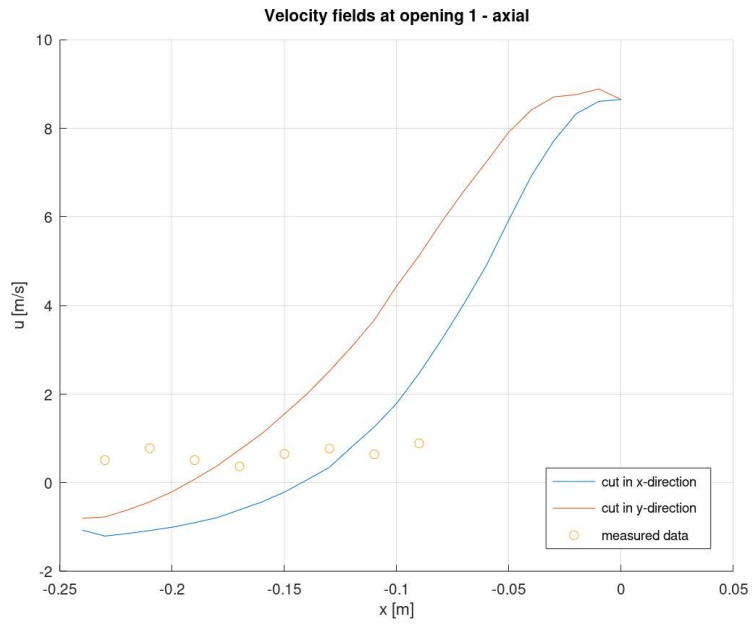


Figure 10.20: Geometry A - opening 1 – axial

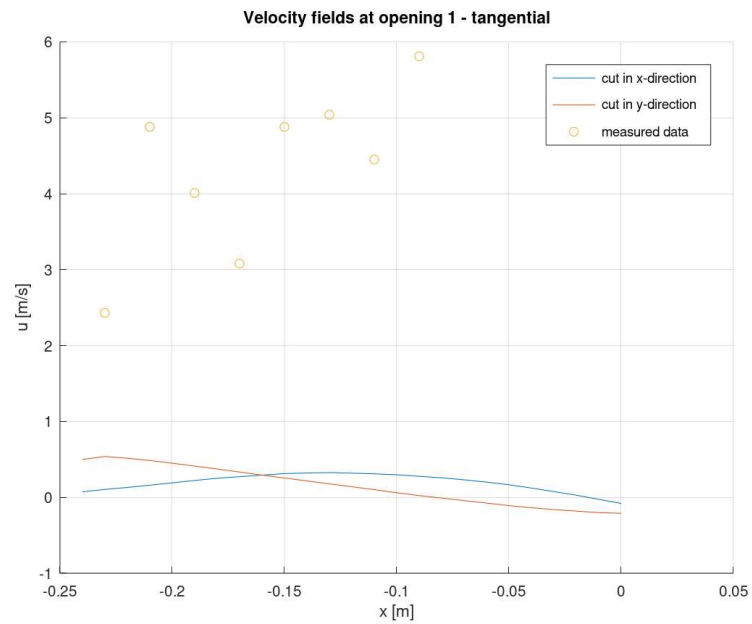


Figure 10.21: Geometry A - opening 1 – tangential

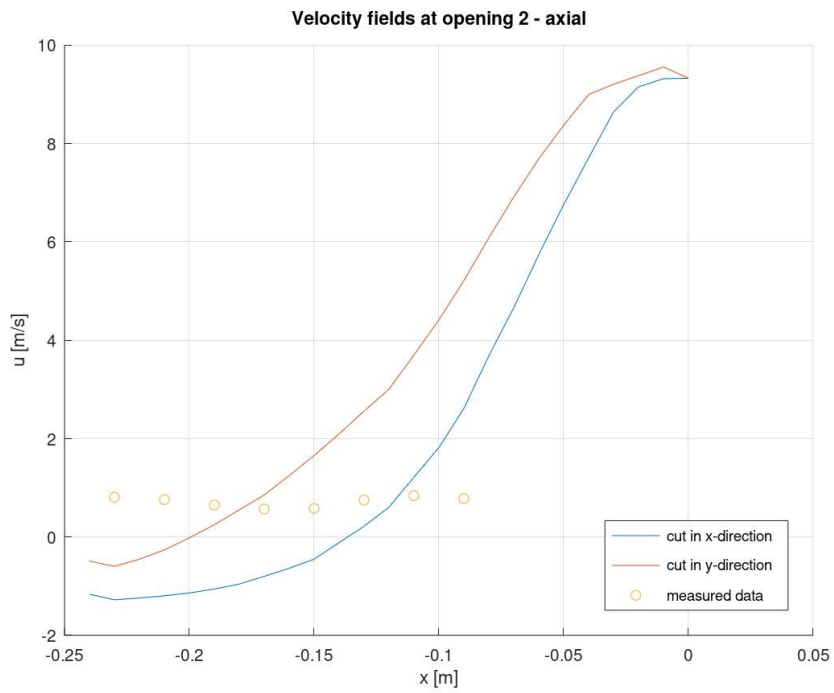


Figure 10.22: Geometry A - opening 2 – axial

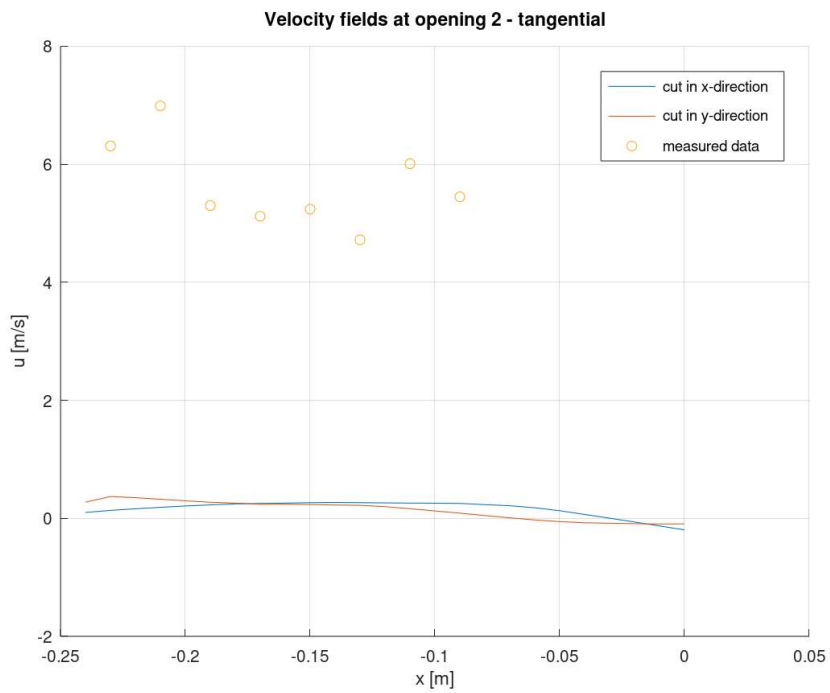


Figure 10.23: Geometry A - opening 2 – tangential

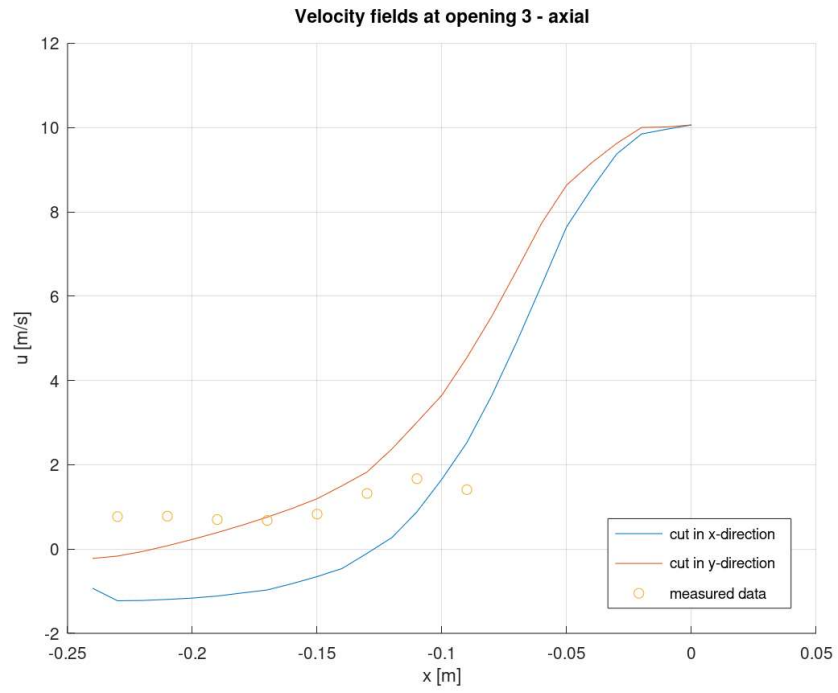


Figure 10.24: Geometry A - opening 3 – axial

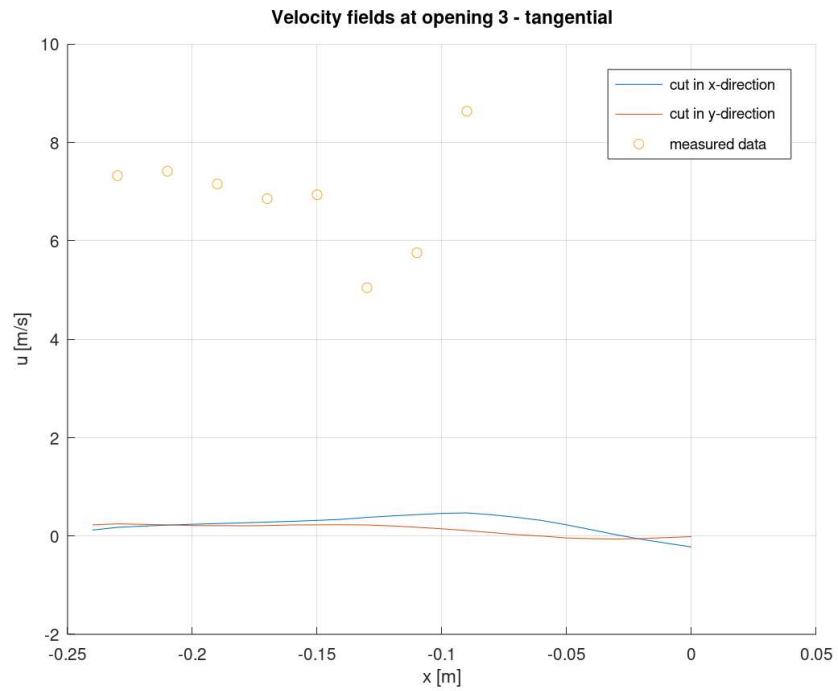


Figure 10.25: Geometry A - opening 3 – tangential

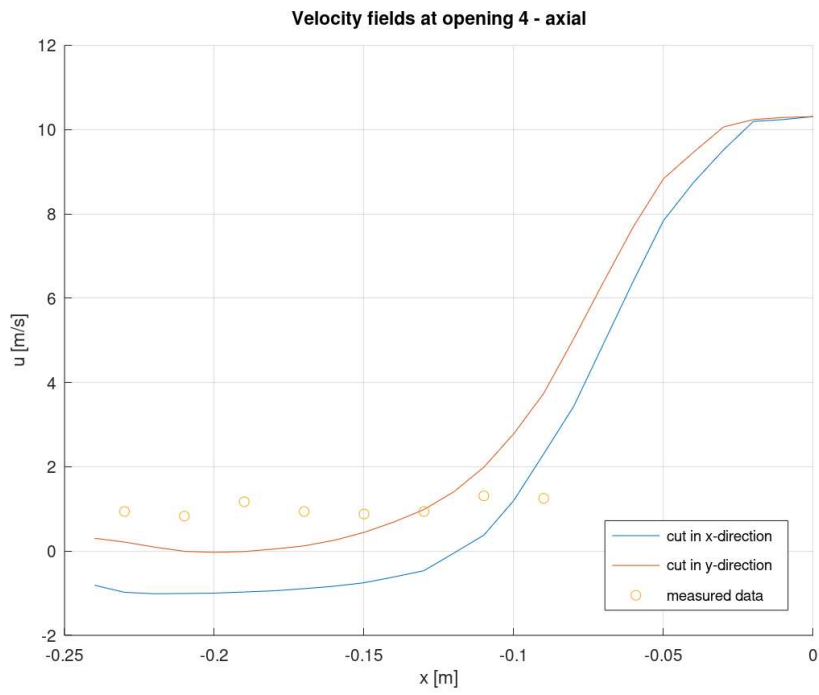


Figure 10.26: Geometry A - opening 4 – axial

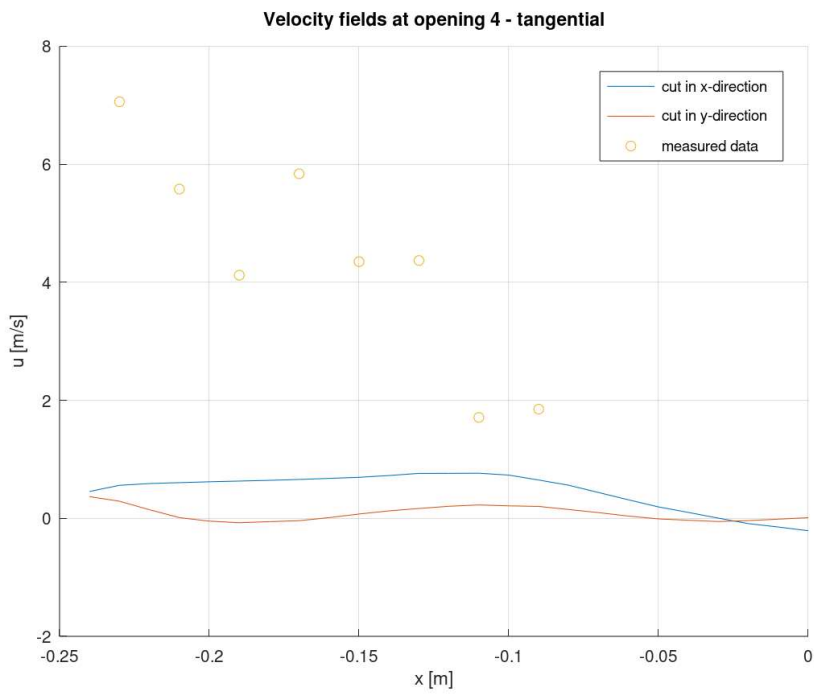


Figure 10.27: Geometry A - opening 4 – tangential

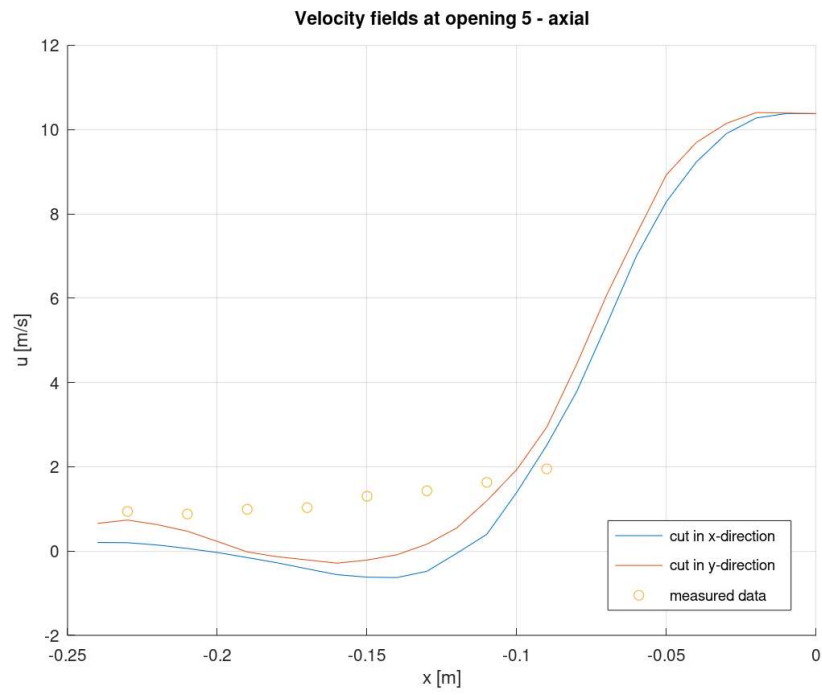


Figure 10.28: Geometry A - opening 5 – axial

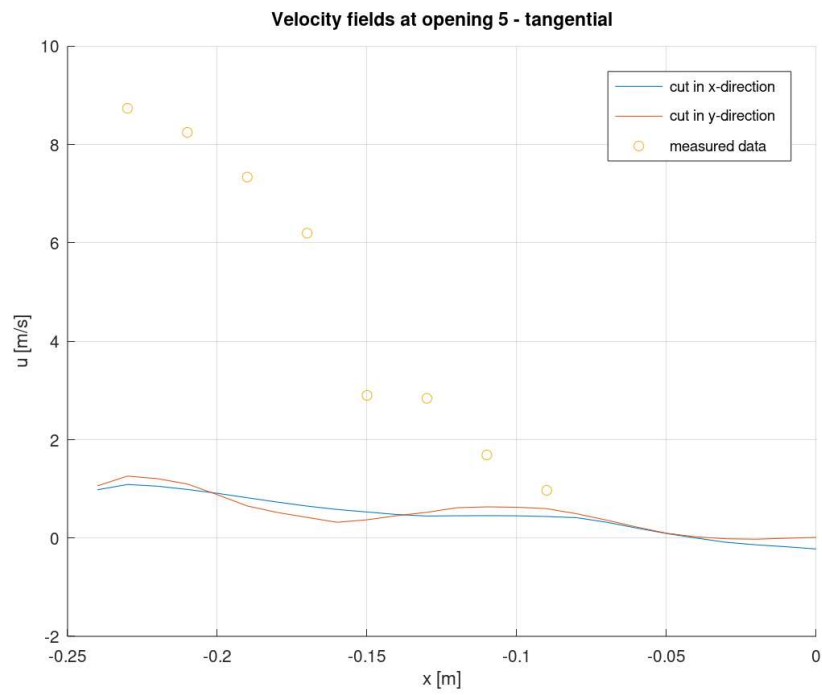


Figure 10.29: Geometry A - opening 5 – tangential

10.4.3 Representing flow in geometry B

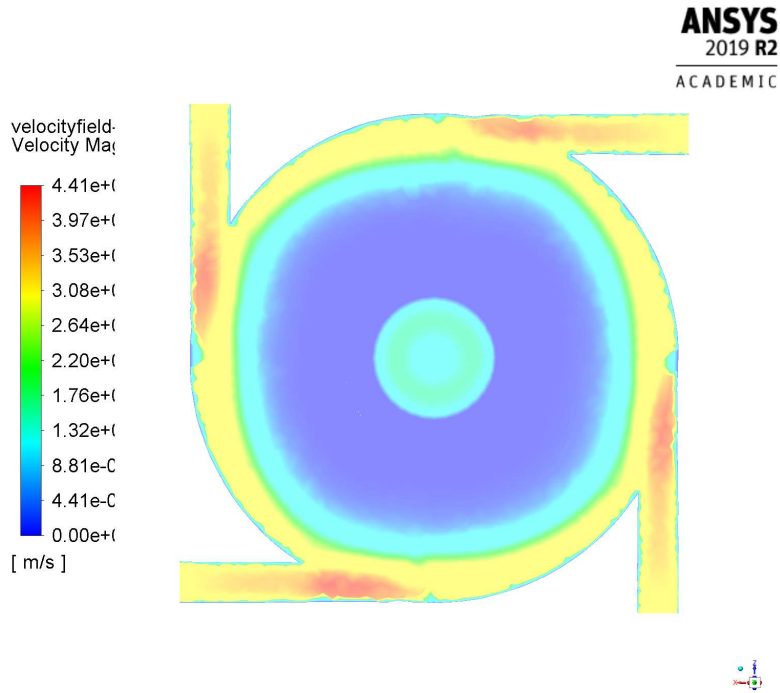


Figure 10.30: Geometry B - Velocity field- contour at the level of the side inlets

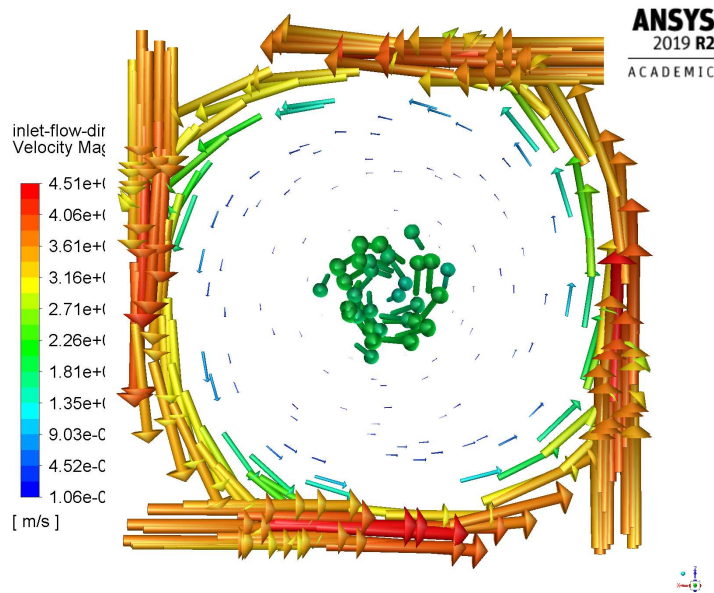


Figure 10.31: Geometry B - Velocity field – cut at the level of the inlets

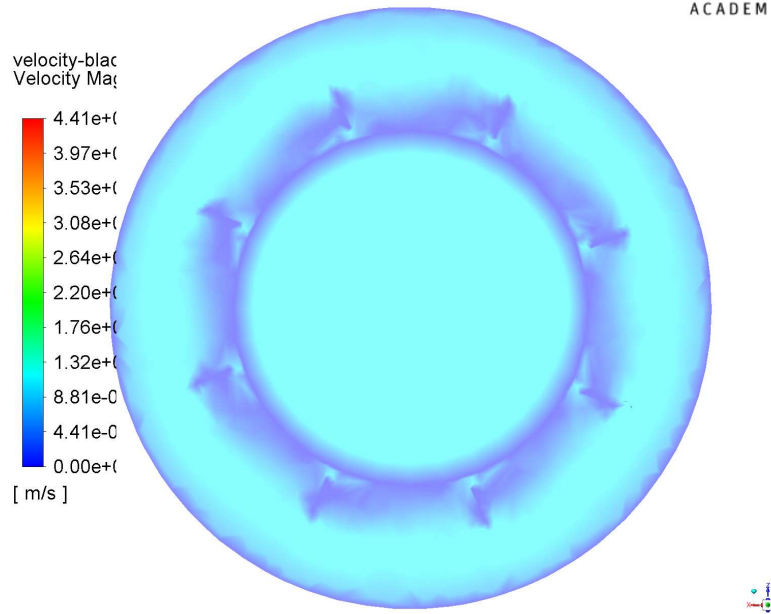


Figure 10.32: Geometry B - Velocity field – contour at the level of the blades

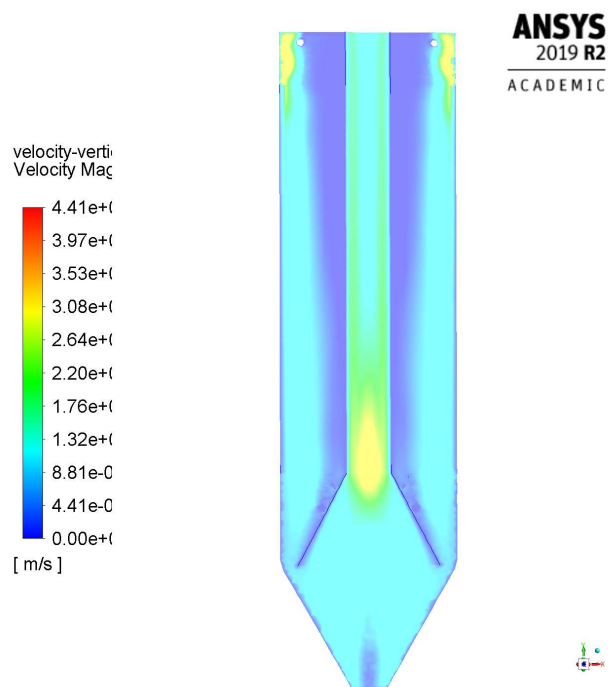


Figure 10.33: Geometry B - Velocity field - x-y plane

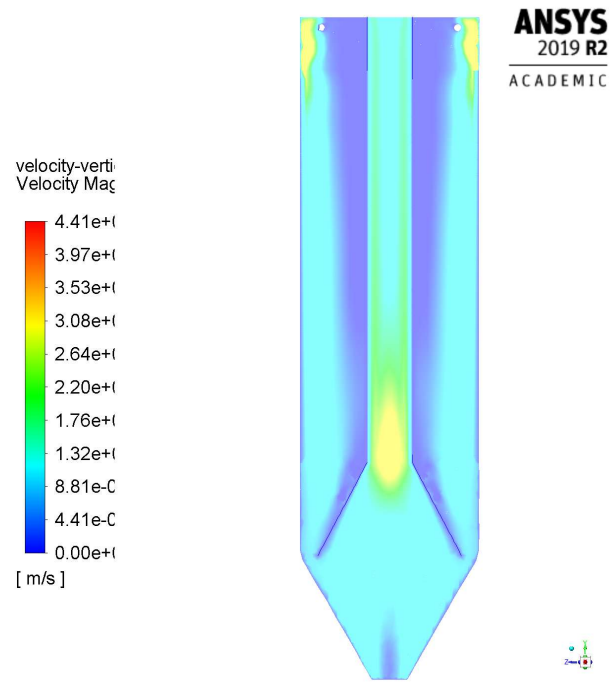


Figure 10.34: Geometry B - Velocity field - z-y plane

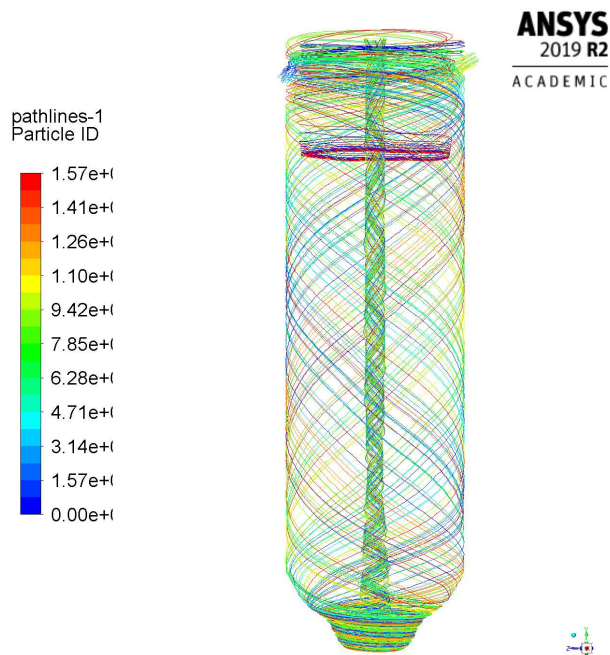


Figure 10.35: Geometry B - Velocity field – particle path

10.4.4 Comparison of results for geometry B

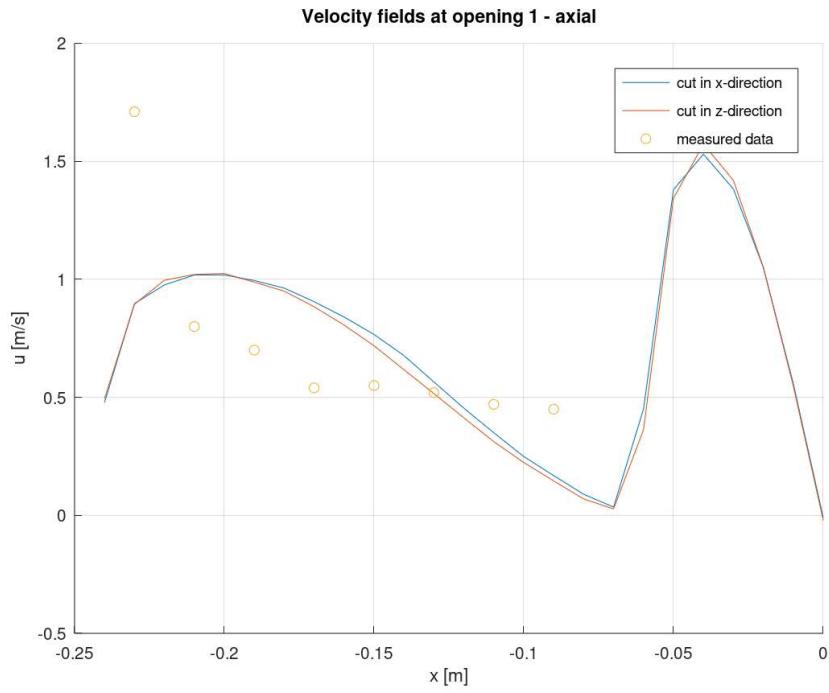


Figure 10.36: Geometry B - opening 1 – axial

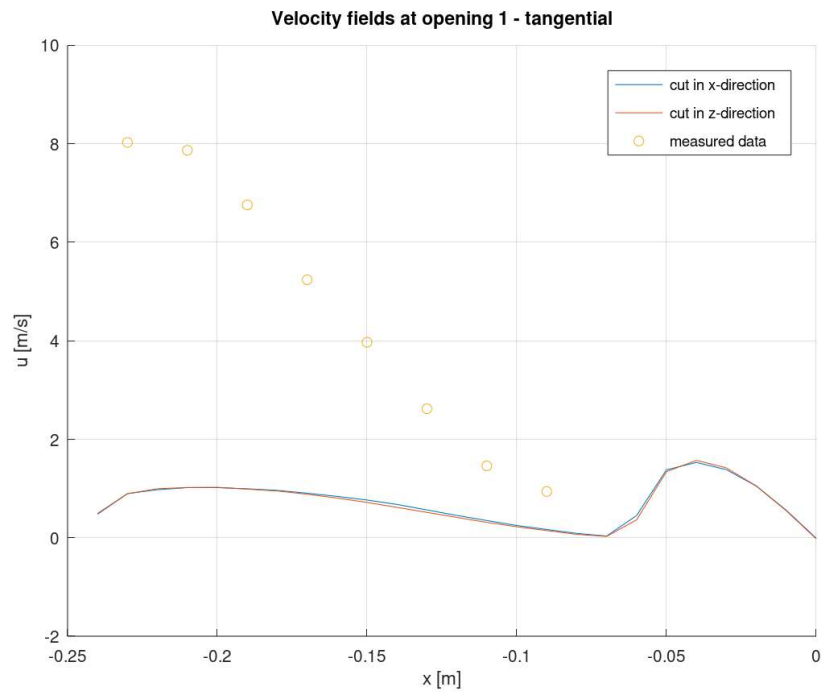


Figure 10.37: Geometry B - opening 1 – tangential

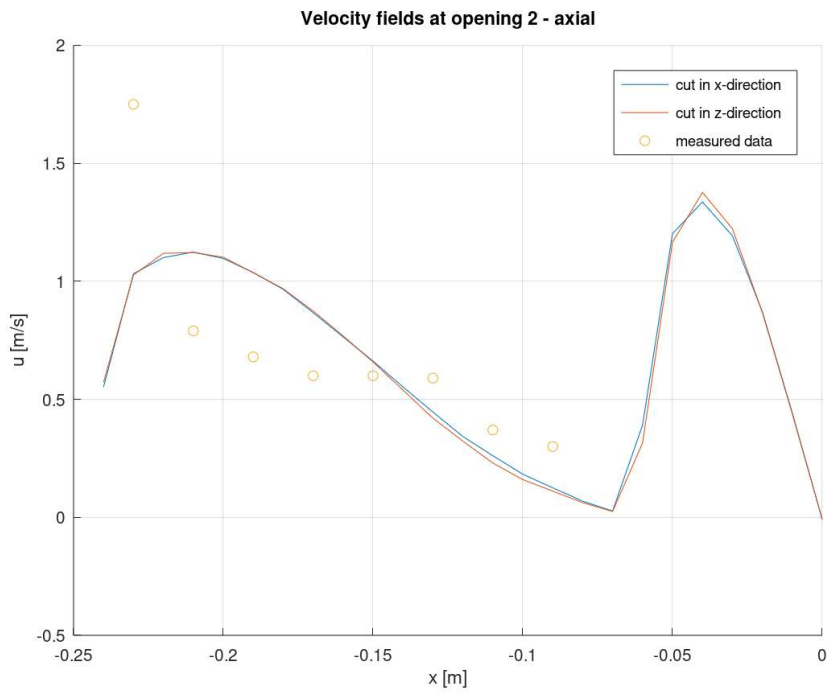


Figure 10.38: Geometry B - opening 2 – axial

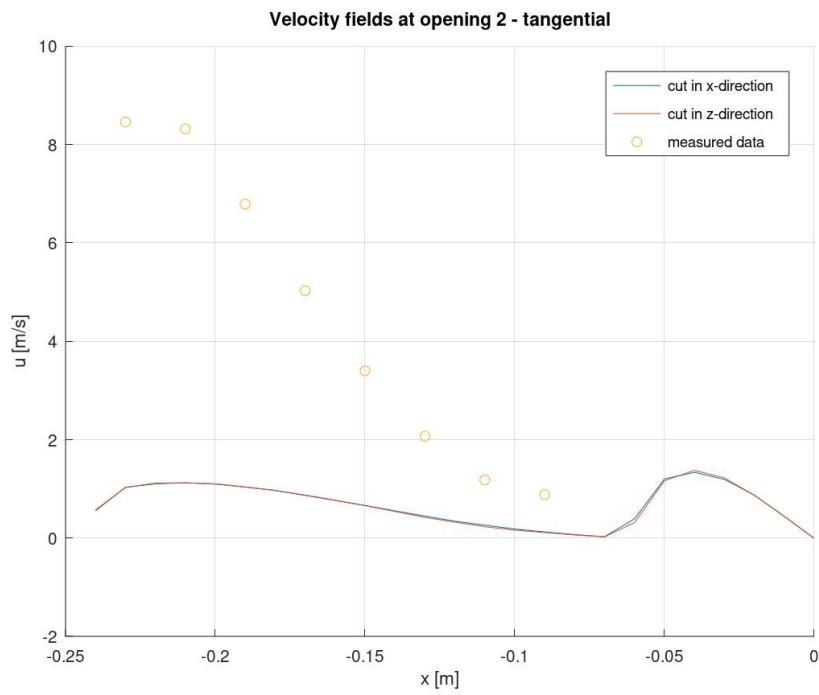


Figure 10.39: Geometry B - opening 2 – tangential

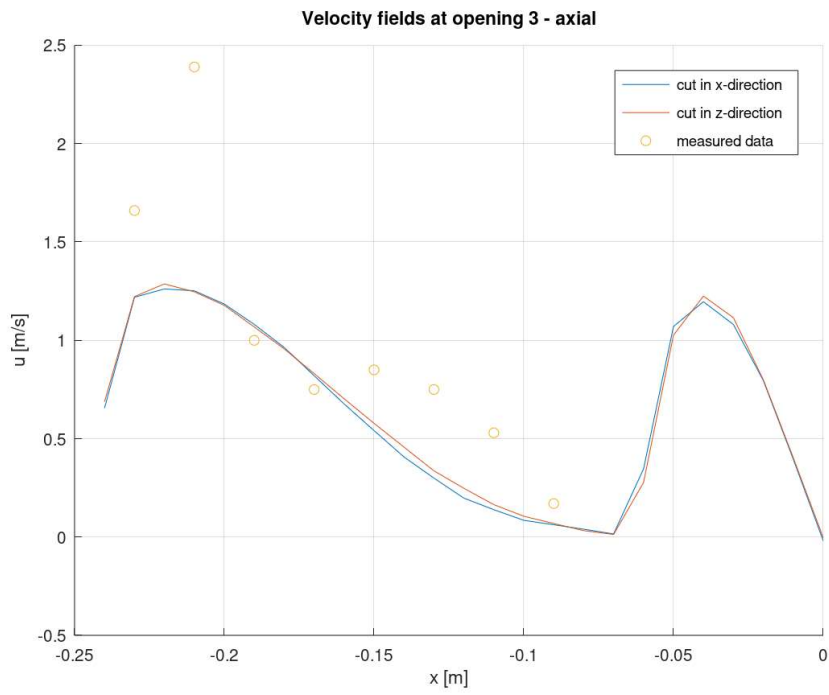


Figure 10.40: Geometry B - opening 3 – axial

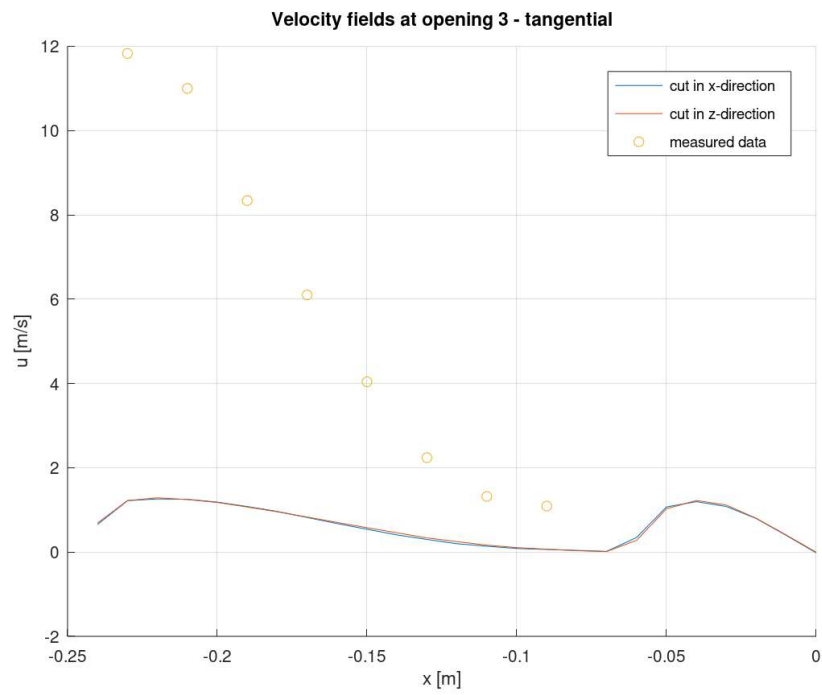


Figure 10.41: Geometry B - opening 3 – tangential

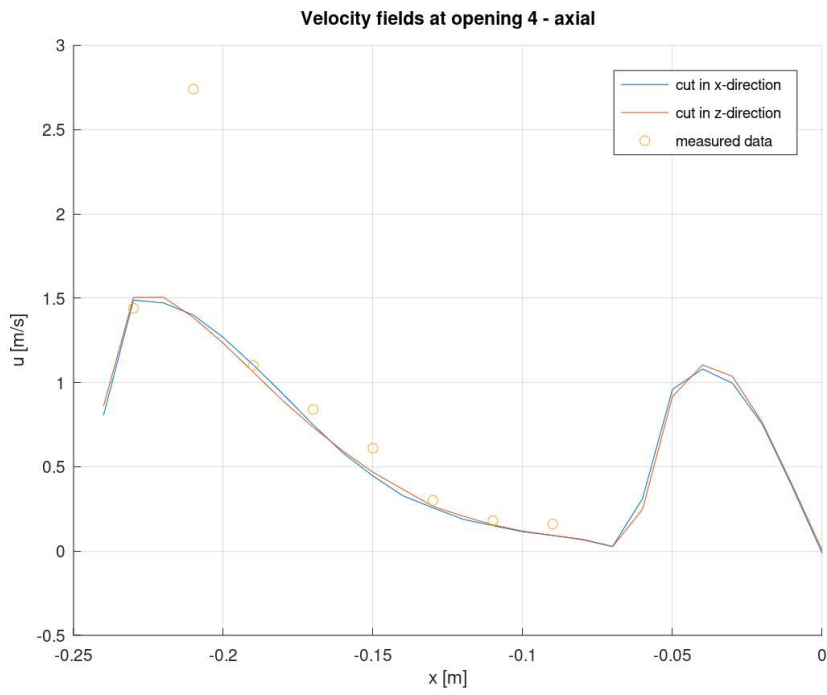


Figure 10.42: Geometry B - opening 4 – axial

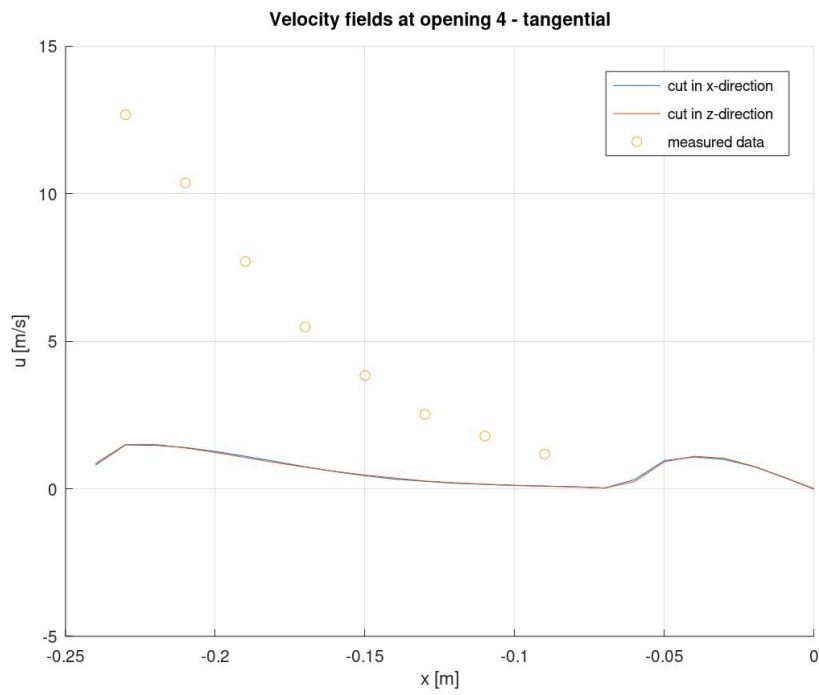


Figure 10.43: Geometry B - opening 4 – tangential

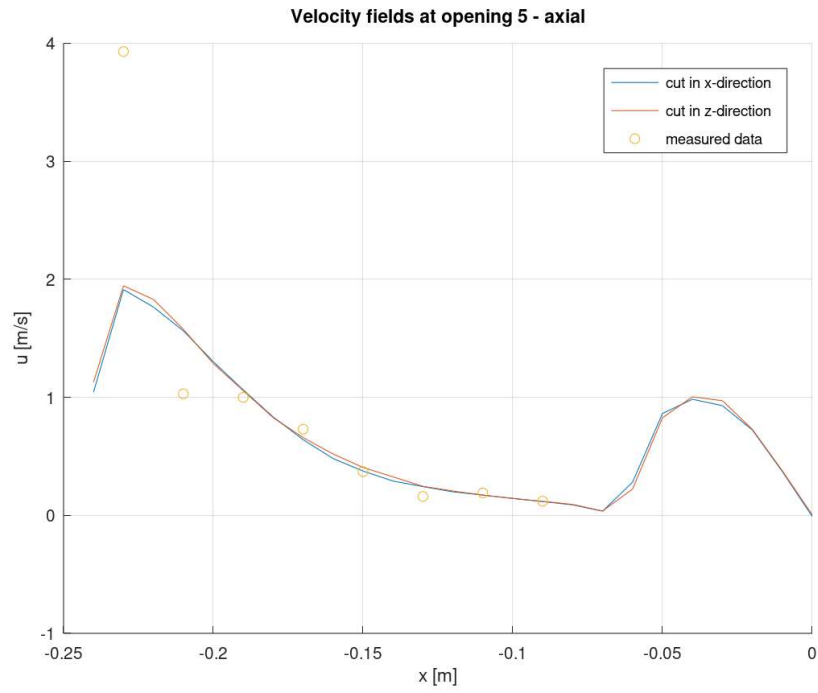


Figure 10.44: Geometry B - opening 5 – axial

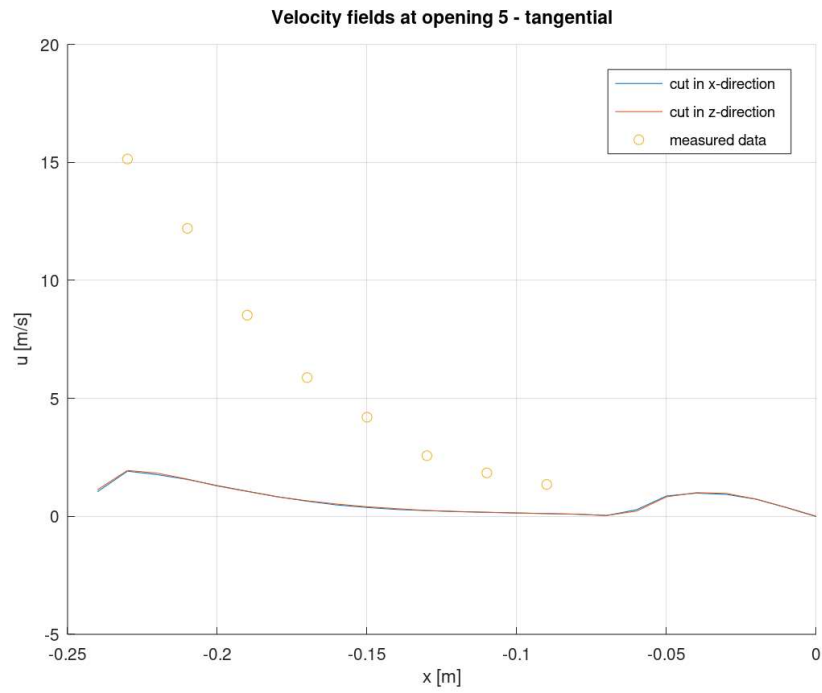


Figure 10.45: Geometry B - opening 5 – tangential

10.5 Further work

After considering the unsatisfactory results obtained thus far, the author decided to continue his work by modifying the inlet velocities in Geometry A. By trial and error it was hoped that inlet values can be found which better replicate the measured behaviour. This may confirm the theory that the primary issue is with the measured values of flow rate, and not directly with the models.

10.5.1 Explanation

To test the author's theory that the lack of correlation between the model and real values in Variant A is caused by incorrect input parameters, the author ran three more simulations in Fluent.

In each simulation the author varied the ratio of inlet air flowing into the chamber through the top and sides, but keeping the total air flow rate constant. The author used the exact same parameters and mesh as in the original simulation (with airflow ratio of Top: 81% - Side 19%), varying only the inlet air velocities, and changing the simulation model to k-omega.

An overview is summarised in **Table 10.1**.

#	Ratio [%]		Flow rate [m ³ /h]			Velocity [m/s]	
	Top	Side	Top	Side	Total	Top	Side
1	81	19	487	120	607	10.35	1.34
2	50	50	303.5	303.5	607.0	6.45	3.39
3	25	75	151.75	455.25	607.0	3.22	5.08
4	5	95	30.35	576.65	607.5	0.645	6.44

Table 10.1: Summary of simulations for Variant A

The results of the simulations are compared at the level of opening 3 in **Figures 10.46 and 10.47**.

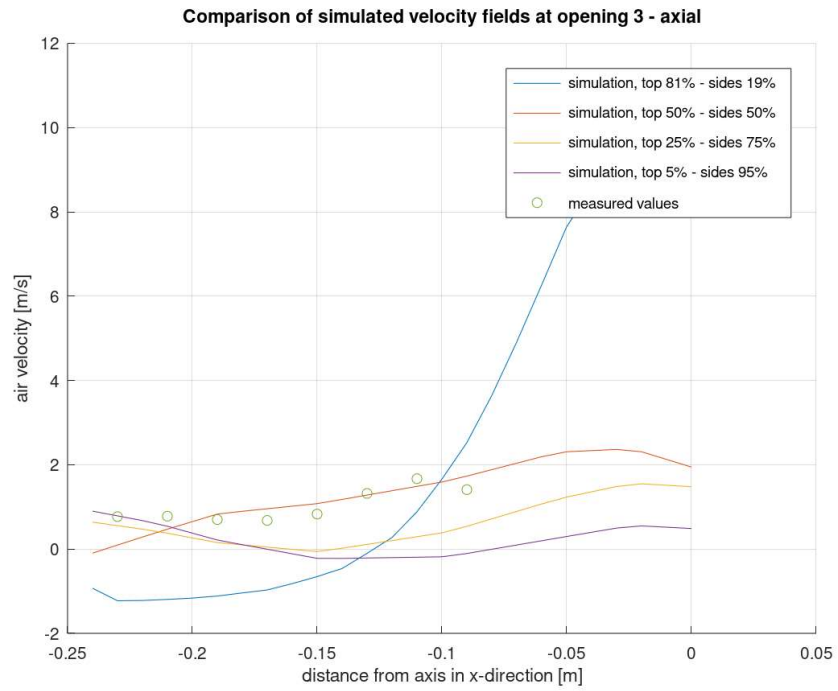


Figure 10.46: Geometry A - comparison of simulations at opening 3 – axial

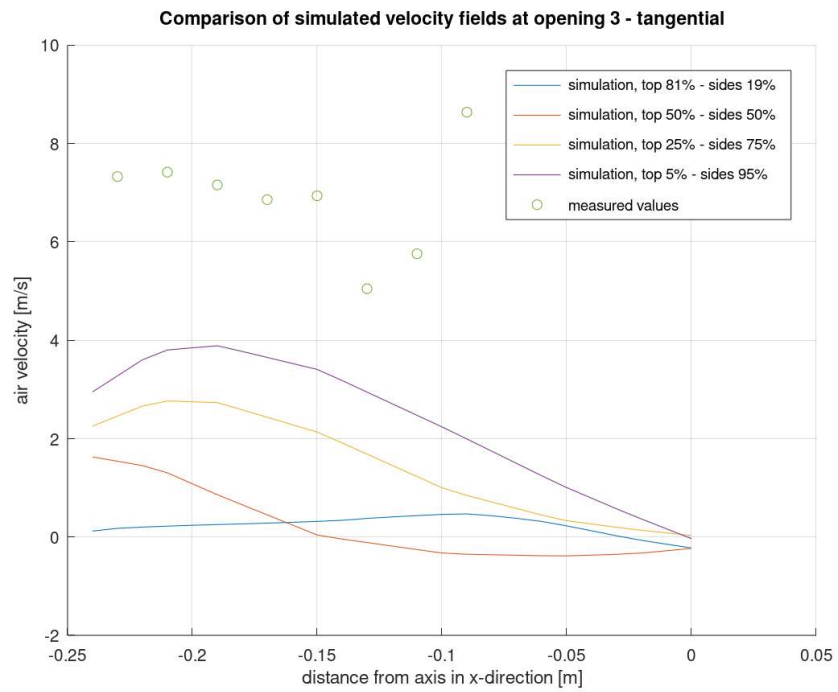


Figure 10.47: Geometry A - comparison of simulations at opening 3 – tangential

As can be seen in the graphs, the simulated axial flow rate corresponds well with reality in the case of the **Simulation 2**, nevertheless, the measured tangential velocity is much higher than for any of the author's simulations. This leads to the conclusion that the total air flow through the system was in reality much higher than the value than was reported to the author.

Thus the author's attempts to create a reliable simulation of the air velocity field inside the dryer have been frustrated by an error during the measurement at which the author was not present in the case of Variant A and by unexplained inaccuracies in the case of Variant B relating to the tangential velocity. Therefore the author will limit his observations of how to optimise the geometry of the dryers to improve their performance, to observations from the experimental results. These are as follows:

Observations for Variant A. The measured results show that the air velocity profile inside the dryer is as expected. The axial velocity is low, though it rises gradually nearer the axis of the chamber, and the linear tangential velocity is higher towards the edge of the chamber, due to a near constant angular velocity. There are no dead spots at the points at which velocity was measured. We therefore conclude that the system is correctly set up, and the only improvements to be made are upgrades to the design, such as the cyclonic separation mechanism used in Variant B.

Conceptually (and as can be seen in the numerical model), there should be a spike in the axial air speed near the central (axial) entrance. This means that the drying chamber needs to be slightly oversized, since the top space is wasted, before the momentum of the entering air is dissipated by the tangential streams. This can be resolved by routing all the incoming air through the side streams (as in Variant B) or by using a baffle plate to absorb the momentum of the air column. Alternatively, it may also be interesting to investigate the effects of shifting the axial inlet off-center so that the flow path of entering air lies directly in front of the tangential streams. This may however cause insymmetricities in the airflow inside the chamber.

Observations for Variant B. Once again we observe high tangential velocities towards the edge of the drying chamber which decrease closer to the axis. Axial velocities are also satisfactorily low, except near the wall of the chamber, though this may be explained naturally. As air spins around the inside of the dryer, centrifugal forces will force air molecules towards the edge leading to higher flow rates, both axial and tangential. Nevertheless, this spike in vertical velocity (to about 3 m/s) at the edge may also be due to the angle of the blades on the interior cone being too shallow, since they act more on

the air in the centre of the chamber than on the air at the extremity. Should this be the issue, one solution would be to angle the blades more steeply, increasing the overall axial velocity, but reducing it at the edge. Should this be undesirable, then the author recommends elongating the blades.

General comments. The author recommends that the measurement of Variant A be repeated and more care be taken while reading the inlet flow velocities. Should this be impractical, further simulations could be run increasing the flow rate through the whole system until a suitable approximation is found, however this requires optimising two variables: the flow rate through the whole system, and the ratio of air flowing through the top and side inlets into the chamber.

The author would also recommend modifying the mesh of Variant A, modelling the unit as separate regions and applying a simplified and more appropriate mesh accordingly (creating a mesh similar to the one used to model Variant B).



Chapter 11

Conclusion



11.1 General summary

During the time that the author has been involved in the project, a large range of work has been undertaken.

The author has successfully conducted a study of the literature relating to the creation of nanoparticles in the food industry, explaining the basics of food dehydration, as well as a review of drying technology and modern trends. Furthermore, the author explained the methods by which nanoparticles are produced and how they can be dried and separated. Finally the author focused on supercritical assisted atomisation, explaining the history of its development and the advantages it holds over other methods.

Subsequently, the current work by the department and its partners to investigate SAA on their laboratory-scale dryer was outlined. The author presented the preliminary design for the dryer, followed by a more detailed description of the system, which was the work of Ing. Skočilas, Ph.D. Following this was an explanation of the measurements and tests which had been conducted on the equipment, including the ones at which the author had been present.

The author then presented a Matlab model for calculating the mass flow rates inside the system, which was his own creation. This script can be used

in further work on the system, or adapted to new variants with only minor adjustments. In applying the model to one of the measurements, the author estimated the amount of leakage in the system as being 39.73% of the dry air and proved that one of the humidity sensors was malfunctioning.

In the following chapter, the author outlined his work in ANSYS to model the airflow inside the drying chamber. The initial work had been conducted within the wider framework of the author's studies, providing two models, one for each configuration of the dryer's geometry to be compared with measured values of air speed. The first of these was inaccurate, and the second matched the measured values in the axial direction, but not in the tangential. For this thesis, the author expanded his original work, supposing that he had been provided with inaccurate data for the airflow in the first part. By running numerous other simulations, the author was able to improve his model to have the correct airflow characteristics, though he did not find a satisfactory flow rate of air through the system, since the solution is an optimisation problem with two parameters, and each iteration involves running a simulation in Fluent. The author judged this was ineffective and not worth the effort.

■ 11.2 Recommendations

■ 11.2.1 General comments

Several recommendations for those involved in the project and for those conducting similar research are now proposed.

First of all, it is crucial that communication between the various parties involved in the project improve. During the author's involvement in the project, he noted several instances where a confusion relating to expectations or information transfer lead to a loss of time or unnecessary work.

Next, the measurement protocol should be observed carefully, and the results recorded and stored accessibly and comprehensibly. Again, much time was wasted piecing together information from various sources, correcting errors made during the measurements, all of which hampered the quality of the research, particularly around the CFD analysis.

11.2.2 Technical recommendations

The first improvement that the author recommends is to reduce the leakage in the system by checking the pipe fittings and connections. A significant amount of air was lost in the dryer, reducing the accuracy of any estimates.

Next, it is necessary for further measurements to use sensors with the correct working parameters. Temperature and humidity sensors should be working within their designed range to avoid damage, and an anemometer with a range up to at least 25 m/s should be used.

Furthermore, the low relative humidity of the air at the output (calculated at 9.278%), combined with the low drop in temperature suggests that far more solution could be dried for the used airflow. Perhaps two or three more nozzles could be added to increase the flow rate of solution, which would render the dryer far more efficient.

As regards improving the geometry of the dryer A, the author is unable to comment with much confidence, since despite his best efforts and lots of time spent tuning Fluent models, he was not able to correct the error in the given data. Nevertheless, he observed from the models that the higher the ratio of air flowing through the side inlets over the axial entrance, the faster the tangential velocity, and less turbulent motion was observed. This has the advantage of producing a more consistent residence time of air in the chamber and therefore a more even nanoparticle quality, since random eddies are eliminated. Another suggestion is to use a baffle plate before the top inlet to speed up mixing in the different streams.

For geometry B, the flow pattern in the model is consistent and nearly ideal. However the velocity of air is particularly slow in the area on the outside of the central tube (see **Figure 10.34**), suggesting that the tube could be enlarged. The effect of this modification would however need to be checked by a further simulation. On the other hand, the measured data shows that there is a spike in axial velocity at the outer edge of the drying chamber. The author suggested in **Chapter 10** that this could be resolved by resetting the blade angles or modifying their geometry.



Table of symbols

Symbol	Unit	Definition
<i>Latin</i>		
A	m^2	surface area
c_p	$\text{kJ.kg}^{-1}.\text{K}^{-1}$	specific heat capacity
c_s	$\text{kJ.kg}^{-1}.\text{K}^{-1}$	specific heat capacity of moist air
c_{pp}	$\text{kJ.kg}^{-1}.\text{K}^{-1}$	specific heat capacity of dry product
c_{pw}	$\text{kJ.kg}^{-1}.\text{K}^{-1}$	specific heat capacity of liquid water
D_{eff}	$\text{m}^2.\text{s}^{-1}$	effective diffusivity
H_a	kJ.kg^{-1}	enthalpy of air
H_p	kJ.kg^{-1}	enthalpy of product
L	kJ.kg^{-1}	latent heat of vaporisation of water
\dot{m}_a	kg.s^{-1}	humid air flow rate
m_{da}	kg	mass of dry air
\dot{m}_{da}	kg.s^{-1}	dry air flow rate
m_{dp}	kg	mass of dry product
\dot{m}_{dp}	kg.s^{-1}	dry product flow rate
m_w	kg	mass of water
N	$\text{kg.m}^{-2}.\text{h}^{-1}$	drying rate
p_w	Pa	partial pressure of water vapour
p'_w	Pa	saturation pressure of water vapour
q	kJ.s^{-1}	heat losses in the dryer
t	s or h	time
T	K	temperature
T_a	K	temperature of air
T_p	K	temperature of product
T_0	K	reference temperature equal to 25°C
W	$\text{kg}_{\text{water}}/\text{kg}_{\text{dry product}}$	dry basis moisture content of a product
X	$\text{kg}_{\text{water}}/\text{kg}_{\text{dry air}}$	absolute humidity of air
<i>Greek</i>		
λ	$\text{W.m}^{-1}.\text{K}^{-1}$	heat conductivity
ρ	kg.m^{-3}	density
φ	-	relative humidity

Table 11.1: List of symbols used in Part I

Symbol	Unit	Definition
<i>Latin</i>		
C_D	-	drag coefficient for a sphere
D	m	internal diameter of the drying chamber
F	N	force
g	m/s ²	acceleration due to gravity ($g = 9.81 \text{ m/s}^2$)
h_A	kJ/kg	enthalpy difference of air
d	nm	particle diameter
H	m	height of the cylindrical part of the chamber
\dot{M}_A	kg/h	mass flow rate of drying air
P_{atm}	MPa	atmospheric pressure of air
Re	-	Reynolds number
t_A	°C	temperature of air
T_{atm}	°C	atmospheric temperature of air
u_t	m/s	terminal velocity of falling particle
\dot{V}_A	m ³ /h	volumetric flow rate of air
V_{DC}	m ³	internal volume of the drying chamber
W	kg/h	mass of evaporated water per hour
x_A	kg _{water} /kg _{dry air}	moisture content of air
<i>Greek</i>		
μ	Pa.s	dynamic viscosity of air
ρ_A	kg/m ³	density of air
ρ_P	kg/m ³	density of particle
τ_A	s	residence time of air in the drying chamber

Table 11.2: List of symbols used in Part II



Bibliography

- [1] W. Abdelwahed, G. Degobert, S. Stainmesse, and H. Fessi. Freeze-drying of nanoparticles: Formulation, process and storage considerations. *Advanced Drug Delivery Reviews*, 58:1688–1713, 2006.
- [2] E. Acosta. Bioavailability of nanoparticles in nutrient and nutraceutical delivery. *Current Opinion in Colloid & Interface Science*, 2009.
- [3] R. Adami, A. D. Capua, and E. Reverchon. Supercritical assisted atomization for the production of curcumin-biopolymer microspheres. *Powder Technology*, 305:455–461, 2017.
- [4] L. Alexandrescu, K. Syverud, A. Nicosia, G. Santachiara, A. Fabrizi, and F. Belos. Airborne nanoparticles filtration by means of cellulose nanofibril based material. *J. of Biomaterials and Nanobiotechnology*, pages 29–36, 2016.
- [5] V. Arrondel and G. Bacchiega. Nanoparticle and fine particle collection efficiency using an electrostatic precipitator: a description of the specific physical processes. *ICESP*, 2016.
- [6] M. Beran, J. Drahorad, O. Vltavsky, M. Urban, I. Laknerova, M. Fronek, J. Sova, J. Ondracek, L. Ondrackova, M. Kralova, and S. Formankova. Pilot-scale production and application of microparticulated plant proteins. *Journal of Nutrition & Food Sciences*, 8, 2018.
- [7] Z. Bourezg, S. Bourgeois, S. Pressenda, T. Shehada, and H. Fessi. Redispersible lipid nanoparticles of spironolactone obtained by three drying methods. *Colloids and Surfaces A: Physicochemical and Engineering Aspects*, 413:191–199, 2012.

- [8] P. J. C. Chen, W. Liu and T. Hong. Coaxial electrohydrodynamic atomization for the production of drug-loaded micro/nanoparticles. *Micromachines*, 2019.
- [9] Y. Chang, X. Yan, Q. Wang, L. Ren, J. Tong, and J. Zhou. High efficiency and low cost preparation of size controlled starch nanoparticles through ultrasonic treatment and precipitation. *Food Chemistry*, 227:369–375, 2017.
- [10] C. Charcosset. Preparation of nanomaterials for food applications using membrane emulsification and membrane mixing. In *Emulsions, Nanotechnology in the Agri-Food Industry*, volume 4, chapter 2, pages 37–69. Academic Press, 2016.
- [11] H. Chien, Y. Hsu, and J. Tsai. Method of collecting nanoparticles by using a cyclone and method of designing the cyclone, Int. Cl. B01D45/16, US Patent 6 969 420, 4th Dec.2005.
- [12] R. Couto, V. Alvarez, and F. Temelli. Encapsulation of vitamin b2 in solid lipid nanoparticles using supercritical co2. *The Journal of Supercritical Fluids*, 120:432–442, 2017.
- [13] D. Czernia and B. Haponiuk. Air density calculator. [online] Available at: <https://www.omnicalculator.com/physics/air-density#how-to-calculate-the-air-density>, 2013. [Accessed: 2020-06-17].
- [14] P. Ditl and M. Netušil. *Bilancování a simulace systémů v MS Excel*. Česká technika - nakladatelství ČVUT, 2018.
- [15] S. Ebert, C. K. W. Koo, J. Weiss, and D. J. McClements. Continuous production of core-shell protein nanoparticles by antisolvent precipitation using dual-channel microfluidization: Caseinate-coated zein nanoparticles. *Food Research International*, 92:48–55, 2017.
- [16] S. Emami, S. Azadmard-Damirchi, S. H. Peighambari, H. Valizadeh, and J. Hesari. Liposomes as carrier vehicles for functional compounds in food sector. *Journal of Experimental Nanoscience*, 11:737–759, 2016.
- [17] EngineeringToolBox. Water vapor and saturation pressure in humid air. [online] Available at: https://www.engineeringtoolbox.com/water-vapor-saturation-pressure-air-d_689.html, 2004. [Accessed: 2020-06-17].
- [18] P. Evans. Properties of air at atmospheric pressure. [online] Available at: <https://theengineeringmindset.com/properties-of-air-at-atmospheric-pressure/>, 2015. [Accessed: 2020-02-26].
- [19] S. Galindo-Rodriguez, E. Allémann, H. Fessi, and E. Doelker. Physicochemical parameters associated with nanoparticle formation in the salting-out, emulsification-diffusion, and nanoprecipitation methods. *Pharmaceutical Research*, 21, 2004.

- [20] H. D. Goodfellow and E. Tähti. *Industrial ventilation design guidebook*. Academic, 2001.
- [21] J. Gou, J. Zhuge, and F. Liang. Processing of polymer nanocomposites. In *Manufacturing Techniques for Polymer Matrix Composites (PMCs)*. Woodhead Publishing, 2012.
- [22] M. Hladíková. unpublished internal documentation. České vysoké učení technické v Praze, Fakulta strojní, Ústav procesní a zpracovatelské techniky, 2020.
- [23] P. Hoffman, J. Skočilas, and T. Jirout. Výpočtová zpráva analýzy procesu sušení a návrhu rozprašovací sušárny projektu „optimalizace zařízení pro sušení biologických látek atomizací stlačeným oxidem uhličitým - návrh a zhotovení laboratorní jednotky, měřící optimální čas zdržení sušených partikulí (mikro a nano částic) v nových high-tech sušárnách“. České vysoké učení technické v Praze, Fakulta strojní, Ústav procesní a zpracovatelské techniky, 2018.
- [24] P. Hoffman, J. Skočilas, and P. M. Tomáš Jirout. Popis funkčního vzorku – měření a regulace demonstrátoru „optimalizace zařízení pro sušení biologických látek atomizací stlačeným oxidem uhličitým - návrh a zhotovení laboratorní jednotky, měřící optimální čas zdržení sušených partikulí (mikro a nano částic) v nových high-tech sušárnách“. České vysoké učení technické v Praze, Fakulta strojní, Ústav procesní a zpracovatelské techniky, 2018.
- [25] A. Jahangiri and L. Barghi. Polymeric nanoparticles: review of synthesis methods and applications in drug delivery. *J. of Advanced Chemical and Pharmaceutical Materials*, 1:38–47, 2018.
- [26] S. Jangam, C. Law, and A. Mujumdar. *Drying of Foods, Vegetables and Fruits - Volume 1*. Nottingham University Singapore, 2010.
- [27] A. Jaworek. Micro- and nanoparticle production by electrospraying. *Powder Technology*, 176, 2007.
- [28] P. Joholm, D. B. Ingham, M. Lehtimaki, L. Perttu-Roiha, H. Goodfellow, and H. Torvela. Gas-cleaning technology. In *Industrial Ventilation Design Guidebook*, chapter 13, pages 1197–1316. Academic Press, 2001.
- [29] W. H. Khan and V. K. Rathod. Process intensification approach for preparation of curcumin nanoparticles via solvent–nonsolvent nanoprecipitation using spinning disc reactor. *Chemical Engineering and Processing: Process Intensification*, 80:1–10, 2014.
- [30] C. S. Kim, L. Bao, K. Okuyama, M. Shimada, and H. Niinuma. Filtration efficiency of a fibrous filter for nanoparticles. *J. of Nanoparticle Research*, pages 215–221, 2006.

- [43] C. J. M. Rivas, M. Tarhini, W. Badri, K. Miladi, H. Greige-Gerges, Q. A. Nazari, S. A. G. Rodríguez, R. A. Román, H. Fessi, and A. Elaisari. Nanoprecipitation process: From encapsulation to drug delivery. *International J. of Pharmaceutics*, 532, 2017.
- [44] W. S. Saada and R. K. Prud'homme. Principles of nanoparticle formation by flash nanoprecipitation. *Nanotoday*, 11, 2016.
- [45] H. Saari, C. Fuentes, M. Sjöö, M. Rayner, and M. Wahlgren. Production of starch nanoparticles by dissolution and non-solvent precipitation for use in food-grade pickering emulsions. *Carbohydrate Polymers*, 157:558–566, 2017.
- [46] P. Sanguansri and M. A. Augustin. Nanoscale materials development – a food industry perspective. *Trends in Food Science & Technology*, 2006.
- [47] F. Santeramo, D. Carlucci, et al. Emerging trends in european food, diets and food industry. *Food Research International*, 2017.
- [48] B. S. Sekhon. Food nanotechnology – an overview. *Dove Medical Press*, 2010.
- [49] A. Shariati and C. J. Peters. Recent developments in particle design using supercritical fluids. *Current Opinion in Solid State and Materials Science*, 7:371–383, 2003.
- [50] P. Sheth, H. Sandhu, D. Singhal, W. Malick, N. Shah, and M. S. Kislalioglu. Nanoparticles in the pharmaceutical industry and the use of supercritical fluid technologies for nanoparticle production. *Current Drug Delivery*, 9:269–284, 2012.
- [51] R. E. Sievers, U. Karst, P. D. Milewski, S. P. Sellers, B. A. Miles, J. D. Schaefer, C. R. Stoldt, and C. Y. Xu. Formation of aqueous small droplet aerosols assisted by supercritical carbon dioxide. *Aerosol Science and Technology*, pages 3–15, 1999.
- [52] R. E. Sievers, P. D. Milewski, S. P. Sellers, B. A. Miles, B. J. Korte, K. D. Kusek, G. S. Clark, B. Mioskowski, and J. A. Villa. Supercritical and near-critical carbon dioxide assisted low-temperature bubble drying. *Industrial & Engineering Chemistry Research*, 39:4831–4836, 2000.
- [53] R. Singh and D. Heldman. *Introduction to food engineering*. Elsevier/Academic Press, 4th edition, 2009.
- [54] J. Skočilas, M. Beran, J. Drahorád, J. Ondráček, P. Hoffman, and T. Jirout. Drying chamber for spray nebulization drying – experimental investigation. currently unpublished.
- [55] B. Stella, A. Marengo, and S. Arpicco. Nanoparticles: and overview of the preparation methods from preformed polymers. *Istituto Lombardo - Accademia Di Scienze E Lettere - Incontri Di Studio*, 2017.

- [56] C. Y. Tai, Y. H. Wang, and H. S. Liu. A green process for preparing silver nanoparticles using spinning disk reactor. *Wiley InterScience*, 2007.
- [57] M. Thiruvengadam, G. Rajakumar, and I. M. Chung. Nanotechnology: current uses and future applications in the food industry. *Springer-Verlag*, 2018.
- [58] R. Vehring, H. Snyder, and D. Lechuga-Ballesteros. Spray drying. In *Drying Technologies for Biotechnology and Pharmaceutical Applications*, chapter 7. Wiley-VCH Verlag GmbH & Co. KGaA, 2020.
- [59] J. Weiss, P. Takhistov, and D. J. McClements. Functional materials in food nanotechnology. *J. of Food Science*, 71, 2006.
- [60] W. Peukert and C. Wadenpohl. Industrial separation of fine particles with difficult dust properties. *Powder Technology*, 118:136–148, 2001.
- [61] Y. Wu, B. Yu, A. Jackson, W. Zha, L. J. Lee, and B. E. Wyslouzil. Coaxial electrohydrodynamic spraying: A novel one-step technique to prepare oligodeoxynucleotide encapsulated lipoplex nanoparticles. *Molecular Pharmaceutics*, 2009.



Appendices



Appendix A

Process Flow Diagrams

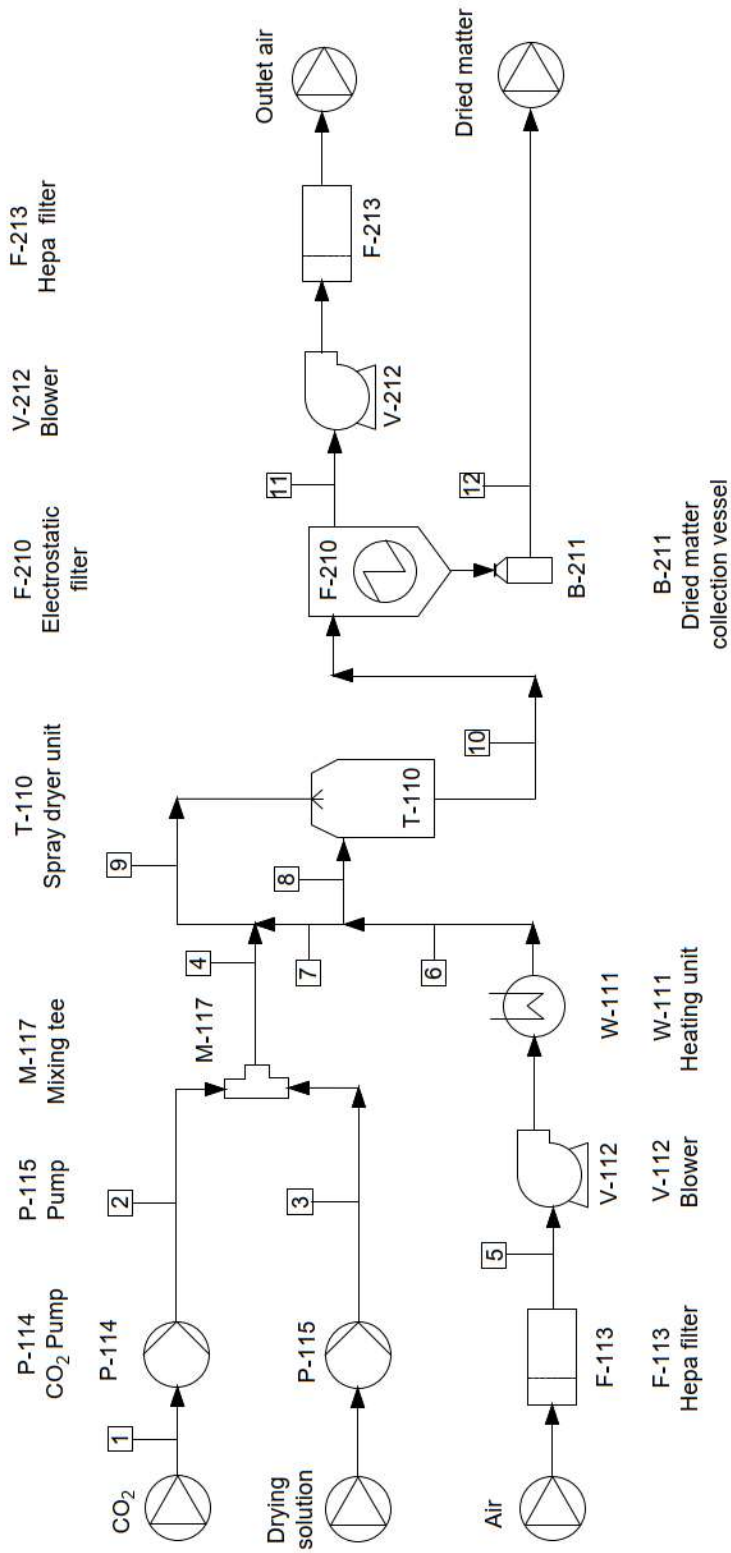


Figure A.1: Process Flow Diagram for Variant A

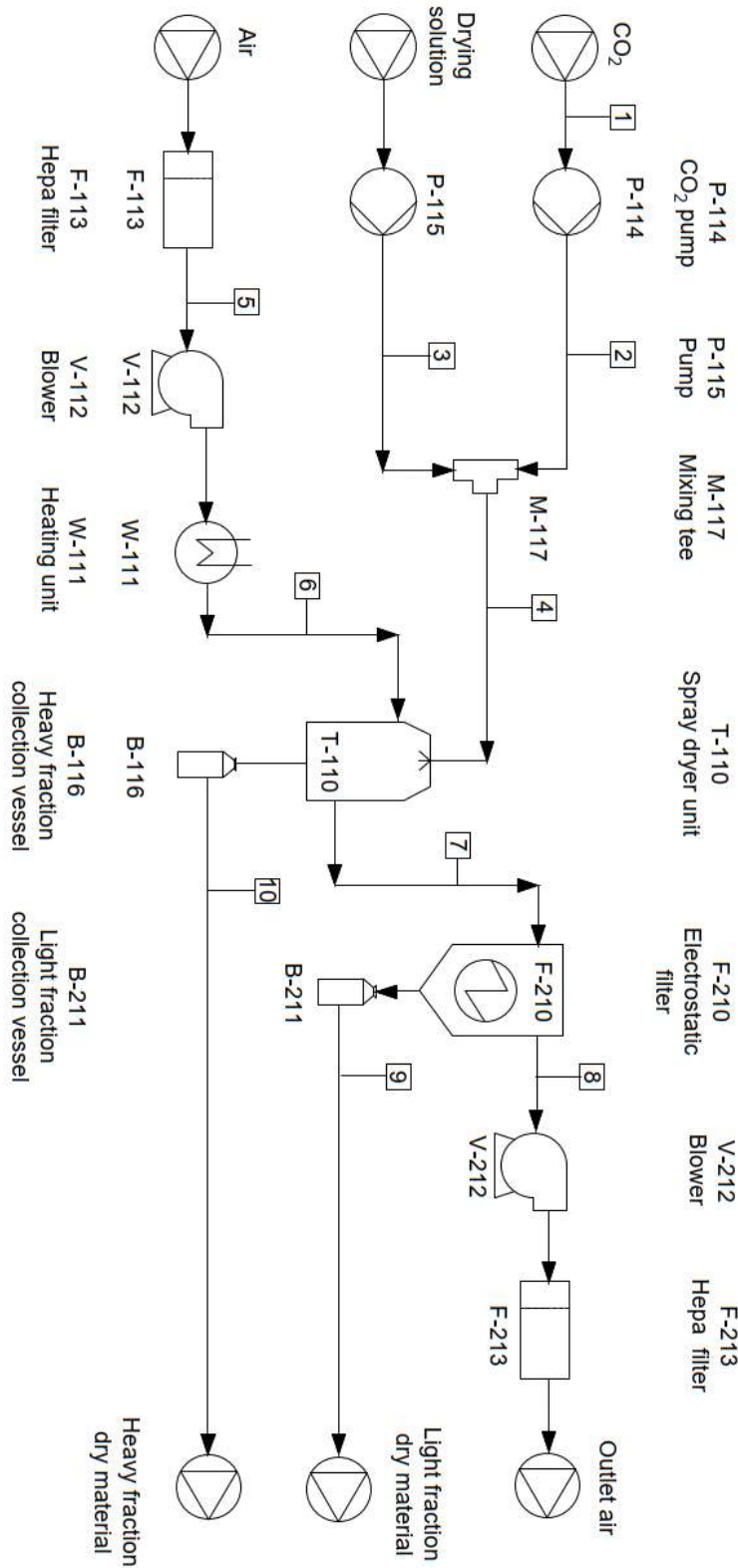


Figure A.2: Process Flow Diagram for Variant B



Appendix B

Overview of measurements

This summary was compiled by Ing. Hladíková as part of her work on the project.

B. Overview of measurements

	1st measurement	2nd measurement	3rd measurement	4th measurement	5th measurement	6th measurement	7th measurement	8th measurement	9th measurement	10th measurement	11th measurement
GENERAL	measurement overseen by	Hladkova	Hladkova	Hladkova	Vitavsky	Vitavsky	Vitavsky	Vitavsky	Dimmock	Dimmock	Dimmock
	measurement date	10, 11 and 15.4.2019	20. 5. 2019	20. 5. 2019	28. 5. 2019	4. and 10. 6. 2019	1. and 2. 8. 2019	5. 8. 2019	12. 8. 2019	12. 8. 2019	18. 8. 2019
CONDITIONS	temperature [°C]	16	16	16 a 19	19	20 a 21	X	X	X	X	X
	humidity [%]	49	49	49 a 45	62	50 a 44	X	X	X	X	X
	inlet temperature [°C]	X	X	X	X	X	24.6 a 23.8	24.25	43.13	64.81	65.25
	inlet humidity [%]	X	X	X	X	X	49.7 a 40.8	47.9	50	46.9	46
	outlet humidity [%]	X	X	X	X	X	53.2 a 49	51.2	28.4	17.7	22.5
MEDIUM	air	YES	YES	YES	YES	YES	YES	YES	YES	YES	YES
	water	NO	NO	NO	NO	NO	NO	NO	NO	NO	NO
	quantity of water	X	X	X	X	X	X	X	X	X	25 ml/min
	CO2	NO	NO	NO	NO	NO	NO	NO	NO	NO	YES
	quantity of CO2	X	X	X	X	X	X	X	X	X	20 ml/min
EQUIPMENT	configuration A	YES	NO	NO	NO	NO	NO	NO	NO	NO	NO
	configuration B	NO	YES	YES	YES	YES	YES	YES	YES	YES	YES
	valve angle [°]	40	X	X	X	X	X	X	X	X	X
	number of blades	8	8	8	8	8	8	8	8	8	8
	angle of blades [°]	X	65	65	65	50	50	50	50	50	50
	inlet blower	YES	NO	YES	YES	YES	YES	YES	YES	YES	YES
	outlet blower	YES	NO	YES	YES	YES	YES	YES	YES	YES	YES
	power of output blower [W]	100	X	100	100	100	100	100, 80, 40, 20, 0	100	100	100
FLOW RATES	opening after the temperature sensor	YES	YES	YES	YES	YES	YES	YES	YES	YES	YES
	opening after the valve	YES	NO	NO	NO	NO	NO	NO	NO	NO	NO
	opening after the filter	NO	YES	YES	NO	YES	YES	YES	YES	YES	YES
	opening after the temp. sensor (pipe diameter) [mm]	130	130	130	130	130	130	130	130	130	130
	opening after the filter (pipe diameter) [mm]	100	100	100	100	100	100	100	100	100	100
MEASUREMENTS	duration of measurement in each position [min]	1	1	1	1	1	1	1	1	1	1
	1st opening	YES	NO	NO	NO	YES	YES	NO	NO	NO	NO
	2nd opening	YES	NO	YES	NO	YES	YES	NO	NO	NO	NO
	3rd opening	YES	NO	YES	NO	YES	YES	NO	NO	NO	NO
	4th opening	YES	NO	YES	NO	YES	YES	NO	NO	NO	YES
	5th opening	YES	NO	YES	NO	YES	YES	NO	NO	NO	YES
	6th opening	NO	NO	NO	NO	NO	NO	NO	NO	NO	NO
	7th opening	NO	NO	NO	YES	YES	YES	NO	NO	NO	NO
	8th opening	NO	NO	NO	YES	YES	YES	NO	NO	NO	YES
	9th opening	NO	NO	NO	NO	YES	YES	NO	NO	NO	YES
	large opening (outer cone) 10th opening	NO	NO	NO	NO	NO	NO	NO	NO	NO	NO
	small opening (outer cone) 11th opening	NO	NO	NO	NO	NO	NO	NO	NO	NO	NO
PROBE ANGLE [°]	0	YES	NO	YES	YES	YES	YES	NO	NO	NO	YES
	45	YES	NO	NO	NO	NO	NO	NO	NO	NO	NO
	90	YES	NO	YES	YES	YES	YES	NO	NO	NO	YES
	135	YES	NO	NO	NO	NO	NO	NO	NO	NO	NO
	180	YES	NO	NO	NO	NO	NO	NO	NO	NO	NO
	225	YES	NO	NO	NO	NO	NO	NO	NO	NO	NO
	270	YES	NO	NO	NO	NO	NO	NO	NO	NO	NO
	315	YES	NO	NO	NO	NO	NO	NO	NO	NO	NO

Figure B.1: Overview of measurements

Appendix C

Mass balance MATLAB scripts

Here the author presents his own MATLAB code for the various calculations relating to balancing mass flow rates in the system.

C.1 Flow rate integration from measured points

C.1.1 Inlet flow rate

```
% --- Flow rate through inlet pipe - rectangular integration
% VolFR = vel * Area
%volume of cylinder: V = h(vel) * (d2^2-d1^2)*PI/4 (area)
d = 0.13; %[m] diameter of cylinder
%data
%col 1 - measured distance; col 2 - axial velocity
vel = [
0 0
0.01 10.23
```

```
0.02 9.16
0.03 10.81
0.04 11.12
0.05 10.95
0.06 11.19
];

%radius vector = distance from centre
r = zeros(7, 1);

for i = 1:length(r)
    r(i) = 0.065 - vel(i,1);
endfor

r;

%integral = volumetric flow rate
Vol = 0;

for i = 1:length(r)
    if i < length(r)
        Vol = Vol + pi * (r(i)^2-r(i+1)^2)*vel(i,2);
    elseif i == length(r)
        Vol = Vol + pi * (r(i)^2)*vel(i,2);
    end
    i;
endfor

Vol %vol flow rate [m^3/s]
```

■ C.1.2 Outlet volumetric flow rate

```
% --- Flow rate through outlet pipe - rectangular integration

%VolFR = vel * Area

%volume of cylinder: V = h(vel) * (d2^2-d1^2)*PI/4 (area)

d = 0.10; %[m] diameter of pipe
```



```

%col 1 - measured distance; col 2 - axial velocity
vel = [
0 0
0.02 20.47 %average
0.04 20.725 %average - one value over maximum
];

%radius vector = distance from centre
r = zeros(3, 1);

for i = 1:length(r)
    r(i) = 0.05 - vel(i,1);
endfor

r;

%integral = volumetric flow rate
Vol = 0;

for i = 1:length(r)
    if i < length(r)
        Vol = Vol + pi * (r(i)^2-r(i+1)^2)*vel(i,2);
    elseif i == length(r)
        Vol = Vol + pi * (r(i)^2)*vel(i,2);
    end
    i;
endfor

Vol %vol flow rate [m^3/s]

```

■ C.1.3 Outlet mass flow rate

```

%MODEL: Mass balance
  |--SYSTEM: Dryer, geometry B
  |--DATA: MEASUREMENT 11

% Calculating outlet mass flow rate

%----- Input values -----

```

```
Vout = 0.057958 %[m3/s] Oultet volumetric flow rate
Tout = 57.06; %[deg C] temperature of air in pipe
RHout = 0.176; %[\] from measured data, relative humidity
Pamb = 101325; %[Pa] pressure in pipe (ambient pressure

%----- Calculation -----

%Air density
[densout, AHout, Xdryout] = pressure_rel2mc (RHout, Tout, Pamb)
    %[kg/m3], [kg/m3], [kg_v/kg_da]

%Mass flow
Mout = densout*Vout
    %[kg/s] mass flow rate of moist air in stream 6

Mwout=Xdryout/(1+Xdryout)*Mout
Maout = Mout - Mwout
```

■ C.2 Psychrometric recalculations

The author devised two functions for calculating between moisture content, relative humidity, absolute humidity, and for finding the density of moist air at a given temperature.

■ C.2.1 Moisture content to relative humidity function

```
function [density, AH, RH] = pressure_mc2rel (Xdry, Tcel, Pamb)
%Converting from (dry basis) moisture content to relative
    humidity(through Abs. Hum)
%also outputs density of air
%sources: https://planetcalc.com/2167/ and
https://www.omnicalculator.com/physics/air-density#how-to-calculate-the-air-density
```

```

Rda = 287.058; %specific gas k for dry air
Rv = 461.495; %specific gas k for water vapour
T = Tcel+273.15; %conversion to kelvins

Psat = exp((77.3450 + 0.0057*T - 7235 / T)) / T^(8.2);
    %[Pa] source: https://www.engineeringtoolbox.com
    /water-vapor-saturation-pressure-air-d_689.html

Pv = Xdry*Pamb / (Rda/Rv+Xdry); %[Pa] vapour partial pressure
Pda = Pamb - Pv; % Dry air partial pressure

AH = Pv/(Rv*T); %absolute humidity = m/V [kg/m3]
Xdry = AH/(Pda/(Rda*T));
    %Dry basis water content [kg_vap/kg_dryair]

density = Pda/(Rda*T) + Pv/(Rv*T); %wet air density IGE

RH = Pv/Psat; % relative humidity

endfunction

```

■ C.2.2 Relative humidity to moisture content function

```

function [density, AH, Xdry] = pressure_rel2mc (RH, Tcel,
Pamb)
%Converting from relative humidity to moisture content
    (through Abs. Hum)
%also outputs density of air
%sources: https://planetcalc.com/2167/ and
    https://www.omnicalculator.com/physics/
    air-density#how-to-calculate-the-air-density

Rda = 287.058; %specific gas k for dry air
Rv = 461.495; %specific gas k for water vapour
T = Tcel+273.15; %conversion to kelvins

Psat = exp((77.3450 + 0.0057*T - 7235 / T)) / T^(8.2);
    %[Pa] source: https://www.engineeringtoolbox.com
    /water-vapor-saturation-pressure-air-d_689.html
Pv = RH*Psat; %vapour partial pressure

```

```
Pda = Pamb - Pv; % Dry air partial pressure

density = Pda/(Rda*T) + Pv/(Rv*T); %wet air density IGE

AH = Pv/(Rv*T); %absolute humidity = m/V [kg/m3]

Xdry = AH/(Pda/(Rda*T)); %Dry basis water content
      [kg_vap/kg_dryair]

endfunction
```

■ C.3 Balance model

The balance model, composed of three parts, contains the script for calculating the ideal flow rates in each stream of the dryer system. It can be easily altered to accommodate any modifications to the dryer system.

A description is included in **Chapter 9**.

■ C.3.1 Script: measurement11.m

```
%MODEL: Mass balance
  %--SYSTEM: Dryer, geometry B
  %--DATA:   MEASUREMENT 11

%=====Technical information=====

% Balanced quantity MASS [kg]

%--STREAMS used as listed in PFD

%--COMPONENTS
%1 Water
%2 CO2
%3 Air
```

```

%4 Dry matter

%%--PROCESSING UNITS
%1 Spray Dryer
%2 Heating Unit
%3 CO2 pump (+Cooling Unit)
%4 Electrostatic Filter
%5 Mixing unit_streams 2, 3

%===EDIT=====Input parameters=====
clear all

%Variable measurements
Tamb = 20; %[Celcius] Ambient Temperature
Pamb = 101325; %[Pa] Ambient Pressure
Vco2 = 20; %[ml/min] Inlet flowrate of CO2
Vsol = 20; %[ml/min] Inlet flowrate of solution
M_lfrac = 0.0; %[kg/h] Mass flowrate of dry matter + water
    %LIGHT FRACTION (separated by electrofilter)
M_hfrac = 0.0; %[kg/h] Mass flowrate of dry matter + water
    %HEAVY FRACTION (separated by cyclone)
RH5 = 0.46; %[/] Relative humidity at inlet before heating
T6 = 65.25; %[Celcius] Moist air temperature after heating -
    %Redundant if calculating added heat by heaters.
    %Used to find M6.
V6 = 0.096610; %[m/s] integrated Vol. air flow rate - inlet
X9 = 0.05; %[kg_water/kg_drymatter] Moisture content of
    %light fraction - dry basis
X10 = 0.05; %[kg_water/kg_drymatter] Moisture content of
    %heavy fraction - dry basis

%Geometry
D6 = 0.130; %[m] inlet pipe diametre
D8 = 0.100; %[m] outlet pipe diametre

%Fixed values
dens_sol = 998; %[kg/m3] Density of solution (water at 20degC)
dens_co2 = 140.65; %[kg/m3] density of liquid co2

%===DO NOT EDIT=====RELAYING TO GEOMETRY=====

Params = [Tamb, Pamb, Vco2, Vsol, M_lfrac, M_hfrac, RH5, T6,
V6, X9, X10, D6, dens_sol, dens_co2];

[Flowrates, IOC] = geometry (Params);
    %Flowrates, [kg/s] (streams x component);

```

```
%IOS = inlet/outlet streams

%===EDIT=====DISPLAYING RESULTS=====

Flowrates

IOC;
```

■ C.3.2 Script: geometry.m

```
function [RT, IOC] = geometry (A)

    %--SYSTEM: Dryer, geometry B

    %=====Technical information=====

    % Balanced quantity MASS [kg]

    %--STREAMS used as listed in PFD

    %--COMPONENTS
    %1 Water
    %2 CO2
    %3 Air
    %4 Dry matter

    %--PROCESSING UNITS
    %1 Spray Dryer
    %2 Heating Unit
    %3 Cooling Unit
    %4 Electrostatic Filter
    %5 Mixing unit_streams 2, 3

    %===EDIT=====Input parameters=====
    %values taken from measurements

    %Variable measurements
    Tamb = A(1); %[Celcius] Ambient Temperature
    Pamb = A(2); %[Pa] Ambient Pressure
```

```

Vco2 = A(3); %[ml/min] Inlet flowrate of CO2
Vsol = A(4); %[ml/min] Inlet flowrate of solution
M_lfrac = A(5); %[kg/h] Mass flowrate of dry matter + water
    5LIGHT FRACTION (separated by electrofilter)
M_hfrac = A(6); %[kg/h] Mass flowrate of dry matter + water
    %HEAVY FRACTION (separated by cyclone)
RH5 = A(7); %[/] Relative humidity at inlet before heating
T6 = A(8); %[Celcius] Moist air temperature after heating -
    %Redundant if calculating added heat by heaters.
    %Used to find M6.
V6 = A(9); %[m/s] integrated Vol. air flow rate - inlet
X9 = A(10); %[kg_water/kg_drymatter] Moisture content of
    %light fraction - dry basis
X10 = A(11); %[kg_water/kg_drymatter] Moisture content of
    %heavy fraction - dry basis

%Geometry
D6 = A(12); %[m] inlet pipe diametre

%Fixed values
dens_sol = A(13); %[kg/m3] Density of solution
    %(water at 20degC)
dens_co2 = A(14); %[kg/m3] density of liquid co2

%===SYSTEM=====Recalculations=====

%--STREAM 6 [1,3]--

%Conversion to water content
[dens5, AH5, Xdry5] = pressure_rel2mc (RH5, Tamb, Pamb);
    %[kg/m3], [kg/m3], [kg_v/kg_da]
%Mass moist air IN_stream 6
[dens6, AH6, RH6] = pressure_mc2rel (Xdry5, T6, Pamb);
    %[kg/m3], [kg/m3], [/]. Used to find density in 6.
M6 = dens6*V6; %[kg/s] mass flow rate of moist air in stream 6

M61=Xdry5/(1+Xdry5)*M6; %[kg/s] Mass flow rate of water
M63 = M6 - M61; %[kg/s] Mass flow rate of dry air

%--STREAM 1 [2]--
M12 = Vco2 /1e6/60 * dens_co2; %[kg/s] mass flow rate of CO2

%--STREAM 9 [1,4]--
M9 = M_lfrac/3600; %[kg/s] stream 9, mass flow rate of

```

```

    %water + dry matter
    M94 = M9/(1+X9); %[kg/s] mass flowrate DM;
    M91 = M9-M94; %[kg/s] mass flowrate water

    %--STREAM 10 [1,4]--
    M10 = M_hfrac/3600; %[kg/s] stream 10, mass flow rate of
    %water + dry matter
    M10_4 = M10/(1+X10); %[kg/s] mass flowrate DM;
    M10_1 = M10-M10_4; %[kg/s] mass flowrate water

    %--STREAM 3 [1 4]--
    M3 = Vsol /1e6/60 * dens_sol;   %[kg/s] mass flow rate of
    %solution
    M34 = M94+M10_4; %[kg/s] Mass flow rate of dry matter
    M31 = M3-M34; %[kg/s] Mass flow rate of water

    %===SYSTEM=====Supplementary equations=====

    %reference stream
    %    stream comp flowrate
    RS = [ 3      1      M31 ];

    %avoiding singularities
    if M31 == 0;
        disp('no Water in stream 3')
        return
    end
    if M63 == 0;
        disp('no air in stream 6')
        return
    end
    if M94 == 0 && M10_4 == 0;
        R94_104 = 0;
    elseif M10_4 == 0;
        disp('no heavy fraction')
        return
    end

    %Relations between components
    %    stream comp  ratio stream comp
    RC= [ 3      4      M34/M31      3      1;%stream 3, dry matter/water
          6      1      M61/M63      6      3;%stream 6 (or 5), water/air
          9      4      R94_104     10     4;%dry matter, mass light

```



```

    3      1  M31/M63   6      3;%water(s3) over air(6)
    1      2  M12/M31  3      1;%CO2 in over water (3)
    9      1  X9       9      4;%stream 9, water\dry matter
    10     1  X10      10     4 %stream 10, water/dry matter
];

%===SYSTEM=====SYSTEM DESCRIPTION=====

%--MATRIX OF INCIDENCE--
%streams 1 2 3 4 5 6 7 8 9 10  block
IM = [ 0 0 0 1 0 1 -1 0 0 -1  %1
      0 0 0 0 1 -1 0 0 0 0  %2
      1 -1 0 0 0 0 0 0 0 0  %3
      0 0 0 0 0 0 1 -1 -1 0  %4
      0 1 1 -1 0 0 0 0 0 0]; %5

%--TABLE OF DATA--

% streams 1 2 3 4 5 6 7 8 9 10  component
TD = [0 0 1 1 1 1 1 1 1 1  %1
      1 1 0 1 0 0 1 1 0 0  %2
      0 0 0 0 1 1 1 1 0 0  %3
      0 0 1 1 0 0 1 0 1 1]; %4

[RT,IOC] = solver(IM, TD, RS, RC);

```

■ C.3.3 Script: solver.m

```

function [RT,IOC] = solver (IM, TD, RS, RC)

%===DO NOT EDIT=====MATRIX RESOLUTION=====

%Inlet and outlet streams
IOS = sum(IM,1);

N_unknowns = sum(sum(TD)); %number of unknowns in the system
%maybe recall at end

```

```

%--MATRIX OF BALANCE (component x block)

MB = TD * (abs(IM))';

%Calculating number of supplementary equations needed

N_balance_equations = 0;
for i = 1:size(MB, 1)
    for j = 1:size(MB,2)
        if MB(i,j) ~= 0
            N_balance_equations = N_balance_equations+1;
        end
    end
end
N_balance_equations;

N_supplementary_equations = N_unknowns-N_balance_equations;

%--MATRIX OF COEFFICIENTS--

%\\MC top part - relations taken from IM

%step 1: vertical margin -[block, component] -taken from MB
MC_Vmarg_bc = zeros (N_balance_equations,2);

k = 1;
for j = 1:size(MB,2)
    for i = 1:size(MB,1)
        if MB(i,j) ~= 0;
            MC_Vmarg_bc(k,1) = j;
            MC_Vmarg_bc(k,2) = i;
            k = k+1;
        end
    end
end
end

MC_Vmarg_bc;

%step2: horizontal margin - [stream, component] -
%taken from TD

MC_Hmarg_sc = zeros (N_unknowns,2);

k = 1;
for j = 1:size(TD,2)

```

```

    for i = 1:size(TD,1)
        if TD(i,j) ~= 0;
            MC_Hmarg_sc(k,1) = j;
            MC_Hmarg_sc(k,2) = i;
            k = k+1;
        end
    end
end
end

MC_Hmarg_sc;

%step3: now fill out the top half of MC
MC_top = zeros(N_balance_equations,N_unknowns);

for j = 1:size(MC_top,2) %column
    for i = 1:size(MC_top,1) %row
        if MC_Hmarg_sc(j,2) == MC_Vmarg_bc(i,2);
            MC_top(i,j) = IM(MC_Vmarg_bc(i,1), MC_Hmarg_sc(j,1));
        end
    end
end
MC_top;

%\MC bottom part - use supplementary equations

MC_bot = zeros(N_supplementary_equations, N_unknowns);

%step 1: Reference stream, in MC first row
for i = 1:N_unknowns;
    if RS(1) == MC_Hmarg_sc(i,1) && RS(2) == MC_Hmarg_sc(i,2);
        MC_bot(1,i) = 1;
    end
end

%step2: define the rest from RC.
%You may need to edit this section if there are
%other types of supplementary equations
for n = 1:N_supplementary_equations-1 %row - 1
    for i = 1:N_unknowns; %columns
        if RC(n,1) == MC_Hmarg_sc(i,1) && RC(n,2) == MC_Hmarg_sc(i,2);
            MC_bot(n+1,i) = 1;
        end
        if RC(n,4) == MC_Hmarg_sc(i,1) && RC(n,5) == MC_Hmarg_sc(i,2);
            MC_bot(n+1,i) = -RC(n,3);
        end
    end
end
end

```

```

end

%Linear equation in form (MC).X = B
% define B, from reference stream
B = zeros(N_unknowns,1);
B(N_balance_equations+1,1) = RS(1,3);

%Combine MC
MC = zeros(N_unknowns,N_unknowns);
MC(1:N_balance_equations, :) = MC_top;
MC(N_balance_equations+1:end, :) = MC_bot;

%linear independence
if det(MC) == 0;
    disp('system not linearly independent');
    return
end

%--Resolution--
% Flow rates: MC . X = B -> X = MC(-1) . B

SOL = inv(MC)*B; %[kg/s]

%Flow rates: combine with streams and components

FR = zeros(N_unknowns, 3);
FR(:,1:2) = MC_Hmarg_sc;
FR(:,3) = SOL; % columns: stream, component, flow rate [kg/s]

%--Results' Table of (streams x components)

RT = zeros(size(TD,2),size(TD,1));

for i = 1:size(TD,2)
    for j = 1:size(TD,1)
        for n = 1:N_unknowns
            if FR(n,1) == i && FR(n,2) == j;
                RT(i,j) = FR(n,3);
            end
        end
    end
end

%Calculating inlets/outlet flow rates, verifying balance
SUMin = zeros(1, size(RT, 2));
SUMout = zeros(1, size(RT, 2));

```

```
for i = 1:size(RT);
    if IOS(i) == 1;
        SUMin = SUMin + RT(i, :);
    elseif IOS(i) == -1;
        SUMout = SUMout + RT(i, :);
    end
end
SUMin
SUMout
if sum(SUMin-SUMout)> 1e-6;
    disp('ERROR, system not balanced')
end
IOC = [SUMin ; SUMout];
    %Component flowrates into and out of system
```
